# Interference effects in the cotunnelling transport regime

Master's Thesis
of
Christoph Rohrmeier

Institute of Theoretical Physics
University Regensburg

Supervisor: PD Dr. Andrea Donarini
Second referee: PD Dr. Juan Diego Urbina

July 29, 2019

# Contents

# Part I.

# Introduction

# 1

# Introduction

In December 1959 Richard Feynman gave a speech, which will prove path-breaking in retrospect, at the California Institute of Technology with the title "There's plenty of room at the bottom"[1]. In his speech, Richard Feynman described the abundant possibilities for researchers if they pursue the path to nanoscale physics. Even if he did not use the term nanotechnology, the transcript of his speech is now one of the most well-known articles in the history of this area. Among other things, he mentioned the vision to write the many volume encyclopedia Britannica on the head of a pin. For this goal, one would need to compress one unit of information to a point of 80 Å in diameter. This dream now became reality and the world record size for a semiconductor transistor is now 30 Å (see Figure 1.1): Just 10 atoms in a row fit the width of this transistor. In the light of these magnitudes, it is impossible to describe the processes there purely with classical physics. The quantum world with its intriguing phenomena starts inevitably to play an important role in this regime. Whereas the classical transistor operations get unstable at the atomic

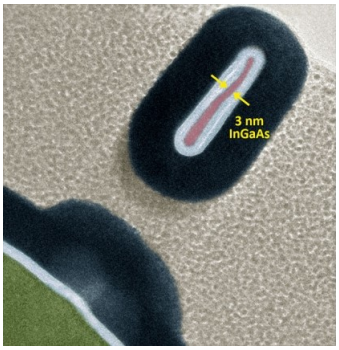


**Figure 1.1 | Cross-section of 3 nm semiconductor transistor** [2].

level, quantum mechanics is not detrimental to information technology. On the contrary, quantum information has shown how mastering quantum bit (Q-bit) operations will allow us to tackle problems of enormous complexity, otherwise inaccessible to classical computers [3]. The major challenge is to improve the reliability and scalability of the Q-bits which are the quantum version of classical transistors with the ultimate goal to make quantum computing feasible. A quantum computer which consists of those Q-bits could lead to huge changes in certain areas like cryptography, database search or molecule simulations. These areas may seem unimportant at first glance, but they do affect us to some extent in our everyday life: Cryptography is the fundamental tool to protect secure Web pages and other sensitive types of data like emails and an efficient way to search databases could save a lot of energy especially in the context that the amount of data which is produced every second

in the world is steadily increasing. Furthermore, more elaborate molecule simulations with the help of quantum computing could be used for the search of new materials in areas like drug or battery research. It is important to state that we are still at the very beginning of the road to a functioning quantum computer and it is not even clear if a quantum computer with sufficient computational power will ever be realized so that it can deliver on its far-reaching promises. Nevertheless, it should be recognized that despite these concerns prestigious companies like Intel, Google, Microsoft and IBM put a huge research effort and investment into this technology [4]. Maybe we are right now at the beginning of another step like the one Feynman proposed in his pioneering speech from 1959. It was, at these times, definitely not easy to believe in a fast realization of this enormous miniaturization and so is it now with quantum computing. Despite many obstacles and its enormous complexity, it is at least conceivable that another generation could benefit from quantum computers like we are benefiting now from the classical miniaturization of transistors. A fundamental step towards the realization of Q-bits and therefore quantum computing - of course not the only one in the light of the many technical difficulties - is the basic understanding and control of quantum mechanical phenomena at the nanoscale. One of those phenomena, namely quantum interference, is at the very heart of quantum

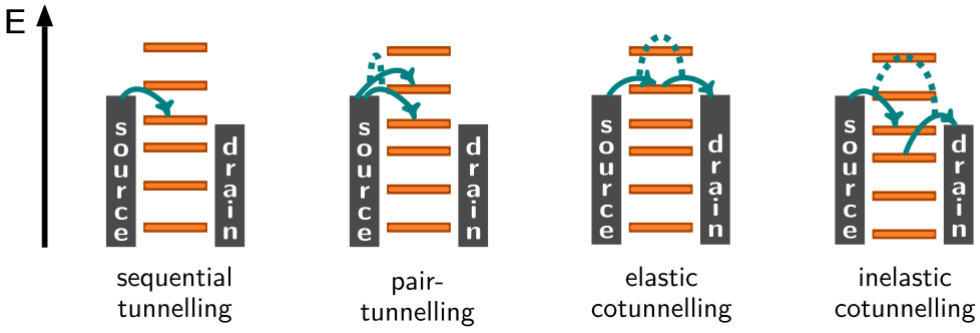


**Figure 1.2 | Visualization of a one-electron tunnelling process and correlated two-electron processes:** The leftmost setup shows an exemplary one-electron or sequential tunnelling process where one electron (green solid line) tunnels from the source to energy levels of the central system which are depicted in orange. The three rightmost setups show instead two-electron processes where the correlation between them is indicated by dashed green lines. These three different types of tunnelling events extend the transport regime to the cotunnelling one. Taken from Figure 2 of [5].

mechanics. It is a direct consequence of the superposition principle which allows quantum systems to be at the same time in two different states. Due to quantum interference - in close analogy to water waves - two coherent states or wave packets form a resultant wave in a constructive or destructive way. The most prominent experiment in this context is definitely the original double-slit experiment by Young where one can see single-particle interference [6]. Furthermore, single-particle interference has been observed with electrons in vacuum [7, 8] and even with the more massive $C_{60}$ molecules [9].

Nowadays, it is possible to study quantum interference in a wide range of systems as a result of ever-progressing experimental techniques. For a complete description of interference effects in experimental setups, it is necessary to account for the interaction of a system with its environment. Generally, decoherence originating from this interaction by e.g. the

coupling to the leads will obstruct interference. In recent years, huge attention was directed to the research of systems which bear such a coupling. Transport measurements, in which a microscopic, coherent system is coupled to macroscopic leads, are well-suited probes to investigate such phenomena. Intra-molecular interference has been recently discussed in molecular junctions for the case of strong [10–16] and weak [17–19] molecule-lead coupling. What unifies these realizations of quantum interference is that the travelling particle has two (or more) spatially equivalent paths at disposal to go from one point to another in the interferometer. Generally, for junctions in the strong coupling regime decoherence can be neglected due to the short time of flight of the particle within the interferometer. In the weak coupling case, instead, the dwelling time is long. It is the regime of the single electron tunnelling in which, usually, the decoherence introduced by the leads dominates the picture and the dynamics are governed by sequential tunnelling events. Though, well inside the Coulomb blockade region, tunnelling processes involving two electrons can become the dominant part by providing possible tunnelling paths that go beyond sequential tunnelling which is there limited by a tiny thermal excitation. This regime where one-electron and two-electron tunnelling events are considered is the so-called cotunnelling transport regime (see Figure 1.2). Cotunnelling events represent the second order term in the perturbation in the coupling strength which will be assumed to be small with respect to the temperature. This regime will be the main focus of this work especially in the context of interference effects.

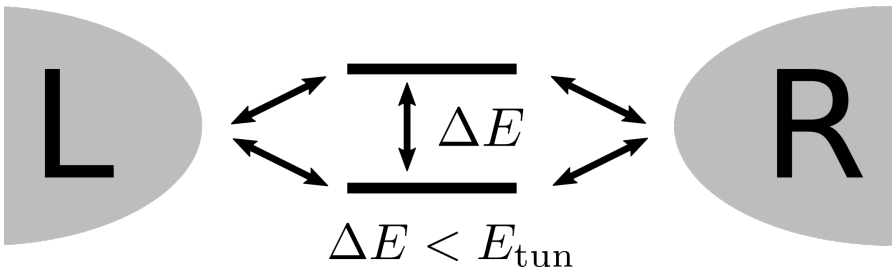


**Figure 1.3 | Schematic transport setup with two quasi-degenerate tunnelling paths:** Throughout this thesis, we will deal with transport systems where electrons can tunnel from two reservoirs ("L" and "R") in and out to a central system. Here, we consider explicitly two energy levels which are quasi-degenerate. The energy difference between them, namely $\Delta E$, is smaller than the energy $E_{\mathrm{tun}}$ which can be associated with the strength of the tunnel coupling. If we consider coherent coupling from the reservoirs to the energy levels, a current can flow via two equivalent paths through the system. In analogy to the double slit experiment by Young, one can see then interference effects arising.

Whenever two energetically equivalent paths involving degenerate states contribute to the dynamics, interference effects can occur (compare Figure 1.3). The associated fingerprints in the transport characteristics can be then strong negative differential conductance and eventually an interference blockade of the current in the case of fully destructive interference [20]. Another recent work showed such a current blocking also in a carbon nanotube quantum dot, due to the formation of a so-called all-electronic dark state which is decoupled from one of the leads (see Figure 1.4 g) [21]. The name for this state is chosen in close analogy to optical dark states. In this publication, theoretical and experimental data is provided and the interference blockade is clearly visible in both data sets through the disappearance of transition lines in the stability diagram (see Figure 1.4 a-f). This publication once again could provide strong experimental evidence of interference effects

in transport and therefore be a manifest of the underlying theory.

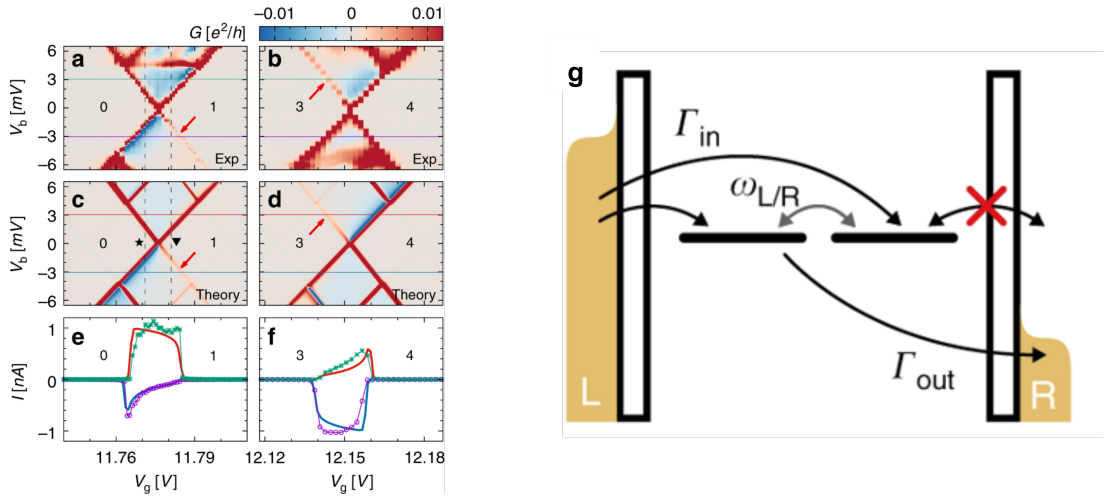


**Figure 1.4 | Interference blockade in a carbon nanotube quantum dot: a,b** Experimental stability diagrams: Differential conductance $G$ is plotted in a gate voltage-bias voltage-landscape. The red lines indicate transitions from specific leads to different occupation numbers of the quantum dot. It is clearly visible that negative differential conductance (blue) arises and that it is accompanied by suppression - indicated by the red arrows - of transition lines. In case of (a), an electron transition to the drain and in case of (b), a hole transition to the drain which is exactly expected under a reversed bias polarity and a mirrored gate voltage are suppressed. **c,d** Theoretical stability diagrams: Experimental data is reproduced except for an up to now unknown horizontal transition line. **e,f** Comparison of experimental (data points) and theoretical (solid lines) current-gate traces for $V_\mathrm{b} = \pm 3.045$ mV. **g** Quantum dot setup: For the chosen bias polarity, an electron can enter a dark state, which is formed by the two degenerate energy states, from the left lead but it cannot leave to the right lead. Precession $\omega_{\mathrm{L/R}}$ allows for population transfer from a dark state to a coupled state. Taken from Figure 1 and 3 of [21].

Another work highlighted a different form of interference, namely the appearance of a so-called canyon of conductance [22]. In an InSb nanowire quantum dot, they could measure suppression of conductance due to the interplay of interference and correlation of the electrons through their Coulomb repulsion. The location of this canyon coincides with the point in the gate voltage-magnetic field-landscape where two energy levels become degenerate (see Figure 1.5 (i) (c)). They supplemented this work with numerical calculations done with the second order von Neumann (2vN) approach [23]. This numerical expensive approach is non-perturbative in the coupling to the leads. On the one side, it bridges the gap between non-interacting Green's-function approaches and the interacting rate equations for the sequential tunnelling regime but on the other side, it is limited to small systems due to its numerical expensiveness. In a following up publication, they claim that this canyon appears when considering the 2vN approach and thus non-perturbative contributions [24]. They explicitly do not make a statement for the cotunnelling regime. One part of the motivation of this thesis is to enter exactly in this realm. Does this current suppression in the Coulomb blockade region already appear in the cotunnelling regime? If yes, then it would shift the picture from the necessity to include all orders of tunnelling events to just include cotunnelling events as the leading order in this region and therefore as sufficient to describe the phenomena there. Furthermore, one could ask what is the connection to other interference effects like interference blockade encountered in Figure 1.4. What do

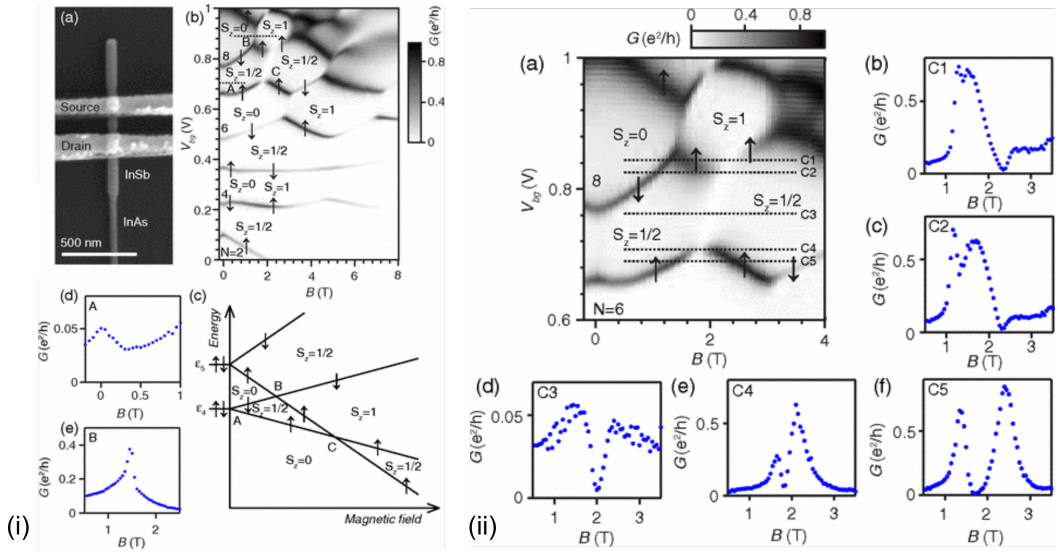


**Figure 1.5 | Correlation-induced conductance suppression at level degeneracy in an InSb quantum dot: (i)** (a) SEM image of a fabricated InSb nanowire quantum dot device. (b) Conductance in greyscale measured at a bias voltage of 0.5 mV. (c) Schematic for the evolution of the single-particle levels 4 and 5 with magnetic field due to the large level dependent g factors of InSb. The letters A, B and C mark three level degenerate points. (d) Conventional spin-1/2 Kondo peak at $B = 0$ T. (e) Integer-spin Kondo-like conductance enhancement at $B \approx 1.5$ T. **(ii)** (a) Enlarged section of (i) (b) with a clearly visible canyon of conductance. (b)-(f) Conductance plots along the line cuts C1-C5 of (a). Taken from Figure 1 and 2 of [22].

they have in common and how do they differ? Even if it is one of the fundamental phenomena of quantum physics, interference is not yet fully understood and therefore worth to investigate.

In this spirit, we will analyze in the following thesis interference effects in the cotunnelling transport regime. In the next part, we will introduce the theory which leads finally to the implementation of a transport code which is capable to treat cotunnelling transport. In the proceeding part, this transport code will be then applied to various model systems so that the asked questions can be addressed.

# Part II.

# Theory

# 2

# Hamiltonian of a quantum dot system

In this chapter, we will introduce the physical system of this thesis. Throughout this work, we consider a generic quantum dot system tunnel-coupled to a bath which in our case is represented by two leads (see Figure 2.1). We can write for this system the following general Hamiltonian $\hat{H}_{\mathrm{tot}}$:

$$\hat{H}_{\mathrm{tot}} = \hat{H}_{\mathrm{S}} + \hat{H}_{\mathrm{B}} + \hat{H}_{\mathrm{T}} \tag{2.1}$$

with the quantum dot system Hamiltonian $\hat{H}_{\mathrm{S}}$, the bath Hamiltonian $\hat{H}_{\mathrm{B}}$ and the tunnelling Hamiltonian $\hat{H}_{\mathrm{T}}$. The bath Hamiltonian is defined as

$$\hat{H}_{\mathrm{B}} = \sum_{l\sigma\mathbf{k}} \varepsilon_{l\sigma\mathbf{k}} \hat{c}^{\dagger}_{l\sigma\mathbf{k}} \hat{c}_{l\sigma\mathbf{k}} = \sum_{b} \varepsilon_b \hat{c}^{\dagger}_b \hat{c}_b \tag{2.2}$$

with $l$ as the lead index ($l = \mathrm{L}$ is the left lead and $l = \mathrm{R}$ is the right lead), $\sigma = \{\uparrow, \downarrow\}$ as the spin index of the lead and $\varepsilon$ as the energy of an electron with the momentum $\mathbf{k}$. We have introduced the second quantization fermionic annihilation operator $\hat{c}_{l\sigma\mathbf{k}}$ of an electron in the l-lead with spin $\sigma$ and momentum $\mathbf{k}$. Furthermore, in the last step we introduced a collective bath index $b = \{l, \sigma, \mathbf{k}\}$. The system Hamiltonian,

$$\hat{H}_{\mathrm{S}} = \hat{H}_0 + \mathrm{e}V_{\mathrm{g}}\hat{N}, \tag{2.3}$$

depends on the gate voltage $V_{\mathrm{g}}$, the specific form of the isolated quantum dot system Hamiltonian $\hat{H}_0$ and the number operator $\hat{N} = \sum_n \hat{d}^{\dagger}_n \hat{d}_n$. The number $n$ labels the single-particle quantum states of the system and thus the different fermionic creation operators $\hat{d}^{\dagger}_n$. In our thesis, we consider systems with a generic number of $i$ quantum dots. A single dot ($i = 1$) has, for example, two creation operators ($n = 2$), $\hat{d}^{\dagger}_{\uparrow}$ for spin-up and $\hat{d}^{\dagger}_{\downarrow}$ for spin down, so that its many-particle Fock space consists of four different states $\{|0\rangle, |\uparrow\rangle, |\downarrow\rangle, |2\rangle\}$ with the corresponding energies. In the case ($i = 1$), in the literature better known as the single dot Anderson impurity model, $\hat{H}_0$ takes the form

$$\hat{H}_0 = \sum_{\zeta=\{\uparrow,\downarrow\}} (\varepsilon_0 - E_\zeta)\, \hat{d}^{\dagger}_\zeta \hat{d}_\zeta + U \hat{d}^{\dagger}_{\uparrow} \hat{d}_{\uparrow} \hat{d}^{\dagger}_{\downarrow} \hat{d}_{\downarrow}. \tag{2.4}$$

with $\varepsilon_0$ as the on-site energy, $U$ as the on-site Coulomb interaction and $E_\zeta$ as a spin-dependent energy which can be understood e.g. as a Zeeman splitting through a magnetic field. The index $\zeta$ is throughout this work reserved for the spin degree of freedom of the system. The tunnelling Hamiltonian connects the bath and the system in the following way:

$$\hat{H}_{\mathrm{T}} = \sum_{l} \hat{H}_{T,l} = \sum_{bn} \left( t^{*}_{b,n} \hat{d}^{\dagger}_n \hat{c}_b + t_{b,n} \hat{c}^{\dagger}_b \hat{d}_n \right) = \sum_{pb} p\, \hat{c}^{p}_b \hat{D}^{\bar{p}}_b \tag{2.5}$$

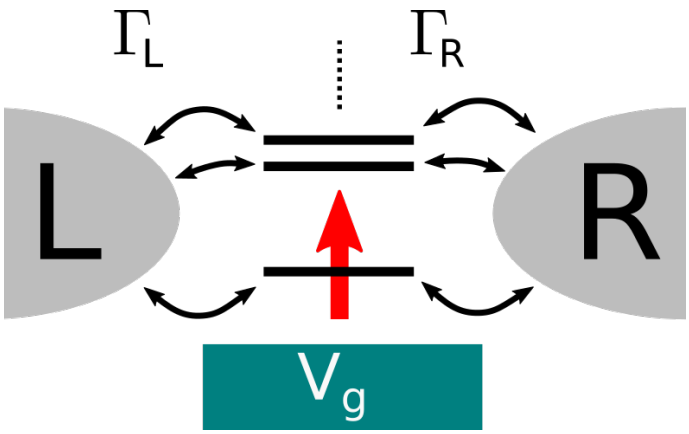


**Figure 2.1 | Schematic setup of a quantum dot system coupled to two leads:** A generic quantum dot system is depicted as energy levels (black lines) tunnel-coupled to a left lead (L) and a right lead (R). The tunnelling rate matrices $\Gamma_L$ and $\Gamma_R$ incorporate the coupling strength to the respective energy levels as well as the geometrical setup. With a gate voltage $V_g$, it is possible to shift the energy levels of the central system. In case of a single dot, there are two energy levels which are connected to the leads: one for spin up (compare red arrow) and one for spin down.

where $t_{b,n}$ are the tunnelling amplitudes with the collective bath index $b = \{l, \sigma, \mathbf{k}\}$ coupling an electron of the $l$-lead of spin $\sigma$ and momentum $\mathbf{k}$ to the energy level $n$ of the dot where in principle, the spin quantization axis can point in another direction as the one of the leads. In the last step, we combined the tunnelling amplitudes and the dot creation/annihilation operators to $\hat{D}_b^p := \sum_n t_{b,n}^p \hat{d}_n^p$ with superscript $p = +$ indicates the conjugate transpose of the matrix, $\hat{d}_n^+ := \hat{d}_n^\dagger$, or in the case of the tunnelling amplitudes, the complex of it, $t_{b,n}^+ := t_{b,n}^*$. The superscript $p = -$ indicates an annihilation operator, $\hat{d}_n^- := \hat{d}_n$, or a bare tunnelling amplitude $t_{b,n}^- := t_{b,n}$ with the property of the $p$-index: $\bar{p} := -p$.

# 3

# Introduction to the density matrix formalism

In this chapter, we will introduce the density matrix formalism which represents an elegant way to describe the state of a physical system. It goes beyond the usual state vector representation of quantum mechanics with taking into account the statistics of a system in a concise form. We work throughout this thesis with density matrices and hence this chapter provides the foundation of the following work. The sections of this chapter will mainly follow [25–27].

## 3.1. Density matrix operator

The density matrix is a way to describe a quantum mechanical system. The latter is determined by a series of measurements. Due to the very nature of quantum mechanics, it is only possible to simultaneously measure two physical variables if their associated operators commute so that it is possible to find a common eigenbasis $|\Psi\rangle$:

$$\left[\hat{Q}_1, \hat{Q}_2\right] = 0 \implies \exists\, |\Psi\rangle : \;\; \hat{Q}_1 |\Psi\rangle = q_1 |\Psi\rangle \;\wedge\; \hat{Q}_2 |\Psi\rangle = q_2 |\Psi\rangle \,. \tag{3.1}$$

A pure state is defined by U. Fano in 1957 as a state of "maximum knowledge" whereas we do not have full information of the system when considering a mixed state [28]. In general, the maximum information of a system consists of the eigenvalues $q_1, ..., q_N$ of the largest set of mutually commuting independent observables $Q_1, ..., Q_N$. The system is then completely specified as the following pure state vector:

$$|\Psi\rangle = |q_1, ..., q_N\rangle \,. \tag{3.2}$$

If $|\Psi\rangle$ is an eigenstate of the observable Q, each measurement gives exactly the same eigenvalue. Assuming the pure state $|\Psi\rangle$ is not an eigenstate of an observable Q then each measurement gives a different result. The average is then given by the expectation value $\langle \hat{Q} \rangle_{\text{pure}} = \langle \Psi | \hat{Q} | \Psi \rangle$. On the contrary, a mixed state, also known as a statistical mixture, cannot be characterized by a single state vector. Since we do not have full information of the system, there is an additional probability in this state which goes beyond the expectation value of a pure state. A mixed state is a statistical mixture of different pure states and can be written in terms of the probabilities $W_1, ..., W_N$ of being in the pure state $|\Psi_1\rangle, ..., |\Psi_N\rangle$:

$$\sum_n W_n = 1, \qquad 0 \leq W_n \leq 1. \tag{3.3}$$

It should be explicitly noted that a mixed state is not a quantum superposition of pure states. The expectation value of statistical mixture is for that reason defined as:

$$\left\langle \hat{Q} \right\rangle_{\text{mixed}} = \sum_n W_n \left\langle \Psi_n \right| \hat{Q} \left| \Psi_n \right\rangle . \tag{3.4}$$

Mixed states commonly arise from a statistical mixture of the starting state like in a thermal equilibrium or from looking at a subsystem entangled with another not measurable system. For example in thermal equilibrium, it is very likely that we are in the state which is the most probable and has the biggest entropy so that we have the least information about the state. The concept of a density matrix stems from the fact that there exist pure and mixed states. In general, the density matrix operator is then defined as:

$$\hat{\rho} \coloneqq \sum_n W_n \left| \Psi_n \right\rangle \left\langle \Psi_n \right| . \tag{3.5}$$

Note that if our system is in a pure state, then the density matrix operator has the form $\hat{\rho} = \left|\Psi\right\rangle \left\langle\Psi\right|$. In an explicit matrix representation, the density matrix operator acquires the following form:

$$\hat{\rho} = \sum_n \sum_{mm'} W_n \, a_m^{(n)} \, a_{m'}^{(n)*} \left| \phi_m \right\rangle \left\langle \phi_{m'} \right| \tag{3.6}$$

with $\left|\Psi_n\right\rangle = \sum_n a_m^{(n)} \left|\phi_m\right\rangle$. The elements of the density matrix in the basis $\{\phi_1, ..., \phi_n\}$ are then defined as:

$$\rho_{ij} = \left\langle \phi_i \right| \hat{\rho} \left| \phi_j \right\rangle = \sum_n W_n \, a_i^{(n)} \, a_j^{(n)*}. \tag{3.7}$$

In this thesis, we will use the term density matrix and density matrix operator equivalently with the knowledge that we can go from one particular density matrix operator in different bases. No matter in which basis we are, the density matrix operator always contains all meaningful information about our physical system. It can be easily shown that the density matrix $\hat{\rho}$ is hermitian and its trace is always 1. If Eq. (3.4) is extended, we will realize that the expectation value of an operator $\hat{Q}$ can be also seen as the trace of the product of the density matrix with the operator:

$$\begin{aligned} \left\langle \hat{Q} \right\rangle &\overset{(3.4)}{=} \sum_n W_n \left\langle \Psi_n \right| \hat{Q} \left| \Psi_n \right\rangle = \sum_n \sum_{mm'} W_n \, a_m^{(n)} \, a_{m'}^{(n)*} \left\langle \phi_{m'} \right| \hat{Q} \left| \phi_m \right\rangle \\ &\overset{(3.7)}{=} \sum_{mm'} \left\langle \phi_m \right| \hat{\rho} \left| \phi_{m'} \right\rangle \left\langle \phi_{m'} \right| \hat{O} \left| \phi_m \right\rangle = \mathrm{Tr} \left\{ \hat{\rho} \, \hat{Q} \right\} . \end{aligned} \tag{3.8}$$

Eq. (3.8) can be seen as an alternative way to define the density matrix (compare Eq. (3.5)). Out of this definition of the density matrix, it is clear that any expectation value of an operator can be derived from $\rho$ and thus it contains all physical information, namely the populations and the coherences. The populations are the diagonal elements of the density matrix $\hat{\rho}_{ii}$ and they tell us the probability of finding the system in the basis state $\left|\phi_i\right\rangle$. The off-diagonal elements $\hat{\rho}_{ij}$ are identified as the coherences between the states $\left|\phi_i\right\rangle$ and $\left|\phi_j\right\rangle$. It can be seen as a certain phase relation between these states which e.g. enables interference. Therefore a completely diagonal density describes a completely incoherent statistical mixture with no phase relation between the basis states.

## 3.2. Time evolution of the density matrix

The time evolution of quantum mechanical states is described by the Schrödinger equation

$$i\hbar\frac{\partial}{\partial t}\left|\Psi(t)\right\rangle = \hat{H}(t)\left|\Psi(t)\right\rangle. \tag{3.9}$$

The time evolution operator $\hat{U}(t,t_0)$ is defined as

$$\left|\Psi(t)\right\rangle \coloneqq \hat{U}(t,t_0)\left|\Psi(t_0)\right\rangle \tag{3.10}$$

with $\hat{U}(t) \coloneqq \hat{U}(t,0)$. Plugging the time evolution operator into the Schrödinger equation will lead to

$$i\hbar\frac{\partial}{\partial t}\hat{U}(t) = \hat{H}(t)\hat{U}(t) \tag{3.11}$$

where we can deduce that $\hat{U}(t)$ is a unitary operator with initial condition $\hat{U}(0) = \mathbb{1}$. Applying then the well-defined time evolution operator on an initial density matrix $\hat{\rho}(0) = \sum_n W_n \left|\Psi_n(0)\right\rangle\left\langle\Psi_n(0)\right|$ will get its time evolution:

$$\hat{\rho}(t) = \sum_n W_n \hat{U}(t)\left|\Psi_n(0)\right\rangle\left\langle\Psi_n(0)\right|\hat{U}^\dagger(t) \tag{3.12}$$

$$= \hat{U}(t)\hat{\rho}(0)\hat{U}^\dagger(t). \tag{3.13}$$

Differentiating Eq. (3.12) will lead to the famous Liouville-von Neumann equation (LVNE) which - as we just demonstrated - directly stems from the Schrödinger equation:

$$i\hbar\frac{\partial}{\partial t}\hat{\rho}(t) = \Big[\hat{H}(t),\hat{\rho}(t)\Big]. \tag{3.14}$$

It is convenient to write the LVNE in terms of the Liouville superoperator $\mathcal{L}(t)$:

$$\mathcal{L}(t)\hat{X} \coloneqq -\frac{i}{\hbar}\Big[\hat{H}(t),\hat{X}\Big] \implies \dot{\hat{\rho}}(t) = \mathcal{L}(t)\hat{\rho}(t) \tag{3.15}$$

where we denoted the time derivative with a dot. It is important to note the Liouville superoperator acts on a generic matrix $\hat{X}$ in analogy to a matrix which acts on a vector. This concept is captured in the Liouville space (compare Table 4.1). In the case of the time-independent Hamiltonian $\hat{H}_{\mathrm{tot}}$ which we consider in this thesis (compare chapter 2), the Liouvillian can be written as $\mathcal{L}(t) \coloneqq \mathcal{L} = \mathcal{L}_{\mathrm{B}} + \mathcal{L}_{\mathrm{S}} + \mathcal{L}_{\mathrm{T}}$.

## 3.3. Reduced density matrix

As we already mentioned in chapter 2, our total system is formed by the leads and the dot system with their respective Hilbert spaces $\mathcal{H}_{\mathrm{B}} = \{|\phi_\alpha\rangle\}$, for the leads, and $\mathcal{H}_{\mathrm{S}} = \{|\phi_\beta\rangle\}$, for the dot system part. As an assumption, our total state vector at an initial time could be written as the Kronecker product of two pure state vectors of the respective Hilbert spaces:

$$\left|\Psi(0)_{\alpha,\beta}\right\rangle = \left|\phi_\alpha\right\rangle \otimes \left|\phi_\beta\right\rangle. \tag{3.16}$$

Turning on the interaction will change the picture drastically. The total system gets entangled so that it is not possible anymore to factorize the state vector into the two subsystems. Nonetheless, if the two subsystems were in a pure state at the initial time, their entangled state vector stays in a pure state. We can define the density matrix of such an entangled state as

$$|\Psi_{\alpha,\beta}(t)\rangle = \sum_{ij} a(i,j,\alpha,\beta,t)\,|\phi_{i,\alpha}\rangle \otimes |\phi_{j,\beta}\rangle \tag{3.17}$$

with $a(i,j,\alpha,\beta,t)$ the coefficient yielding the probability of finding the bath in $|\phi_\alpha\rangle$ and simultaneously the dot system in $|\phi_\beta\rangle$. Since we are only interested in the time evolution of the dot system, we can construct the so-called reduced density matrix (RDM):

$$\rho_{\text{red}} \coloneqq \sum_{i} \langle\phi_{i,\alpha}|\,\hat{\rho}(t)\,|\phi_{i,\alpha}\rangle = \text{Tr}_{\text{B}}\left\{\hat{\rho}(t)\right\}. \tag{3.18}$$

$\text{Tr}_{\text{B}}\{\}$ denotes the trace over the lead degrees of freedom. From there, we can rewrite the expectation value of an operator which acts only on the dot system in terms of the RDM:

$$\begin{aligned}\left\langle\hat{Q}\right\rangle &= \text{Tr}\left\{\hat{\rho}\,\hat{Q}\right\}\\ &= \sum_{i\,j}\sum_{i'j'} \langle\phi_{i,\alpha}\phi_{j,\beta}|\,\hat{\rho}\,|\phi_{i',\alpha}\phi_{j',\beta}\rangle\,\langle\phi_{i',\alpha}|\phi_{i,\alpha}\rangle\,\langle\phi_{j',\beta}|\,\hat{Q}\,|\phi_{j,\beta}\rangle\\ &= \text{Tr}_{\text{S}}\left\{\hat{\rho}_{\text{red}}\,\hat{Q}\right\}\end{aligned} \tag{3.19}$$

If we are only interested in observables of the quantum dot system, the RDM is the tool to reduce the complexity of the LVNE. It is possible to reformulate LVNE in one equation for the RDM by inserting Eq. (3.18) in Eq. (3.15):

$$\dot{\hat{\rho}}_{\text{red}}(t) = \text{Tr}_{\text{B}}\left\{\hat{L}_{\text{tot}}\,\hat{\rho}(t)\right\}, \tag{3.20a}$$

$$\hat{\rho}(t_0) = \hat{\rho}_{\text{red}}(t_0)\otimes\hat{\rho}_{\text{B}}(t_0). \tag{3.20b}$$

For Eq. (3.20b) we took as an initial condition an uncorrelated total system hence there is no interaction at $t_0$ between the dot system and the leads. The bath density matrix can be finally written as

$$\hat{\rho}_{\text{B}} = \hat{\rho}_{\text{L}}\otimes\hat{\rho}_{\text{R}}. \tag{3.21}$$

Furthermore, we assume that the two leads are in thermal equilibrium so that we can construct the density operator of the $l$-lead ($l = \text{L/R}$) as a grand-canonical ensemble

$$\hat{\rho}_l = \frac{\text{e}^{-\beta\left(\hat{H}_l-\mu_l\hat{N}_l\right)}}{Z_l} \tag{3.22}$$

where $\mu_l$ is the chemical potential of the respective lead and $Z_l = \text{Tr}_l\{\text{e}^{-\beta\left(\hat{H}_l-\mu_l\hat{N}_l\right)}\}$ is the partition function of the respective lead. In the latter, we use $\beta = \frac{1}{k_{\text{B}}T}$ with temperature $T$ and Boltzmann constant $k_{\text{B}}$. The number operator of the $l$-lead is defined as $\hat{N}_l = \sum_{\boldsymbol{\sigma}\mathbf{k}} \hat{c}^\dagger_{l\boldsymbol{\sigma}\mathbf{k}}\hat{c}_{l\boldsymbol{\sigma}\mathbf{k}}$. The chemical potential of the leads constitute of the bias voltage $V_{\text{b}}$, the elementary charge e, the Fermi level of the system $\mu_0$ and the asymmetry parameter for the bias voltage drop $\alpha_{\text{b}}$ ($0 \le \alpha_{\text{b}} \le 1$) in the following form:

$$\mu_{\text{L}} = \mu_0 - \text{e}\alpha_{\text{b}}V_{\text{b}}, \tag{3.23a}$$

$$\mu_{\text{R}} = \mu_0 + \text{e}(1-\alpha_{\text{b}})V_{\text{b}}. \tag{3.23b}$$

# 4

# Transport theory

In this chapter, we want to introduce the transport theory which is used in this thesis. With the help of a generalized master equation (GME), we can accurately describe the time evolution of our systems. The goal of this thesis is to rigorously take into account not only the populations of the underlying density matrix but also all its coherences. Only then it is possible to capture interference effects in full glory. The method of choice to derive a GME is the Nakajima-Zwanzig projection operator technique. In comparison with other techniques which are summarized in [5, 27], it is here easier to go to single-time diagrammatics in the Liouville space and the equations get more compact. This chapter will mainly follow [26, 29].

## 4.1. Nakajima-Zwanzig equation

The Nakajima-Zwanzig projection operator technique is a powerful tool to derive a GME which is needed to describe the explicit time evolution of quantum dot systems described in chapter 2. The main idea of Nakajima and Zwanzig is to split the total density into two parts: one where the quantum dot system and the leads are separated ($\mathcal{P}\hat{\rho}_{\mathrm{tot}}$) and one where the entanglement of the quantum dot system and the leads is captured ($\mathcal{Q}\hat{\rho}_{\mathrm{tot}}$) [30, 31]. This is done by the two projectors

$$\mathcal{P}\hat{X} \coloneqq \mathrm{Tr}_{\mathrm{B}}\left\{\hat{X}\right\} \otimes \hat{\rho}_{\mathrm{B}}, \tag{4.1}$$

$$\mathcal{Q}\hat{X} \coloneqq (1-\mathcal{P})\hat{X} \tag{4.2}$$

with $\hat{X}$ an arbitrary density matrix. There are some important properties of these projectors namely: $\mathcal{P}^2 = \mathcal{P}$, $\mathcal{Q}^2 = \mathcal{Q}$, $\mathcal{P}\mathcal{Q} = \mathcal{Q}\mathcal{P} = 0$, $\mathcal{P}\mathcal{L}_{\mathrm{B}} = \mathcal{L}_{\mathrm{B}}\mathcal{P} = 0$, $\mathcal{P}\mathcal{L}_{\mathrm{S}} = \mathcal{L}_{\mathrm{S}}\mathcal{P}$, $\mathcal{P}\mathcal{L}_{\mathrm{T}}^{2n+1}\mathcal{P} = 0$ for $n \in \mathbb{N}$. Applying these projectors to the LVNE result in:

$$\mathcal{P}\dot{\hat{\rho}}(t) = \mathcal{P}\mathcal{L}\mathcal{Q}\hat{\rho}(t) + \mathcal{P}\mathcal{L}\mathcal{P}\hat{\rho}(t), \tag{4.3}$$

$$\mathcal{Q}\dot{\hat{\rho}}(t) = \mathcal{Q}\mathcal{L}\mathcal{Q}\hat{\rho}(t) + \mathcal{Q}\mathcal{L}\mathcal{P}\hat{\rho}(t). \tag{4.4}$$

It is possible to solve Eq. (4.4) with the help of the propagator $\mathcal{G}_{\mathcal{Q}}(t) = e^{\mathcal{Q}\mathcal{L}t}$, by multiplying it with $\mathcal{G}_{\mathcal{Q}}(-t)$ from the left:

$$\frac{\mathrm{d}}{\mathrm{d}t}\left[\mathcal{G}_{\mathcal{Q}}(-t)\mathcal{Q}\hat{\rho}(t)\right] = \mathcal{G}_{\mathcal{Q}}(-t)\mathcal{Q}\mathcal{L}\mathcal{P}\hat{\rho}(t). \tag{4.5}$$

Integrating this equation and then multiplying the equation from the left with $\mathcal{G}_{\mathcal{Q}}(t)$ yields

$$\mathcal{Q}\hat{\rho}(t) = \mathcal{G}_{\mathcal{Q}}(t)\mathcal{Q}\hat{\rho}(0) + \int_0^t \mathrm{d}s\, \mathcal{G}_{\mathcal{Q}}(t-s)\mathcal{Q}\mathcal{L}\mathcal{P}\hat{\rho}(s). \tag{4.6}$$

Reinserting this equation of the entangled part into Eq. (4.3) and keeping in mind $\mathcal{Q}\hat{\rho}(0) = 0$ will lead to

$$\mathcal{P}\dot{\hat{\rho}}(t) = \mathcal{P}\mathcal{L}\mathcal{P}\hat{\rho}(t) + \int_0^t \mathrm{d}s\, \mathcal{P}\mathcal{L}\mathcal{G}_{\mathcal{Q}}(t-s)\mathcal{Q}\mathcal{L}\mathcal{P}\hat{\rho}(s). \tag{4.7}$$

Simplifying this expression with $\mathcal{P}\mathcal{L}\mathcal{P} = \mathcal{L}_{\mathrm{S}}\mathcal{P}$, $\mathcal{P}\mathcal{L}\mathcal{Q} = \mathcal{P}\mathcal{L}_{\mathrm{T}}$ and $\mathcal{Q}\mathcal{L}\mathcal{P} = \mathcal{L}_{\mathrm{T}}\mathcal{P}$ gives the Nakajima-Zwanzig equation

$$\mathcal{P}\dot{\hat{\rho}}(t) = \mathcal{L}_{\mathrm{S}}\mathcal{P}\hat{\rho}(t) + \int_0^t \mathrm{d}s\, \mathcal{K}(t-s)\mathcal{P}\hat{\rho}(s). \tag{4.8}$$

with the Kernel superoperator $\mathcal{K}(t) = \mathcal{P}\mathcal{L}_{\mathrm{T}}\bar{G}_{\mathcal{Q}}(t)\mathcal{L}_{\mathrm{T}}\mathcal{P}$. We have used here another slightly different definition of the propagator for the entangled part $\bar{G}_{\mathcal{Q}}(t) = e^{(\mathcal{L}_{\mathrm{S}}+\mathcal{L}_{\mathrm{B}}+\mathcal{Q}\mathcal{L}_{\mathrm{T}}\mathcal{Q})t}$ which can be substituted in the following equation with the formerly defined $\mathcal{G}_{\mathcal{Q}}(t)$:

$$\begin{aligned}\mathcal{P}\mathcal{L}\mathcal{G}_{\mathcal{Q}}(t)\mathcal{Q}\mathcal{L}\mathcal{P} &= \mathcal{P}\mathcal{L}e^{\mathcal{Q}\mathcal{L}t}\mathcal{Q}\mathcal{L}\mathcal{P} = \mathcal{P}\mathcal{L}_{\mathrm{T}}e^{(\mathcal{L}_{\mathrm{S}}+\mathcal{L}_{\mathrm{B}}+\mathcal{Q}\mathcal{L}_{\mathrm{T}}\mathcal{Q})t}\mathcal{L}_{\mathrm{T}}\mathcal{P} \\ &= \mathcal{P}\mathcal{L}_{\mathrm{T}}\bar{G}_{\mathcal{Q}}(t)\mathcal{L}_{\mathrm{T}}\mathcal{P}.\end{aligned} \tag{4.9}$$

The Nakajima-Zwanzig equation (Eq. (4.8)) is so far exact to all orders in the tunnelling Hamiltonian $\hat{H}_{\mathrm{T}}$ and the Markovian approximation is not performed so that the time evolution, not only the steady-state, is captured exactly via the propagator $\bar{G}_{\mathcal{Q}}(t)$. In this thesis, however, only the steady-state is of interest. The steady-state of the RDM is reached at an infinite time and is per definition $\hat{\rho}_{\mathrm{red}}(t \to \infty) \coloneqq \hat{\rho}^{\infty}$. In this limit the Laplace transformation (*L.t.*) can help us to simplify Eq. (4.8). In general, a Laplace transformation is defined as

$$L.t.\left\{f(t)\right\} = \tilde{f}(\lambda) = \int_0^{\infty} \mathrm{d}t f(t) e^{-\lambda t}. \tag{4.10}$$

Our aim is now to perform this transformation on

$$\hat{g}(t) \coloneqq \int_0^t \mathrm{d}s\, \mathcal{K}(t-s)\mathcal{P}\hat{\rho}(s) \tag{4.11}$$

which yields, due to the convolution theorem,

$$L.t.\left\{\hat{g}(t)\right\} = \hat{g}(\lambda) = \tilde{\mathcal{K}}(\lambda)\mathcal{P}\tilde{\hat{\rho}}(\lambda). \tag{4.12}$$

According to the final value theorem ($\lim_{t\to\infty} f(t) = \lim_{\lambda\to 0^+} \lambda\tilde{f}(\lambda)$), Eq. (4.8) turns into

$$0 = \mathcal{L}_{\mathrm{S}}\hat{\rho}^{\infty} + \lim_{\lambda\to 0^+} \lambda\tilde{\mathcal{K}}(\lambda)\mathcal{P}\tilde{\hat{\rho}}(\lambda) = \left(\mathcal{L}_{\mathrm{S}} + \mathcal{K}\right)\hat{\rho}^{\infty}. \tag{4.13}$$

Hereby, we used the fact that a limit of a product is the product of the limits if they exist, so that we can write $\lim_{\lambda\to 0^+} \lambda\mathcal{P}\tilde{\hat{\rho}}(\lambda)$ back into $\hat{\rho}^{\infty}$. From now on, we will denote with $\mathcal{K}$ the Laplace-transformed Kernel which is defined as

$$\mathcal{K}\hat{\rho}^{\infty} = \lim_{\lambda\to 0^+} \mathrm{Tr}_{\mathrm{B}}\left\{\mathcal{L}_{\mathrm{T}}\tilde{\mathcal{G}}_{Q}(\lambda)\mathcal{L}_{\mathrm{T}}\hat{\rho}^{\infty} \otimes \hat{\rho}_{\mathrm{B}}\right\} \tag{4.14}$$

with $\tilde{\mathcal{G}}_Q(\lambda)$ the Laplace transformation of the propagator $\bar{\mathcal{G}}_Q(t)$ which can be therefore written as $\tilde{\mathcal{G}}_Q(\lambda) = [\lambda - \mathcal{L}_\mathrm{S} - \mathcal{L}_\mathrm{B} - \mathcal{Q}\mathcal{L}_\mathrm{T}\mathcal{Q}]^{-1}$. It is possible to rewrite the Kernel $\mathcal{K}$ as a series of $\mathcal{L}_\mathrm{T}$. Using the relation for a geometrical series

$$\frac{1}{x-y} = \frac{1}{x\left(1-\frac{y}{x}\right)} = \sum_{n=0}^{\infty}\left(\frac{y}{x}\right)^n \frac{1}{x} \tag{4.15}$$

with $x^{-1} = \tilde{\mathcal{G}}_0$ and $y = \mathcal{Q}\mathcal{L}_\mathrm{T}\mathcal{Q}$. $\tilde{\mathcal{G}}_0 = \lim_{\lambda\to 0^+}\tilde{\mathcal{G}}_0(\lambda) = \lim_{\lambda\to 0^+}[\lambda - \mathcal{L}_\mathrm{S} - \mathcal{L}_\mathrm{B}]^{-1}$ is the propagator of the system and the bath in Laplace space. We obtain

$$K\hat{\rho}^\infty = \mathrm{Tr}_\mathrm{B}\left\{\mathcal{L}_\mathrm{T}\sum_{n=0}^{\infty}\left(\tilde{\mathcal{G}}_0\mathcal{Q}\mathcal{L}_\mathrm{T}\mathcal{Q}\right)^{2n}\tilde{\mathcal{G}}_0\mathcal{L}_\mathrm{T}\hat{\rho}^\infty\otimes\hat{\rho}_\mathrm{B}\right\}. \tag{4.16}$$

Since $\mathcal{P}\mathcal{L}_\mathrm{T}^{2n+1}\mathcal{P} = 0$ for $n \in \mathbb{N}$, only an even number of $\mathcal{L}_\mathrm{T}$ survives in the trace of the bath. It should be noted that the limit $\lim_{\lambda\to 0^+}$ should be performed at the very end of the calculation and not in the free propagator alone. In the following, this fact that the limit still has to be performed is marked with $0^+$ in the propagators. This procedure of writing the propagator $\tilde{\mathcal{G}}_Q(\lambda)$ in a geometrical series is only valid if the series converges. This condition is fulfilled in the so-called weak coupling limit where the tunnelling rate is small compared to the temperature ($\hbar\Gamma \ll k_\mathrm{B}T$). Rewriting the Nakajima-Zwanzig equation (Eq. (4.8)) in the steady-state limit results in

$$\dot{\hat{\rho}}^\infty = 0 = \mathcal{L}\hat{\rho}^\infty = (\mathcal{L}_\mathrm{S} + \mathcal{K})\,\hat{\rho}^\infty. \tag{4.17}$$

## 4.2. Sequential tunnelling

Considering the full Kernel from Eq. (4.16) to the lowest non-vanishing order, $\mathcal{K} = \mathcal{K}^{(2)} + \mathcal{O}(\hat{H}_\mathrm{T}^4)$, we get the following sequential tunnelling Kernel

$$\mathcal{K}^{(2)}\hat{\rho}^\infty = \mathrm{Tr}_\mathrm{B}\left\{\mathcal{L}_\mathrm{T}\frac{1}{0^+ - \mathcal{L}_\mathrm{S} - \mathcal{L}_\mathrm{B}}\mathcal{L}_\mathrm{T}\hat{\rho}^\infty\otimes\hat{\rho}_\mathrm{B}\right\}. \tag{4.18}$$

This Kernel will be also called second order Kernel due to the appearance of two Louvillians $\mathcal{L}_\mathrm{T}$ and therefore denoted by the superscript "(2)". To simplify the notation of a superoperator $X$, let us introduce the parameter $\alpha$ which is defined by

$$[X,\hat{\rho}] = X\hat{\rho} - \hat{\rho}X \coloneqq X^+\hat{\rho} - X^-\hat{\rho} = \sum_\alpha \alpha X^\alpha\hat{\rho}. \tag{4.19}$$

Using this notation for $\mathcal{L}_\mathrm{T}$ yields

$$\begin{aligned}\mathcal{L}_\mathrm{T}\hat{X} &= -\frac{i}{\hbar}\left(\hat{H}_\mathrm{T}\hat{X} - \hat{H}_\mathrm{T}\hat{X}\right) = -\frac{i}{\hbar}\sum_{pb} p\left(\hat{c}_b^p\hat{D}_b^{\bar{p}}\hat{X} - \hat{X}\hat{c}_b^p\hat{D}_b^{\bar{p}}\right)\\ &\coloneqq -\frac{i}{\hbar}\sum_{pb} p\left(c_b^{p,+}D_b^{\bar{p},+} - c_b^{p,-}D_b^{\bar{p},-}\right)\hat{X} = -\frac{i}{\hbar}\sum_{pb\,\alpha} p\,c_b^{p,\alpha}D_b^{\bar{p},\alpha}\hat{X}.\end{aligned} \tag{4.20}$$

Herby should be noted that the minus sign arising from the commutator of the Hamiltonian is cancelled by the relation: $(XY)^\alpha = \alpha X^\alpha Y^\alpha$ if $\{X,Y\} = 0$. The required condition of

anticommutating operators are provided in our case by the fermionic anticommutation relation of $\{\hat{c}_b^p, \hat{D}_b^{\bar{p}}\} = 0$. The operators transform to Liouville space superoperators like $\hat{c}_b^p \to c_b^{p,\alpha}$ where $\alpha$ indicates an operator which acts from the left or right side. Applying Eq. (4.20) on the second order Kernel of Eq. (4.18), we obtain

$$\mathcal{K}^{(2)}\hat{\rho}^\infty = -\frac{i}{\hbar}\sum_{\substack{b\alpha p\\ b'\alpha' p'}} pp'\,\mathrm{Tr_B}\left\{c_b^{p,\alpha} D_b^{\bar{p},\alpha}\frac{1}{i0^+ - i\hbar\mathcal{L}_\mathrm{S} - p'\xi_{b'}} c_{b'}^{p',\alpha'} D_{b'}^{\bar{p}',\alpha'}\hat{\rho}^\infty \otimes \hat{\rho}_\mathrm{B}\right\} \tag{4.21}$$

with the energy $\xi_{b'}$ which is associated with the rightmost bath operator which can destroy ($p' = -$) or create ($p' = +$) an electron. The next step is to separate the bath part from the system part. In order to achieve that we have to use the commutation rule for superoperators which reads $X^\alpha Y^{\alpha'} = -\alpha\alpha' Y^{\alpha'} X^\alpha$ in case of anticommuting operators. The result is

$$\mathcal{K}^{(2)}\hat{\rho}^\infty = \frac{i}{\hbar}\sum_{\substack{b\alpha p\\ b'\alpha' p'}} pp'\alpha\alpha' D_b^{\bar{p},\alpha}\frac{1}{i0^+ - i\hbar\mathcal{L}_\mathrm{S} - p'\xi_{b'}} D_{b'}^{\bar{p}',\alpha'}\hat{\rho}^\infty\,\mathrm{Tr_B}\left\{c_b^{p,\alpha} c_{b'}^{p',\alpha'}\hat{\rho}_\mathrm{B}\right\}. \tag{4.22}$$

The trace over the bath can be performed using the bath correlators of the Fermi-Dirac statistics

$$\mathrm{Tr_B}\left\{c_b^{p,\alpha} c_{b'}^{p',\alpha'}\rho_\mathrm{B}\right\} = \left\langle c_{l\sigma\mathbf{k}}^{p,\alpha} c_{l'\sigma'\mathbf{k}'}^{p',\alpha'}\right\rangle = \delta_{ll'}\delta_{\sigma\sigma'}\delta_{\mathbf{k}\mathbf{k}'}\delta_{p\bar{p}'} f_l^{(p\alpha')}(\xi_{l\sigma\mathbf{k}}) \tag{4.23}$$

with the Fermi-function $f_l^p(\varepsilon) = 1/\left(e^{p\beta(\varepsilon-\mu_l)}+1\right)$ together with $\beta = 1/\left(k_\mathrm{B}T\right)$ and its counterpart with no units $f^p(x) = 1/\left(e^{px}+1\right)$. It should be emphasized that the superscript of the Fermi-function is $(p\alpha')$ which can be deduced starting from the general expression $\mathrm{Tr}\{\hat{c}_{l\sigma\mathbf{k}}^\dagger \hat{c}_{l\sigma\mathbf{k}}\hat{\rho}\} = \langle\hat{n}\rangle = f_l^+(\xi_{l\sigma\mathbf{k}})$, using the cyclic property of the trace and respecting the different cases for left operators $\alpha = +$ and right operators $\alpha = -$ in our notation. Setting $\varepsilon := \xi_{l\sigma\mathbf{k}}$ yields

$$\mathcal{K}^{(2)}\hat{\rho}^\infty = -\frac{i}{\hbar}\sum_{l\sigma p}\sum_{\alpha\alpha'}\int_{-\infty}^{\infty}\mathrm{d}\varepsilon\;\alpha\alpha' D_{l\sigma}^{\bar{p},\alpha}\frac{f_l^{(p\alpha')}(\varepsilon)\,g_{l\sigma}(\varepsilon)}{i0^+ - i\hbar\mathcal{L}_\mathrm{S} + p\varepsilon} D_{l\sigma}^{p,\alpha'}\hat{\rho}^\infty \tag{4.24}$$

with the replacement $\sum_b = \sum_{l\sigma\mathbf{k}} = \sum_{l\sigma}\int\mathrm{d}\varepsilon\sum_\mathbf{k}\delta(\varepsilon - \varepsilon_{l\sigma\mathbf{k}}) = \sum_{l\sigma}\int\mathrm{d}\varepsilon\; g_{l\sigma}(\varepsilon)$ with $g_{l\sigma}(\varepsilon)$ the density of states for the spin $\sigma$ of the $l$-lead. It should be noted that throughout this thesis the $D$-operators are not dependent on $\mathbf{k}$ and thus are not dependent on $\varepsilon$ as well. Therefore, we will drop the index $\mathbf{k}$ of the $D$-operators after the energy integration. It will be important for the energy integration to have a Lorentzian cut-off function $L(\tilde{W}, \varepsilon)$ which ensures the convergence of the integral. The physical argument for this is that we assume the so-called wide band limit. In a wide band of energies, the density of states is constant (at $\bar{g}_{l\sigma}$) with a cut-off at very high energies. According to this requirement, the density of states could be written as $g_l(\varepsilon) = \bar{g}_l L(\tilde{W}, \varepsilon - \mu_l) = \bar{g}_l\,\tilde{W}^2/((\varepsilon-\mu_l)^2 + \tilde{W}^2)$ with the high energy band limit $\tilde{W}$. To proceed further, we separate the $D$-superoperators again in the tunnelling amplitudes and the $d$-superoperators to be able to define the entries of the tunnelling rate matrix as

$$\Gamma_{l,nm}^p := \sum_\sigma \Gamma_{l,nm}^{p\sigma} = \sum_\sigma \frac{2\pi}{\hbar}\bar{g}_{l\sigma} t_{l\sigma\mathbf{k},n}^{\bar{p}} t_{l\sigma\mathbf{k},m}^{p}. \tag{4.25}$$

As it can be deduced from its name, it has the dimension of one over time. The explicit form of these matrices will be at the very heart of the interference effects which will be

discussed to a greater extent in chapter 7. Their size is in general $n \times n$ where $n$ is the number of single-particle states of our quantum dot system. Expressing Eq. (4.24) with the tunnelling rate matrix leads to

$$\mathcal{K}^{(2)}\hat{\rho}^{\infty} = -\frac{i}{2\pi}\sum_{nm}\sum_{pl}\sum_{\alpha\alpha'}\int_{-\infty}^{\infty} \mathrm{d}\varepsilon\ \alpha\alpha'\Gamma^{p}_{l,nm} d_n^{\bar{p},\alpha}\frac{f_l^{(p\alpha')}(\varepsilon)\, L(\tilde{W},\varepsilon-\mu_l)}{i0^{+}-i\hbar\mathcal{L}_{\mathrm{S}}+p\varepsilon} d_m^{p,\alpha'}\hat{\rho}^{\infty}. \tag{4.26}$$

where $d_n^{\bar{p},\alpha}$ is the $\hat{d}_n^{p}$-operator in the Liouville space. To perform the energy integral in this Kernel, we have to go from the operatorial level with the Liouvillian $\mathcal{L}_{\mathrm{S}}$ acting on the whole density matrix containing many different energy differences to one specific energy difference $\Delta E$. This projection is explicitly shown in [29]. The part of the energy integration can be then substituted by $Y_{+}^{\alpha'}\left(\beta(\Delta E - p\mu_l)\right)$ with

$$Y_m^n(\mu) \coloneqq -\frac{i}{2\pi}\int \mathrm{d}x \frac{f^{(n)}(x)\, L(W,x)}{m(x-\mu)+i0^{+}}. \tag{4.27}$$

with the renormalized energy band limit $W$ so that $W$ is dimensionless. This integral is explicitly performed in Appendix A in close analogy to [27], but with the important difference that the splitting of the real and the imaginary part is not executed. This splitting is closely related to the Sokhotski-Plemelj theorem with its imaginary part with a $\delta$-function and its real part with a principle part integration. With our approach, though, we rely only on the residuum theorem to obtain the result. This approach will be the method of choice also for the more complicated integrals later in this thesis. Finally, we get for $Y_{+}^{n}(\mu)$,

$$Y_{+}^{n}(\mu) = -\frac{1}{2}f^{n}(\mu) - \frac{in}{2\pi}\left[\mathrm{Re}\Psi^{(0)}\left(\frac{1}{2}+\frac{i\mu}{2\pi}\right)-C\right] = -\frac{1}{4} - \frac{in}{2\pi}\left[\Psi^{(0)}\left(\frac{1}{2}+\frac{i\mu}{2\pi}\right)-C\right] \tag{4.28}$$

with the constant $C = \Psi^{(0)}(\frac{1}{2}+\frac{W}{2\pi})$ defined by the renormalized wide band constant $W$. We furthermore introduced the digamma function

$$\Psi^{(0)}(z) \coloneqq -\sum_{n=0}^{\infty}\frac{1}{n+z} + \sum_{n=1}^{\infty}\log\left(1+\frac{1}{n}\right) = -\sum_{n=0}^{\infty}\frac{1}{n+z} + C', \quad z\in\mathbb{C}. \tag{4.29}$$

The last step of Eq. (4.28) is the result of our residuum-only approach and the first equality sign is reached through the aforementioned Sokhotski-Plemelj theorem. The relation to transform the Fermi-function into the imaginary part of a digamma function is the following

$$\mathrm{Im}\Psi^{(0)}\left(\frac{1}{2}+\frac{ix}{2\pi}\right) = \frac{\pi}{p}\left(\frac{1}{2}-f^{p}(x)\right), \quad x\in\mathbb{R},\ p\in\{\pm 1\}. \tag{4.30}$$

The constant $C$ always disappears when summing over the $\alpha$-indices. Therefore, we can drop $C$ from the sequential tunnelling Kernel calculation. The proof can be found in Appendix B. The final expression for the second order Kernel $\mathcal{K}^{(2)}$ is obtained by inserting the energy integral function $Y$ into Eq. (4.26)

$$\mathcal{K}^{(2)}\hat{\rho}^{\infty} = \sum_{\substack{nmp\\ l\,\alpha\,\alpha'}} \alpha\alpha'\,\Gamma^{p}_{l,nm} d_n^{\bar{p},\alpha} d_m^{p,\alpha'} Y_{+}^{\alpha}\left(\beta(\Delta E_{mp\alpha'} - p\mu_l)\right)\hat{\rho}^{\infty}. \tag{4.31}$$

It should be noted that the energy difference $\Delta E_{mp\alpha'}$ depends on the $d_m^{p,\alpha'}$-superoperator. This superoperator will change the density matrix on which then the system Liouvillian $\mathcal{L}_{\mathrm{S}}$ is acting on to retrieve an energy difference $\Delta E$.

## 4.3. Cotunnelling and pair tunnelling

If we include the next leading order in the expansion of the Kernel, we get a Kernel which is valid up to the fourth order: $\mathcal{K} = \mathcal{K}^{(2)} + \mathcal{K}^{(4)} + \mathcal{O}\left(\hat{H}_{\mathrm{T}}^{6}\right)$. This regime of tunnelling events up to fourth order in $\mathcal{L}_{\mathrm{T}}$ is better known as the cotunnelling transport regime. In this regime two new processes are included, namely the cotunnelling ones and pair tunnelling ones (depicted in Figure 1.2). For the fourth order Kernel, we obtain according to Eq. (4.16):

$$\mathcal{K}^{(4)} = \mathcal{P}\mathcal{L}_{\mathrm{T}}\tilde{\mathcal{G}}_0\mathcal{Q}\mathcal{L}_{\mathrm{T}}\mathcal{Q}\tilde{\mathcal{G}}_0\mathcal{Q}\mathcal{L}_{\mathrm{T}}\mathcal{Q}\tilde{\mathcal{G}}_0\mathcal{L}_{\mathrm{T}}\mathcal{P} \tag{4.32}$$

Applying $\mathcal{P}\mathcal{L}_{\mathrm{T}}^{2n+1}\mathcal{P} = 0$ for $n \in \mathbb{N}$ yields:

$$\begin{aligned}\mathcal{K}^{(4)} &= \mathcal{P}\mathcal{L}_{\mathrm{T}}\tilde{\mathcal{G}}_0\mathcal{L}_{\mathrm{T}}\tilde{\mathcal{G}}_0\mathcal{Q}\mathcal{L}_{\mathrm{T}}\tilde{\mathcal{G}}_0\mathcal{L}_{\mathrm{T}}\mathcal{P} \\ &= \mathcal{P}\mathcal{L}_{\mathrm{T}}\tilde{\mathcal{G}}_0\mathcal{L}_{\mathrm{T}}\tilde{\mathcal{G}}_0\mathcal{L}_{\mathrm{T}}\tilde{\mathcal{G}}_0\mathcal{L}_{\mathrm{T}}\mathcal{P} - \mathcal{P}\mathcal{L}_{\mathrm{T}}\tilde{\mathcal{G}}_0\mathcal{L}_{\mathrm{T}}\mathcal{P}\tilde{\mathcal{G}}_0\mathcal{P}\mathcal{L}_{\mathrm{T}}\tilde{\mathcal{G}}_0\mathcal{L}_{\mathrm{T}}\mathcal{P}.\end{aligned} \tag{4.33}$$

We used hereby also that $\tilde{\mathcal{G}}_0$ commutes with $\mathcal{Q}$ respective $\mathcal{P}$ and $\mathcal{Q}^2 = \mathcal{Q}$ so that the outermost $\mathcal{Q}$-operators vanish and the innermost square to $\mathcal{Q}$. If we let $\mathcal{K}^{(4)}$ act on a density matrix, we get

$$\begin{aligned}\mathcal{K}^{(4)}\hat{\rho}^{\infty} =& \frac{1}{\hbar^4}\sum_{\substack{\{\alpha_i\}\{b_i\}\\\{p_i\}}}\left(\prod_i p_i\right)\mathrm{Tr}_{\mathrm{B}}\Bigg\{c_{b_4}^{p_4,\alpha_4}D_{b_4}^{\bar{p}_4,\alpha_4}\frac{1}{0^+ - \mathcal{L}_{\mathrm{S}} - \mathcal{L}_{\mathrm{B}}}c_{b_3}^{p_3,\alpha_3}D_{b_3}^{\bar{p}_3,\alpha_3} \\ &\frac{1}{0^+ - \mathcal{L}_{\mathrm{S}} - \mathcal{L}_{\mathrm{B}}}c_{b_2}^{p_2,\alpha_2}D_{b_2}^{\bar{p}_2,\alpha_2}\frac{1}{0^+ - \mathcal{L}_{\mathrm{S}} - \mathcal{L}_{\mathrm{B}}}c_{b_1}^{p_1,\alpha_1}D_{b_1}^{\bar{p}_1,\alpha_1}\hat{\rho}^{\infty}\otimes\hat{\rho}_{\mathrm{B}}\Bigg\} \\ &-\frac{1}{\hbar^4}\sum_{\substack{\{\alpha_i\}\{b_i\}\\\{p_i\}}}\left(\prod_i p_i\right)\mathrm{Tr}_{\mathrm{B}}\Bigg\{c_{b_4}^{p_4,\alpha_4}D_{b_4}^{\bar{p}_4,\alpha_4}\frac{1}{0^+ - \mathcal{L}_{\mathrm{S}} - \mathcal{L}_{\mathrm{B}}}c_{b_3}^{p_3,\alpha_3}D_{b_3}^{\bar{p}_3,\alpha_3} \\ &\mathcal{P}\frac{1}{0^+ - \mathcal{L}_{\mathrm{S}}}\mathcal{P}c_{b_2}^{p_2,\alpha_2}D_{b_2}^{\bar{p}_2,\alpha_2}\frac{1}{0^+ - \mathcal{L}_{\mathrm{S}} - \mathcal{L}_{\mathrm{B}}}c_{b_1}^{p_1,\alpha_1}D_{b_1}^{\bar{p}_1,\alpha_1}\hat{\rho}^{\infty}\otimes\hat{\rho}_{\mathrm{B}}\Bigg\}.\end{aligned} \tag{4.34}$$

Bringing the bath operators together with the help of the commutator relation for superoperators and performing the trace on them results in an expectation value of four respective two creation operators. The leftmost bath Louvillian is picking up the energies from the three Louvillians to the right so that a sum of energies is arising:

$$\begin{aligned}\mathcal{K}^{(4)}\hat{\rho}^{\infty} =& -\frac{i}{\hbar}\sum_{\substack{\{\alpha_i\}\{b_i\}\\\{p_i\}}}\left(\prod_i p_i\alpha_i\right)\Bigg[\left\langle c_{b_4}^{p_4,\alpha_4}c_{b_3}^{p_3,\alpha_3}c_{b_2}^{p_2,\alpha_2}c_{b_1}^{p_1,\alpha_1}\right\rangle D_{b_4}^{\bar{p}_4,\alpha_4} \\ &\frac{1}{i0^+ - i\hbar\mathcal{L}_{\mathrm{S}} - \sum_{j=1}^{3}p_j\xi_{b_j}}D_{b_3}^{\bar{p}_3,\alpha_3}\frac{1}{i0^+ - i\hbar\mathcal{L}_{\mathrm{S}} - \sum_{j=1}^{2}p_j\xi_{b_j}}D_{b_2}^{\bar{p}_2,\alpha_2} \\ &\frac{1}{i0^+ - i\hbar\mathcal{L}_{\mathrm{S}} - p_1\xi_{b_1}}D_{b_1}^{\bar{p}_1,\alpha_1}\hat{\rho}^{\infty} \\ &-\left\langle c_{b_4}^{p_4,\alpha_4}c_{b_3}^{p_3,\alpha_3}\right\rangle\left\langle c_{b_2}^{p_2,\alpha_2}c_{b_1}^{p_1,\alpha_1}\right\rangle D_{b_4}^{\bar{p}_4,\alpha_4}\frac{1}{i0^+ - i\hbar\mathcal{L}_{\mathrm{S}} - p_3\xi_{b_3}}D_{b_3}^{\bar{p}_3,\alpha_3}\frac{1}{i0^+ - i\hbar\mathcal{L}_{\mathrm{S}}} \\ &D_{b_2}^{\bar{p}_2,\alpha_2}\frac{1}{i0^+ - i\hbar\mathcal{L}_{\mathrm{S}} - p_1\xi_{b_1}}D_{b_1}^{\bar{p}_1,\alpha_1}\hat{\rho}^{\infty}\Bigg]\end{aligned} \tag{4.35}$$

where $i \in \{1,2,3,4\}$. Wick's theorem for superoperators states (compare appendix A1 of [29]):

$$\begin{aligned}\langle c_4^{\alpha_4} c_3^{\alpha_3} c_2^{\alpha_2} c_1^{\alpha_1} \rangle = &\langle c_4^{\alpha_4} c_3^{\alpha_3} \rangle \langle c_2^{\alpha_2} c_1^{\alpha_1} \rangle \\ &- \alpha_2\alpha_3 \langle c_4^{\alpha_4} c_2^{\alpha_2} \rangle \langle c_3^{\alpha_3} c_1^{\alpha_1} \rangle \\ &+ \alpha_2\alpha_3 \langle c_4^{\alpha_4} c_1^{\alpha_1} \rangle \langle c_3^{\alpha_3} c_2^{\alpha_2} \rangle \end{aligned} \tag{4.36}$$

With the help of this relation, it is possible to simplify our fourth-order Kernel. The first term of the three terms in the result of Wick's theorem is exactly canceling the second term of Eq. (4.35). The two remaining contributions of the relation can be split up in $\mathcal{K}^{(4,D)}$

$$\begin{aligned}\mathcal{K}^{(4,D)}\hat{\rho}^{\infty} = &-\frac{i\hbar}{4\pi^2} \sum_{\substack{\{\alpha_i\}\{b_i\} \\ \{n\}\{m\} \\ \{p\}}} \alpha_1\alpha_4 \int_{-\infty}^{\infty} \mathrm{d}\varepsilon \int_{-\infty}^{\infty} \mathrm{d}\varepsilon' \, \Gamma^{p}_{l,nm}\Gamma^{p'}_{l',n'm'} L(\tilde{W}, \varepsilon - \mu_l) L(\tilde{W}, \varepsilon' - \mu_{l'}) d_n^{\bar{p},\alpha_4} \\ &\frac{f_l^{(p\alpha_1)}(\varepsilon)}{i0^+ - i\hbar\mathcal{L}_{\mathrm{S}} + p\varepsilon} d_{n'}^{\bar{p}',\alpha_3} \frac{1}{i0^+ - i\hbar\mathcal{L}_{\mathrm{S}} + p\varepsilon + p'\varepsilon'} d_{m'}^{p',\alpha_2} \frac{f_{l'}^{(p'\alpha_2)}(\varepsilon')}{i0^+ - i\hbar\mathcal{L}_{\mathrm{S}} + p\varepsilon} d_m^{p,\alpha_1} \hat{\rho}^{\infty} \end{aligned} \tag{4.37}$$

and $\mathcal{K}^{(4,X)}$

$$\begin{aligned}\mathcal{K}^{(4,X)}\hat{\rho}^{\infty} = &\frac{i\hbar}{4\pi^2} \sum_{\substack{\{\alpha_i\}\{b_i\} \\ \{n\}\{m\} \\ \{p\}}} \alpha_1\alpha_4 \int_{-\infty}^{\infty} \mathrm{d}\varepsilon \int_{-\infty}^{\infty} \mathrm{d}\varepsilon' \, \Gamma^{p}_{l,nm}\Gamma^{p'}_{l',n'm'} L(\tilde{W}, \varepsilon - \mu_l) L(\tilde{W}, \varepsilon' - \mu_{l'}) d_n^{\bar{p},\alpha_4} \\ &\frac{f_l^{(p\alpha_2)}(\varepsilon)}{i0^+ - i\hbar\mathcal{L}_{\mathrm{S}} + p\varepsilon} d_{n'}^{\bar{p}',\alpha_3} \frac{1}{i0^+ - i\hbar\mathcal{L}_{\mathrm{S}} + p\varepsilon + p'\varepsilon'} d_{m}^{p,\alpha_2} \frac{f_{l'}^{(p'\alpha_1)}(\varepsilon')}{i0^+ - i\hbar\mathcal{L}_{\mathrm{S}} + p'\varepsilon'} d_{m'}^{p',\alpha_1} \hat{\rho}^{\infty}. \end{aligned} \tag{4.38}$$

The constant part of the density of states is disappearing into the two tunnelling rate matrices $\Gamma^{p}_{l,nm}$ and $\Gamma^{p'}_{l',n'm'}$. It can be shown that this superoperator formalism is equivalent to the ansatz in the dissertation of S. Koller [5]. The difference between these approaches is that the superoperator formalism is treating the problem in the Liouville space and therefore can be mapped into single-path diagrammatics. Koller's approach is performed in the Hilbert space and can by nicely mapped into double-path diagrammatics. Furthermore, she explicitly calculates in her dissertation the real part of these energy integrals of the fourth order Kernel which she calls $D$- and $X$-functions (compare Table 4.1). The next step is to perform the energy integrals of the two fourth order Kernels. The $D$-function is defined by

$$\begin{aligned}&D^{nn'}_{pp'}(\mu,\mu',\Delta) = \\ &-\frac{i\hbar}{4\pi^2} \int_{-\infty}^{\infty} \mathrm{d}x \int_{-\infty}^{\infty} \mathrm{d}x' \frac{f^{(n)}(x)}{i0^+ + p(x-\mu)} \frac{1}{i0^+ + px + p'x' - \Delta} \frac{f^{(n')}(x')}{i0^+ + p(x-\mu')} \end{aligned} \tag{4.39}$$

and the $X$-function reads

$$\begin{aligned}&X^{nn'}_{pp'}(\mu,\mu',\Delta) = \\ &-\frac{i\hbar}{4\pi^2} \int_{-\infty}^{\infty} \mathrm{d}x \int_{-\infty}^{\infty} \mathrm{d}x' \frac{f^{(n)}(x)}{i0^+ + p(x-\mu)} \frac{1}{i0^+ + px + p'x' - \Delta} \frac{f^{(n')}(x')}{i0^+ + p'(x'-\mu')}. \end{aligned} \tag{4.40}$$

The analytic epression of the two integrals can be found in Appendix C. Using these two definitions $\mathcal{K}^{(4)}$ will simplify to

$$\begin{aligned}\mathcal{K}^{(4)}\hat{\rho}^{\infty} &= \left[\mathcal{K}^{(4,D)} + \mathcal{K}^{(4,X)}\right]\hat{\rho}^{\infty} \\ &= \sum_{\substack{\{\alpha_i\}\{b_i\}\\ \{n\}\{m\}\\ \{p\}}} \alpha_1\alpha_4\beta\,\Gamma^{p}_{l,nm}\Gamma^{p'}_{l',n'm'}\Big[D^{\alpha_1\alpha_2}_{++}(\square,\odot,\bullet)d^{\bar{p},\alpha_4}_{n}d^{\bar{p}',\alpha_3}_{n'}d^{p',\alpha_2}_{m'}d^{p,\alpha_1}_{m} \\ &\quad + X^{\alpha_1\alpha_2}_{++}(\square,\star,\bullet)d^{\bar{p},\alpha_4}_{n}d^{\bar{p}',\alpha_3}_{n'}d^{p,\alpha_2}_{m}d^{p',\alpha_1}_{m'}\Big]\hat{\rho}^{\infty}\end{aligned} \tag{4.41}$$

with $\square = \beta(\mu_{j_3} - p\mu_l)$, $\odot = \beta(\mu'_{j_1} - p\mu_l)$, $\bullet = \beta(\Delta_{j_2} - p\mu_l - p'\mu_{l'})$ and $\star = \beta(\mu'_{j_1} - p'\mu_{l'})$ where the inverse of the temperature enters via $\beta$ and the chemical potential of the respective leads via $\mu_l$ (compare Appendix C). The subscripts $\{j_1, j_2, j_3\}$ of the energy differences $\mu', \Delta$ and $\mu$ indicate that these energies depend on the variables of the first $(\alpha_1, p, m)$, two first respective three first $d$-superoperators.

## 4.4. Diagrammatics

In this section, we will discuss the diagrammatic representation of the Kernel of Eq. (4.16) which was introduced by Gerd Schön, Herbert Schoeller and Jürgen König [32, 33]. This helps us to identify and visualize the underlying tunnelling processes. At first, we want to introduce a double-path diagrammatics with its two time lines which represent a forward and backward propagation on a Keldysh contour [5, 27]. At the end, we want to draw a comparison between the latter and a single-time line diagrammatics which is more compact and which represents the Liouville space in a more straightforward way [29].

Starting with the two-time line diagrams, we notice the general structure of the GME of Eq. (4.17). Every final state ($|\Psi_b\rangle\langle\Psi_{b'}|$) is obtained from initial states ($|\Psi_a\rangle\langle\Psi_{a'}|$) which will be transformed via tunnelling events contained in the Kernel.

$$\begin{aligned}\langle\Psi_b|\,\dot{\hat{\rho}}^{\infty}\,|\Psi_{b'}\rangle = \dot{\hat{\rho}}^{\infty}_{bb'} = 0 &= -\frac{i}{\hbar}\sum_{a'a}\delta_{ab}\delta_{a'b'}\left(E_a - E'_a\right)\rho_{aa'} + \sum_{a'a}K^{aa'}_{bb'}\,\hat{\rho}^{\infty}_{aa'} \\ &\coloneqq \delta_{ab}\delta_{a'b'}\left(\begin{array}{ccc} |\Psi_b\rangle & \longleftarrow & |\Psi_a\rangle \\ & & \hat{\rho}^{\infty}_{aa'} \\ \langle\Psi_{b'}| & \longrightarrow & \langle\Psi_{a'}| \end{array}\right) \\ &\quad + \sum_{a'a}\left(\begin{array}{ccc} |\Psi_b\rangle & \longleftarrow & |\Psi_a\rangle \\ & & \hat{\rho}^{\infty}_{aa'} \\ \langle\Psi_{b'}| & \longrightarrow & \langle\Psi_{a'}| \end{array}\right).\end{aligned} \tag{4.42}$$

The first part of the equation is the coherent part which directly stems from the system Liouvillian $\mathcal{L}_{\mathrm{S}}$ and can be seen as a free propagation of one specific state. The second

part with the grey block in the middle represents all tunnelling events arising from the perturbation expansion of the tunnelling Hamiltonian. Approximating the Kernel up to sequential tunnelling will lead to the following eight diagrams:

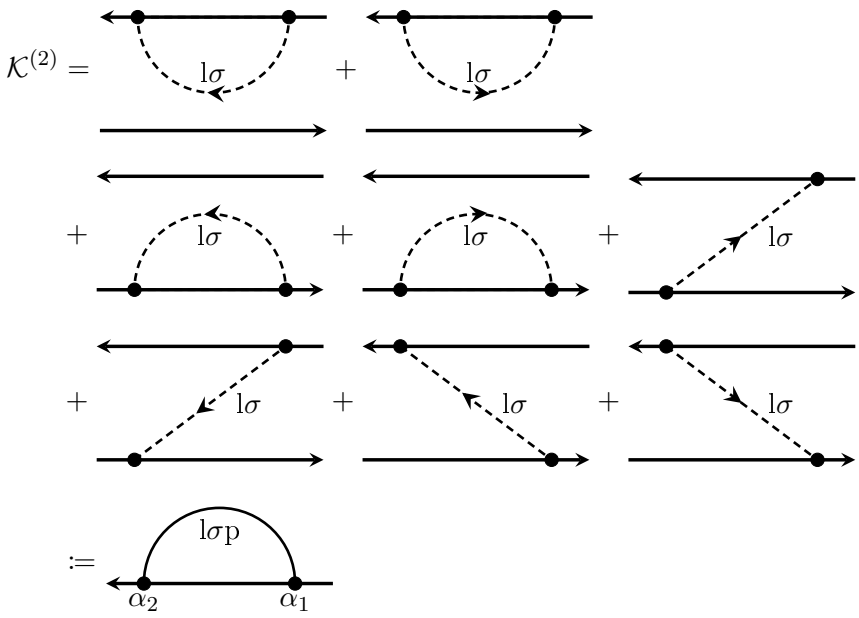


(4.43)

The two black vertices represent the two $D_n^{p,\alpha}$-operators of the Kernel. They are connected via a dotted line which stands for a Wick contraction. The Wick contraction will result in a Fermi-function (compare Eq. (4.23)) and thus the dotted line connecting two dots can be further specified with the lead index $l$, the lead spin $\sigma$ and the $p$ index which governs the direction of this fermionic line. As an example, one could take the first diagram of Eq. 4.43 where we see that the rightmost and therefore time-wise the first tunnelling vertex is connected to an out-tunnelling event. It can be seen as an electron with spin $\sigma$ which is annihilated in the system and transferred to the $l$-lead. The tunnelling rate matrix $\Gamma^p_{l,nm}$ is incorporated in the two $D_n^{p,\alpha}$-operators and can set a specific diagram a priori to zero. It should be emphasized that the lead spin in the two connected tunnelling events is always preserved but it is not in general true that a spin up injected electron will create a spin up electron with respect of the dot system. To each diagram a certain $Y$-function is associated which will weigh a specific tunnelling event similar to the entry of the tunnelling rate matrix. $D_n^{p,\alpha}$-operators on the upper/lower contour have an index $\alpha = \pm 1$ and act from the left/right on the density matrix. The last diagram of Eq. (4.43) is a single-time line diagram. By summing up the variables $p, \alpha_1$ and $\alpha_2$, the eight sequential tunnelling diagrams of the two-time line diagrammatics are recovered. In Table 4.1, we find a comparison of these two concepts.

Furthermore, we want to direct the interested reader for the transformation of the diagrams into the analytic form and vice versa to the appendix A1 of the dissertation of M. Niklas [34]. With these so-called diagrammatic rules, it is possible to rephrase the lengthy tunnelling contributions into compact diagrams and visualize them. At this point, we will give an example of a cotunnelling diagram of the $D$-type in both diagrammatics. To highlight the physical interpretation of the diagrams, we opted to project these diagrams already on the exemplary initial density matrix $|0\rangle\langle 0|$ of an single quantum dot with the

four available states $\{|0\rangle, |\uparrow\rangle, |\downarrow\rangle, |2\rangle\}$:

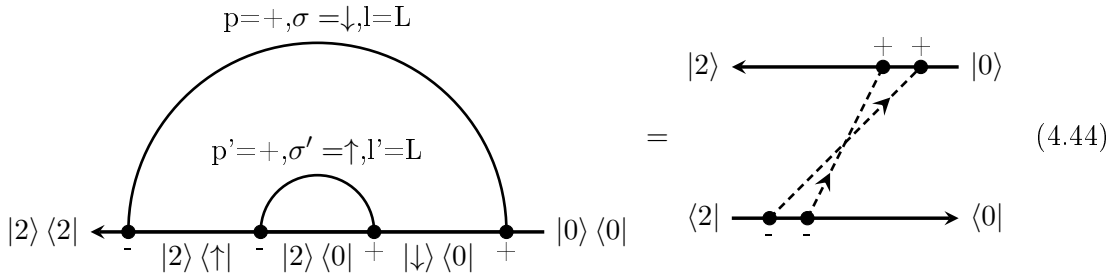


(4.44)

The depicted diagrams can be classified as pair tunnelling events where to electrons - in this case from the left lead - enter into the system (compare Figure 1.2). The $p/p'$-indices together with the $\alpha$-indices which are depicted below the tunnelling vertices, indicate that two electrons are created in the system part. The $\sigma/\sigma'$-indices tell us that the created electrons have opposite spin. Fixing all the indices will lead to three different virtual intermediate states during the tunnelling event and their energies will be then the parameters of the respective $D$-function.

| | Hilbert space | Liouville space |
|---|---|---|
| Equation of motion | $\|\dot{\Psi}\rangle = -\frac{i}{\hbar}\hat{H}\|\Psi\rangle$ | $\dot{\hat{\rho}} = \mathcal{L}\hat{\rho}$ |
| Evolutors | $\hat{U}(t,0) = e^{-i/\hbar\hat{H}t}$ | $\mathcal{G}(t,0) = e^{\mathcal{L}t}$ |
| Free evolution | $\hat{U}_0(t,0)\|\Psi_a\rangle\langle\Psi_{a'}\|\hat{U}_0^\dagger(t,0)$ | $\mathcal{G}_0(t,0)\,\hat{\rho}_{aa'}$ |
| Diagrammatics of a free evolution | 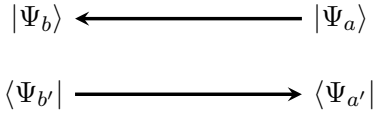  | 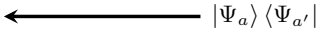  |
| $D$-type diagrams | 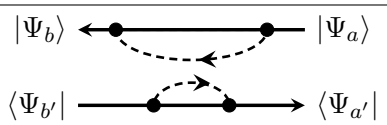  |   |
| $X$-type diagrams | 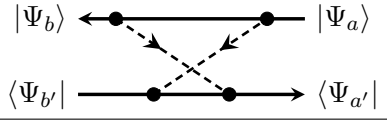  |   |

**Table 4.1 | Comparison of the Hilbert space and the Liouville space**

## 4.5. Current Kernel

In close analogy to the Liouvillian $\mathcal{L} = \mathcal{L}_S + \mathcal{K}$ with its (time evolution) Kernel $\mathcal{K} = \mathcal{K}^{(2)} + \mathcal{K}^{(4)}$ which was derived in the previous sections, we can find the so-called current Kernel. The reasoning starts with Eq. (3.19) where we know that the expectation value of every operator can be deduced from the density matrix. The current is defined as the

derivative of the particle number up to a prefactor with the elementary charge e:

$$\begin{aligned} I_l &= -\mathrm{e}\frac{\mathrm{d}}{\mathrm{dt}}\left\langle \hat{N}_l \right\rangle = -\mathrm{e}\frac{\mathrm{d}}{\mathrm{dt}}\mathrm{Tr}\left\{\hat{N}_l\hat{\rho}(t)\right\} = -\mathrm{e}\,\mathrm{Tr}\left\{-\hat{N}_l\frac{i}{\hbar}\Big[\hat{H}_{\mathrm{tot}},\hat{\rho}(t)\Big]\right\} \\ &= \mathrm{e}\frac{i}{\hbar}\mathrm{Tr}\left\{\hat{N}_l\hat{H}_{\mathrm{tot}}\hat{\rho}(t)\right\} - \mathrm{e}\frac{i}{\hbar}\mathrm{Tr}\left\{\hat{N}_l\hat{\rho}(t)\hat{H}_{\mathrm{tot}}\right\} = \mathrm{Tr}\left\{\mathrm{e}\frac{i}{\hbar}\Big[\hat{N}_l,\hat{H}_{\mathrm{tot}}\Big]\hat{\rho}(t)\right\} \\ &= \mathrm{Tr}\left\{\mathrm{e}\frac{i}{\hbar}\Big[\hat{N}_l,\hat{H}_{\mathrm{T}}\Big]\hat{\rho}(t)\right\} = \mathrm{Tr}\left\{\hat{I}_l\hat{\rho}(t)\right\} = \mathrm{Tr}\left\{\hat{I}_l\mathcal{Q}\hat{\rho}(t)\right\}. \end{aligned} \tag{4.45}$$

Due to the cyclic property of the trace, we can combine the particle number operator of the $l$-lead $\hat{N}_l = \sum_{\sigma\mathbf{k}}\hat{c}^\dagger_{l\sigma\mathbf{k}}\hat{c}_{l\sigma\mathbf{k}}$ again with the total Hamiltonian $\hat{H}_{\mathrm{tot}}$. In the second last step, we obtain the definition of the current operator $\hat{I}_l$ of the $l$-lead. In the last step, we use the fact that one can concentrate itself only on the entangled part $\mathcal{Q}\hat{\rho}(t)$ of the density operator. The part $\mathcal{P}\hat{\rho}(t)$ is always diagonal in the bath basis and does therefore not contribute to the current due to the odd number of lead operators in the current operator. The procedure is now very similar to the one of the time evolution Kernel. We plug Eq. (4.6) into Eq. (4.45) and obtain

$$I_l = \mathrm{Tr}\left\{\hat{I}_l\int_0^t \mathrm{d}s\; \mathcal{G}_{\mathcal{Q}}(t-s)\mathcal{Q}\mathcal{L}\mathcal{P}\hat{\rho}(s)\right\} = \mathrm{Tr}\left\{\int_0^t \mathrm{d}s\; \mathcal{K}^I_l(t-s)\mathcal{L}\mathcal{P}\hat{\rho}(s)\right\} \tag{4.46}$$

with the current Kernel $\mathcal{K}^I_l(t)$ defined as $\mathcal{K}^I_l(t) = \mathcal{P}\hat{I}_l\bar{G}_{\mathcal{Q}}(t)\mathcal{L}_{\mathrm{T}}\mathcal{P}$ and $\mathcal{K}^I_l = \lim_{\lambda\to 0^+}\tilde{\mathcal{K}}^I_l(\lambda)$. The stationary current is then given by

$$I^\infty_l = \mathrm{Tr}_{\mathrm{B}}\left\{\hat{I}_l\sum_{n=0}^{\infty}\Big(\tilde{\mathcal{G}}_0\mathcal{Q}\mathcal{L}_{\mathrm{T}}\mathcal{Q}\Big)^{2n}\tilde{\mathcal{G}}_0\mathcal{L}_{\mathrm{T}}\hat{\rho}^\infty\otimes\hat{\rho}_{\mathrm{B}}\right\} \tag{4.47}$$

if the same steps are taken as in section 4.1 in respect with the Laplace transformation. In comparison with the time evolution Kernel (Eq. (4.16)) just the first $\mathcal{L}_{\mathrm{T}}$ is substituted by the current operator. Therefore the calculation of the current kernel is very similar. There are three modifications with respect to the diagrams of time evolution Kernel:

- **Lead index:** The lead index $l$ of the current operator $\hat{I}_l$ fixes the $l$-index of the last (leftmost) vertex. No summation over the fermionic line connected to the last vertex is therefore needed.

- **Position of last vertex:** The current operator $\hat{I}_l$ is a left superoperator. For this reason, the last vertex is fixed on the upper contour (two-time line diagrammatics) or generally, this $\alpha$-index is fixed to $+1$.

- **Direction of last fermion line:** The sign of the diagrams where the fermionic line points away from the last so leftmost vertex has to be inverted. This difference stems from a sign difference in $\hat{H}_{\mathrm{T}}$ in respect with $\hat{I}_l$ (compare Eq. (2.5) with Eq. (4.46)).

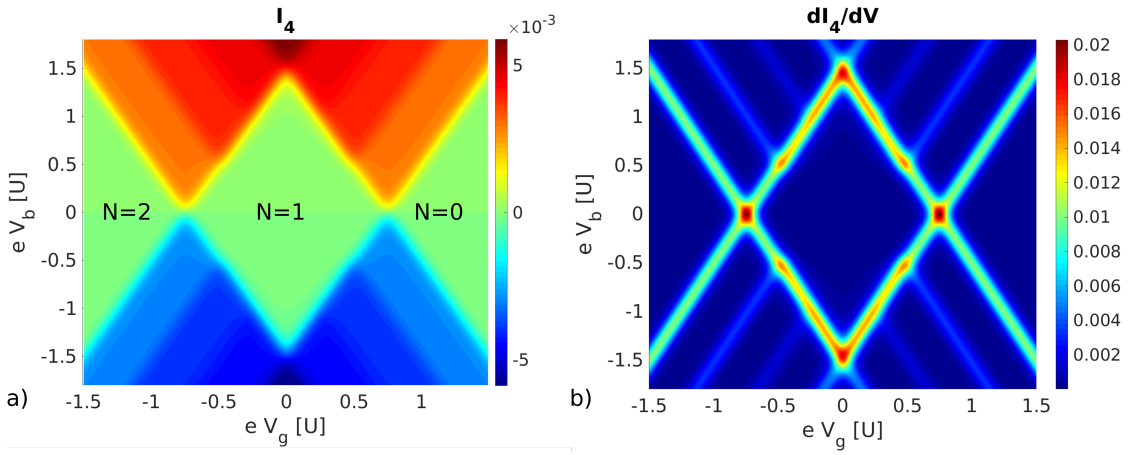


**Figure 4.1 | Current and differential conductance of a single quantum dot with exited states due to Zeeman splitting: a)** Fourth order current of an Anderson impurity model with the Hamiltonian of Eq. (2.4) which is additionally made particle-hole symmetric. The green areas represent the Coulomb diamonds (e.g. the one with particle number $N = 1$) where the current is strongly suppressed. The parameters are the following and all measured in units of the Coulomb interaction $U = 1$: $T = 0.033$, $E_z = 0.5$, $W = 10^{50}$ and a diagonal $\Gamma$ with a coupling strength of 0.006. The gate and the bias voltage are both as well measured in units of $U$ so that the particle number rises from the right to the left. **b)** Differential conductance $dI_4/dV$ in a so-called stability diagram. The excited transition lines due to Zeeman splitting can be seen clearly. In the Coulomb blockade region, there is enhanced current through cotunnelling events in comparison with only sequential tunnelling.

## 4.6. Transport code implementation

In this section, we will shortly address the topic of the transport code implementation of the just-introduced theory. The main goal of this implementation is to rigorously include coherences within the cotunnelling transport regime. Furthermore, we want to be as generic as possible in terms of the specification of the treated systems, e.g. we want to easily change the leads by giving them a spin polarization or change the size of the central system. We are aware that there are already other codes (e.g. [35]) which are capable of treating the cotunnelling transport regime with coherences but they are not as easily applicable to more sophisticated systems due to their numerical expensiveness.

In the past, we used, among others, the program called KinEq which was written by M. Leijnse, M. R. Wegewijs and S. Koller [5, 36]. This transport code is well optimized in terms of calculation time but there is a problem in the way how it treats coherences. It fully incorporates the second order coherences via the principal part of the $Y$-function but not fourth order coherences where one would need the imaginary part of the cotunnelling integrals $D$ and $X$. The line of argumentation which justifies their procedure of still having a consistent fourth order Kernel is based on a splitting of the Kernel in a secular part of only populations and a general non-secular part [5]. However, if one has to deal with coherences which are quasi-degenerate, this ansatz cannot justify anymore a proper treatment of the problem. By contrast, we can confidently claim that with our newly implemented code, we can treat also the dynamics of all coherences up to fourth order. On the other side, we

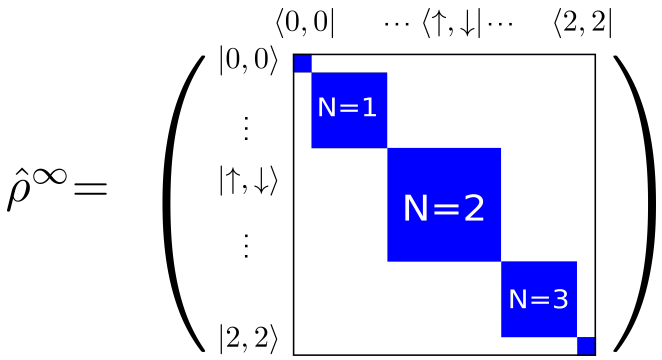


**Figure 4.2 | Double quantum dot reduced density matrix of the steady state:** The diagonal elements are the populations and the off-diagonal elements are the coherences. In general, the size of the reduced density matrix of a double quantum dot is of size $16 \times 16$ due to its 16 states $\{|0,0\rangle, |\uparrow,0\rangle, |0,\uparrow\rangle, |\downarrow,0\rangle, ..., |2,2\rangle\}$ which are depicted in a number representation. The general Kernel would be then of size $256 \times 256$. Due to the conservation of total particle number, the entries, which have to be considered, are reducing drastically (blue blocks). It is obvious that with increasing system size the exact treatment of all states soon becomes unfeasible - even just in the blue blocks of defined particle number.

enter into a way more complicated realm due to the sheer number of coherences when we consider bigger systems with many degenerate or quasi-degenerate states.

In the previous sentences, we justified the way, namely to include all coherences up to fourth order, how we are setting up the code and now we will come to the actual description of it. It should be emphasized that this description is to no point complete but rather will focus on the overall picture. The numerical computing environment for this project was chosen to be MATLAB. Usually, we want to calculate the current in a gate voltage-bias voltage-map (see Figure 4.1 a)). At every point in this voltage landscape, we set up time the evolution Kernel - if desired up to fourth order. According to the modifications explained in section 4.5, we easily can deduce from the time evolution Kernel $\mathcal{K}$ also the current Kernel $\mathcal{K}_l^I$ which is just a subset of it. The steady-state density matrix $\hat{\rho}^\infty$ can be then calculated (compare Eq. (4.17)) by

$$0 = \left(\mathcal{L}_\mathrm{S} + \mathcal{K}^{(2)} + \mathcal{K}^{(4)}\right)\hat{\rho}^\infty \tag{4.48}$$

with keeping in mind the definition of the system Liouvillian $\mathcal{L}_\mathrm{S}\hat{X} = -\frac{i}{\hbar}\left[\hat{H}_\mathrm{S}, \hat{X}\right]$. Fortunately, we can reduce the number of non-zero entries of the steady-state density matrix due to the conservation law of total particle number (see Figure 4.2). With additional conservation laws, we can further reduce the acquired block-diagonal structure of the density matrix. For example, we can exclude coherences between states of different total spin number (conservation of total spin). Solving Eq. (4.48) can be a tough mathematical problem in its own. During this work, we faced at several occasions numerical instabilities due to an inadequate solution of this task where the result can be then highly inaccurate. We use the built-in *eigs*-function of MATLAB to solve the equation and find then the eigenvector of the eigenvalue which is closest to zero. The *eigs*-function of MATLAB uses an Arnoldi algorithm to find the eigenvectors respective the eigenvalues [37]. If there are many eigenvalues which fulfill this condition of being close to the value of zero, then it can happen that we do not find the correct eigenvector. It should be emphasized that we are aware

of more sophisticated ways, namely using a preconditioner (compare [38]), to tackle this problem but at this stage we do not focus on this. The focus of the implementation is more on the crucial step to calculate the time evolution Kernel via the diagrammatic technique as accurately as possible while at the same time not using too much computational power. The time-consuming part is the one of the calculation of the $D$- and $X$-functions. The reason for that is the fact that the analytical expressions of them (compare Appendix C) include sums which in principle go up to infinity. To speed up the calculations, we first of all choose to split them up into different cases where the involved energy differences share certain properties like e.g. $\mu = \mu'$ and $\Delta = 0$ in the case of $D.i$ . There, the sum of a digamma function with two denominators of the general case disappears and therefore speeds up the evaluation. In the general cases, we truncate the sums in the following way, here exemplary shown for a part of the $D$-function:

$$\begin{aligned}
&\frac{inn'}{2\pi}\sum_{k=0}^{\infty}\frac{\Psi^{(0)}\left(1+k+\frac{i\Delta}{2\pi}\right)}{\left(k+\frac{1}{2}+\frac{i\mu}{2\pi}\right)\left(k+\frac{1}{2}+\frac{i\mu'}{2\pi}\right)}\\
&\approx\frac{inn'}{2\pi}\left[\sum_{k=0}^{N-1}\frac{\Psi^{(0)}\left(1+k+\frac{i\Delta}{2\pi}\right)}{\left(k+\frac{1}{2}+\frac{i\mu}{2\pi}\right)\left(k+\frac{1}{2}+\frac{i\mu'}{2\pi}\right)}\right.\\
&\left.+\sum_{k=0}^{\infty}\frac{\Psi^{(0)}\left(1+k+N\right)}{\left(k+\frac{1}{2}+N\right)^2}+\mathcal{O}(\Delta)+\mathcal{O}(\mu)+\mathcal{O}(\mu')\right].
\end{aligned}\tag{4.49}$$

We noticed that if we truncate the sum up to a certain number there is a slowly converging shift in comparison to the exact result. If we add the first term of a Taylor expansion in the three energy parameters to the truncated sum, then we compensate this shift. The truncation is chosen so that $(N-1) \gg |\beta(\max(\mu,\mu'))/(2\pi)|$.

Another time-consuming part is the calculation of the intermediate energies which will be then the arguments of the $D$- and $X$-functions. These energies stem from the product of the four creation-/annihilation-operators (compare Eq. (4.41)) and they can be seen as different paths to reach a certain final state. In the code, a huge speedup is achieved if we precalculate this product of the $d_n^{p,\alpha_i}$-operators for every set of parameters $\{\alpha_i\},\{n\},\{m\},\{p\}$. We can store then all the paths which are associated with one diagram in an energy independent tensor (compare Table 4.2). This tensor can be finally used for the whole voltage landscape.

| Final state: $\|\Psi_b\rangle\langle\Psi_{b'}\|$ | $\mu$-state | $\Delta$-state | $\mu'$-state | Initial state: $\|\Psi_a\rangle\langle\Psi_{a'}\|$ |
|---|---|---|---|---|
| $\|2,2\rangle\langle 2,2\|$ | $\|\downarrow,2\rangle\langle 2,2\|$ | $\|\downarrow,\downarrow\rangle\langle 2,2\|$ | $\|\downarrow,2\rangle\langle 2,2\|$ | $\|2,2\rangle\langle 2,2\|$ |
| $\|2,\uparrow\rangle\langle 2,\uparrow\|$ | $\|\downarrow,\uparrow\rangle\langle 2,\uparrow\|$ | $\|\downarrow,0\rangle\langle 2,\uparrow\|$ | $\|\downarrow,\uparrow\rangle\langle 2,\uparrow\|$ | $\|2,\uparrow\rangle\langle 2,\uparrow\|$ |
| $\|\uparrow,\uparrow\rangle\langle\uparrow,\uparrow\|$ | $\|0,\uparrow\rangle\langle\uparrow,\uparrow\|$ | $\|0,0\rangle\langle\uparrow,\uparrow\|$ | $\|0,\uparrow\rangle\langle\uparrow,\uparrow\|$ | $\|\uparrow,\uparrow\rangle\langle\uparrow,\uparrow\|$ |
| ... | ... | ... | ... | ... |

**Table 4.2 | Precalculation of intermediate paths for the cotunnelling energy integrals:** A specific diagram allows only some transitions from an intial state $|\Psi_a\rangle\langle\Psi_{a'}|$ to a final state $|\Psi_b\rangle\langle\Psi_{b'}|$. In this table, an exemplary diagram which is determined by a certain configuration of its $d$-operators is chosen ($d_n^{\bar{p},\alpha_4} d_{n'}^{\bar{p}',\alpha_3} d_{m'}^{p',\alpha_2} d_m^{p,\alpha_1} \rightarrow d_{\uparrow L}^{+,+} d_{\uparrow R}^{+,+} d_{\uparrow R}^{-,+} d_{\uparrow L}^{-,+}$). It is a $D$-type diagram where all the superoperators act from the left on the density matrix due to the $\alpha$-indices. The density matrix which we are looking at in this example is one of a double dot with four single-particle states $\{|\uparrow L\rangle, |\uparrow R\rangle, |\downarrow L\rangle, |\downarrow R\rangle\}$. Before going through the whole voltage landscape, we identify the paths which are connected to each diagram and store them in a tensor. For the actual calculation of the Kernel with a given bias and gate voltage, we just have to calculate the value of the possible energies but not again the paths itself, plug them into the $D$-function and place the result according to the initial respective final state in the correct position of the Kernel.

# Part III.

# Model systems

# 5

# Spin resonance model

In this chapter, we will focus on transport through a single and a double quantum dot in the spin valve configuration. In this setup, one can find spin resonance lines in the stability diagram which are due to a mixing of spin channels induced by an effective exchange field. This setup is ideal for comparing the results of the self-implemented transport code of the cotunnelling regime with existing numerical transport data. In this respect, we have to mention the work of M. Hell et al. where they analyze such a spin resonance in a single quantum dot [35]. We will dedicate the first section to the explanation of this mechanism and afterwards, we will show explicitly the effect of including cotunnelling events to the transport calculations. In the second section of this chapter, we will go beyond the Anderson impurity model and extend their work by looking at a parallel double quantum dot and analyze its spin resonance lines with the help of our found equations of motion.

## 5.1. Single quantum dot spin resonance

In order to obtain a spin resonance line inside the Coulomb blockade region, three points are crucial. First of all, we need to have degenerate or almost degenerate states in our system. This is achieved when we do not apply an external magnetic field to the quantum dot so that the spin up and spin down levels have the same energy. As we have pointed out already in the introduction, this is a necessary condition for interference effects to appear. The second point is - again another prerequisite of interference effects - the existence off-diagonal elements in the tunnelling rate matrices which can be associated with the tunnelling behaviour of the two leads. To be more precise, we do not need them just to be off-diagonal rather them not to share a common eigenbasis with the energy eigenbasis of the central system. With this condition, we are sure that there is not another basis where these three constituents, namely right lead, leaf lead and central system, can be diagonalized at the same time. The last point for the existence of a spin resonance line is that we need the setup to be in the so-called spin valve configuration which we achieve e.g. with ferromagnetic leads of almost antiparallel alignment [39]. The mechanism of a spin valve setup is explained in more detail in Figure 5.1. First of all, we define the Hamiltonian of the quantum dot $\hat{H}_0$ (compare Eq. (2.3)):

$$\hat{H}_0 = \sum_{\zeta=\{\uparrow,\downarrow\}} \left(\varepsilon_0 - \frac{U}{2}\right) \hat{d}^\dagger_\zeta \hat{d}_\zeta + U \hat{d}^\dagger_\uparrow \hat{d}_\uparrow \hat{d}^\dagger_\downarrow \hat{d}_\downarrow. \tag{5.1}$$

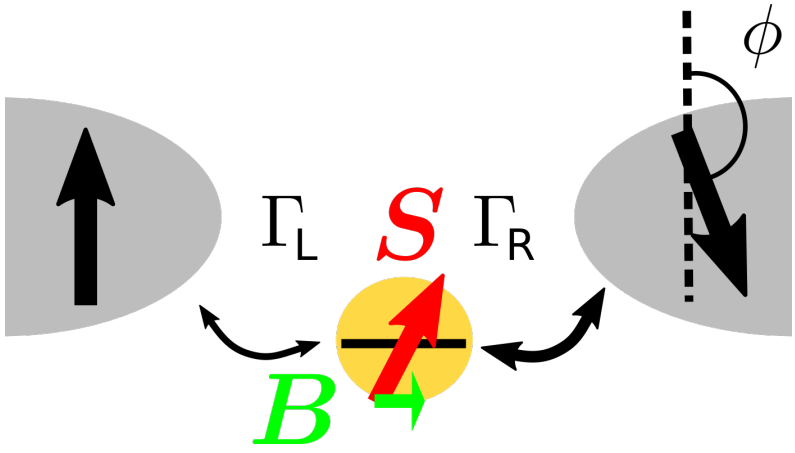


**Figure 5.1 | General setup of a single quantum dot in the spin valve configuration:** The two black arrows indicate the polarization unit vectors $\boldsymbol{n}_{\mathrm{L/R}}$ of the two leads which are in this case almost antiparallel aligned so that the angle between them is approaching $\phi = \pi$. If now one electron with the spin from the left lead enters into the system, there is almost no possibility for this electron to leave the system through the right lead. The red arrow symbolizes the spin of the central system $\boldsymbol{S}$. The effective magnetic field $\boldsymbol{B}$ which stems from an interplay of spin polarization and electrical correlations on the dot will induce a spin precession. With the thickness of the arrows between the dot and the leads, the asymmetry in the coupling should be emphasized. At the vectorial resonance condition of maximum precession (compare Eq. (5.7)) the spin valve effect is partly lifted and a spin resonance line appears (see Figure 5.2).

To account for the spin polarization, we choose the tunnelling rate matrix for the $l$-lead to have the following form:

$$\Gamma^{p}_{l,nm} = \sum_{\sigma} \frac{2\pi}{\hbar} \bar{g}_{l\sigma} t^{\bar{p}}_{l\sigma,n} t^{p}_{l\sigma,m} = \left[\Gamma^{0}_{l} \left(\mathbb{1}_2 + P_l \boldsymbol{n}_l \cdot \boldsymbol{\sigma}\right)\right]^{p}_{nm} . \tag{5.2}$$

An upper index $p = -1$ of the matrix in the last step does not change the matrix while $p = +1$ will transpose the matrix (compare Eq. (4.25)). The spin-averaged coupling strength of the tunnelling rate matrix $\Gamma^{0}_{l}$ is defined by half of the trace of the given matrix. The polarization of the $l$-lead is entering this formula via $P_l$ and the polarization unit vector of the $l$-lead via $\boldsymbol{n}_l$. The vector $\boldsymbol{\sigma}$ contains the Pauli-matrices $\sigma$ as entries:

$$\sigma_x = \begin{pmatrix} 0 & 1 \\ 1 & 0 \end{pmatrix}, \sigma_y = \begin{pmatrix} 0 & -i \\ i & 0 \end{pmatrix}, \sigma_z = \begin{pmatrix} 1 & 0 \\ 0 & -1 \end{pmatrix}. \tag{5.3}$$

From now on, we will use bold symbols to denote vectors. In Figure 5.2, the transport data of the self-implemented code is shown. Before explaining all the details of the plots, we first want to give all the tools which are necessary for a full understanding of the mechanism. To define the state of a single quantum dot, we need in principle six parameters: the three populations ($p_0$, $p_1$ and $p_2$) and the three components of the spin $\boldsymbol{S}$. The components of the spin are defined by the expectation values of the spin operators $\hat{S}_i$

$$\hat{S}_i = \frac{1}{2} \sum_{\zeta,\zeta'} \hat{d}^{\dagger}_{\zeta'} \left[\sigma_i\right]_{\zeta\zeta'} \hat{d}_{\zeta'} \tag{5.4}$$

with $i = x, y, z$. The equations of motion which follow from this setup are

$$\dot{p}_0 = -2\gamma_{10}^{+} p_0 + \gamma_{10}^{-} p_1 + 2\boldsymbol{\gamma}_{10}^{-} \cdot \boldsymbol{S}, \tag{5.5a}$$
$$\dot{p}_1 = 2\gamma_{10}^{+} p_0 - \left(\gamma_{10}^{-} + \gamma_{21}^{+}\right) p_1 + 2\gamma_{21}^{-} p_2 - 2\left(\boldsymbol{\gamma}_{10}^{-} - \boldsymbol{\gamma}_{21}^{+}\right) \cdot \boldsymbol{S}, \tag{5.5b}$$
$$\dot{p}_2 = \gamma_{21}^{+} p_1 - 2\gamma_{21}^{-} p_2 - 2\boldsymbol{\gamma}_{21}^{+} \cdot \boldsymbol{S}, \tag{5.5c}$$
$$\dot{\boldsymbol{S}} = \boldsymbol{\gamma}_{10}^{+} p_0 + \left(-\tfrac{1}{2}\boldsymbol{\gamma}_{10}^{-} + \tfrac{1}{2}\boldsymbol{\gamma}_{21}^{+}\right) p_1 - \boldsymbol{\gamma}_{21}^{-} p_2 - \left(\gamma_{10}^{-} + \gamma_{21}^{+}\right) \boldsymbol{S} - \boldsymbol{S} \times \boldsymbol{B} \tag{5.5d}$$

with $\gamma_{\mathrm{nm}}^{\pm} = \sum_l \gamma_{l,\mathrm{nm}}^{\pm}$ and $\gamma_{l,\mathrm{nm}}^{\pm} = \Gamma_l^0 f_l^{\pm}(\varepsilon - \mu_{\mathrm{nm}})$ where $\mu_{\mathrm{nm}}$ is the energy difference between the state n and the state m. The vectorial form is defined by $\boldsymbol{\gamma}_{\mathrm{nm}}^{\pm} = \sum_l \boldsymbol{n}_l P_l \gamma_{l,\mathrm{nm}}^{\pm}$. Out of an analysis of these equations, we can deduce two things. Firstly, we encounter in the last term of Eq. (5.5d) a part which acts as if it would be a magnetic field thus will be called effective magnetic field $\boldsymbol{B}$:

$$\boldsymbol{B} = \sum_l 2P_l\Gamma_l^0 \mathrm{Im}\left(Y_+^+(\mu_{10} - \mu_l) - Y_+^+(\mu_{21} - \mu_l)\right) \boldsymbol{n}_l \tag{5.6}$$

In other sources, the same field is referred to an exchange field. The effective magnetic field is induced by Coulomb interaction and is characterized by the difference of the principal parts of the $Y$-function and thus by the real part of the digamma functions (compare Eq. (4.28)). This effective magnetic field can be seen as a many-body interaction effect which will vanish if the Coulomb interaction $U$ becomes zero. The effective magnetic field $\boldsymbol{B}$ causes precession of the spin $\boldsymbol{S}$ but it also generates a spin splitting of order $\Gamma_l^0$. Due to this precession, an electron captured in a spin valve configuration can now turn its spin in order to leave the dot which results in a lifting of the spin valve. This lifting effect can only appear if our system stays in a coherent state for a certain time to be able to precess. Coherence, as we have pointed out already a couple of times, is described by the off-diagonal elements of the tunnelling rate matrix. For a coherent state in the reduced density matrix where we traced out the leads and the tunnelling rate matrices are tilted, we need inevitably the off-diagonal elements of the reduced density matrix, namely the coherences, to describe such a state. It is therefore reasonable why in $\boldsymbol{B}$ the principal parts which are connected to the dynamics of the coherences appear. In the work of M. Hell, they gave a vectorial argument for the lifting of the spin valve [35]:

$$\boldsymbol{B} \cdot \boldsymbol{n}_{\mathrm{L}} = (B_{\mathrm{L}}\boldsymbol{n}_{\mathrm{L}} + B_{\mathrm{R}}\boldsymbol{n}_{\mathrm{R}}) \cdot \boldsymbol{n}_{\mathrm{L}} = \left(\left(B_{\mathrm{L}} + B_{\mathrm{R},\parallel}\right)\boldsymbol{n}_{\mathrm{L}} + B_{\mathrm{R},\perp}\boldsymbol{n}_{\perp}\right) \cdot \boldsymbol{n}_{\mathrm{L}} = B_{\mathrm{L}} + B_{\mathrm{R},\parallel} = 0 \tag{5.7}$$

They argue that this is the condition of maximum precession. The magnetic field can be split up into one part stemming from the left lead $B_{\mathrm{L}}\boldsymbol{n}_{\mathrm{L}}$ and one from the right lead $B_{\mathrm{R}}\boldsymbol{n}_{\mathrm{R}}$ (compare Eq. (5.6)). It is possible to reexpress the part from the right lead into one which is perpendicular to left lead $B_{\mathrm{R},\perp}\boldsymbol{n}_{\perp} = B_{\mathrm{R}} \sin\phi\, \boldsymbol{n}_{\perp}$ and one which is parallel to it $B_{\mathrm{R},\parallel}\boldsymbol{n}_L = B_{\mathrm{R}} \cos\phi\, \boldsymbol{n}_L$. The second point which we can deduce from the equations of motion is the one of the overall current suppression of the spin valve itself. When the effective magnetic field is ignored and at large biases where the Fermi-functions are either 0 or 1, we get for the current [39]:

$$I = \frac{e\Gamma_{\mathrm{L}}^0}{4\hbar}\left(1 - P_{\mathrm{L}}^2 \sin^2\frac{\phi}{2}\right). \tag{5.8}$$

Now, we want to turn our attention to a precise description of the actual transport data of Figure 5.2. One can observe a spin resonance line in the current landscape but even better in the stability diagram of differential conductance. In all the shown plots, we have

an asymmetry ($\Gamma_L^0/\Gamma_R^0 \neq 1$) in the coupling to the leads. Without this condition, we would observe the resonance line at zero bias voltage according to Eq. (5.7). The plot of the fourth order differential conductance (see Figure 5.2 a)) matches perfectly in shape and magnitude the one from Figure 2 of [35]. Together with various line cuts which also agree with their data (e.g. Figure 9 of [35]), we have a strong indication that our fourth order code is producing trustworthy results. This spin resonance effect already appears in second order calculations as it is anticipated from the second order resonance condition (see Figure 5.2 b)). Comparing the scale of the differential conductance in fourth and second order, we can see that the resonance line in the second order is stronger than in the fourth order plot. Generally, there are two competing influences of including fourth order processes.

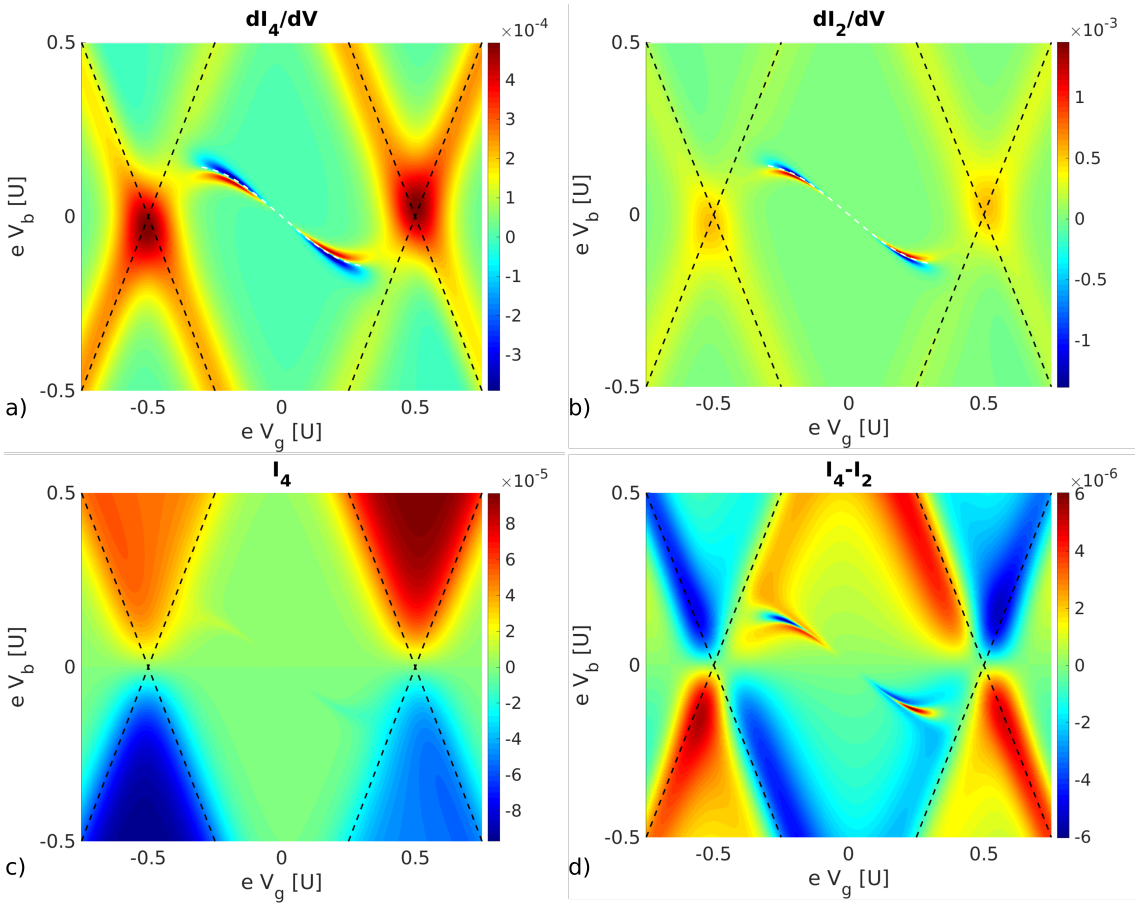


**Figure 5.2 | Transport data of a single dot spin resonance in the spin valve configuration: a)** Differential conductance obtained by fourth order calculations: The transition lines are highlighted by the black dashed lines. The s-shape of the spin resonance line is centred around the particle-hole symmetric point. With white dashed lines the predicted resonance position is marked. **b)** Differential conductance obtained by second order calculations: In comparison with a) the spin resonance line is more pronounced. **c)** Current obtained by fourth order calculations. **d)** Difference of fourth order and second order current highlights the increased current through cotunnelling events inside the Coulomb blockade region. Furthermore, suppression of the resonance line through increased spin decay can be extracted. The parameters of all plots are measured in terms of the Coulomb interaction $U = 1$: $T = 0.05$, $E_z = 0$, $W = 10^{50}$, $\phi = 0.99\,\pi$, $P_l = 0.99$ and $2\Gamma_L^0 = \Gamma_R^0 = 0.01$.

On the one hand, there are more tunnelling events available so that - especially in the Coulomb blockade region - a higher maximal current can be achieved. In Figure 5.2 d) which displays the difference between the fourth and second order current, we observe exactly this (red respective blue region inside the Coulomb blockade region for positive respective negative bias). Though, the regions of current which are enclosed by the black dashed transition lines are exhibiting a lowering of the current. With including fourth order tunnelling events, additional transitions to states are possible which differ by two in terms of particle number and not only the ones with neighbouring particle numbers. On the other hand, a fourth order treatment increases also the spin decay and thus hinders coherent precession of the spin $\boldsymbol{S}$. In this regime, there are more tunnelling events to leave this coherent state at disposal. Due to this decay, the spin resonance line is suppressed close to the transition lines where also sequential tunnelling via thermal excitation can contribute to the current. Well inside the Coulomb blockade region, the current is increased. According to Eq. (5.7), we can predict the position of the spin resonance line through a second order analysis (compare white dashed lines in Figure 5.2 a) and b)).

## 5.2. Double quantum dot spin resonance

In this section, we will now focus on a double quantum dot setup (see Figure 5.3) in the spin valve configuration in analogy to the previous example of a single quantum dot. The two dots are coupled to both leads, have an on-site Coulomb interaction $U$ and a crucial inter-site Coulomb interaction $V$ which will be chosen throughout our analysis to be smaller than $U$. The Hamiltonian of the isolated system $\hat{H}_0$ reads then:

$$\hat{H}_0 = \sum_{\alpha\zeta}\left(\varepsilon_0 - \frac{U}{2} - V\right)\hat{d}^\dagger_{\alpha\zeta}\,\hat{d}_{\alpha\zeta} + U\sum_{\alpha}\hat{d}^\dagger_{\alpha\uparrow}\,\hat{d}_{\alpha\uparrow}\,\hat{d}^\dagger_{\alpha\downarrow}\,\hat{d}_{\alpha\downarrow} + V\left(\hat{d}^\dagger_{d1\uparrow} + \hat{d}_{d1\downarrow}\right)\left(\hat{d}^\dagger_{d2\uparrow} + \hat{d}_{d2\downarrow}\right) \tag{5.9}$$

with $\alpha = \{d1, d2\}$ as the index to specify the dot and $\zeta = \{\uparrow, \downarrow\}$ as the index to specify the spin. In order to see resonance lines in this setup, one needs once again asymmetric coupling to the leads. We have to deal now with a system which has in principle an orbital and a spin degree of freedom. To account for this, we model the tunnelling rate matrix as a Kronecker product between an orbital part and a spin part:

$$\Gamma^p_{l,nm} = \left[\Gamma^{\text{spin}}_l \otimes \Gamma^{\text{orb}}_l\right]^p_{nm} = \left[\left(\mathbb{1}_2 + P^{\text{spin}}_l \boldsymbol{n}_l{}^{\text{spin}} \cdot \boldsymbol{\sigma}\right) \otimes \begin{pmatrix} \Gamma^{\text{orb}}_{l,d1} & 0 \\ 0 & \Gamma^{\text{orb}}_{l,d2} \end{pmatrix}\right]^p_{nm} \tag{5.10}$$

With this form of $\Gamma^p_{l,nm}$, we can describe spin polarization as well as different coupling to the different orbitals. Furthermore, it implies that we do not allow for coherent coupling to the orbitals (off-diagonal elements of $\Gamma^{\text{orb}}_l$). We will address this particular issue in the outlook of this thesis in chapter 8.

At first, we assume $\Gamma^{\text{orb}}_{\text{L},d1} = \Gamma^{\text{orb}}_{\text{L},d2} \neq \Gamma^{\text{orb}}_{\text{R},d1} = \Gamma^{\text{orb}}_{\text{R},d2}$ which can be seen as an equal coupling to both orbitals of each respective lead but with different strength depending on the $l$-index. For such a double dot, we could find the equations of motion which are depicted in Appendix D. The 16 eigenstates of this system can be found in Table D.1. The interesting part about this double dot system is the splitting of the six states with particle number two. We will find two excited states where two electrons occupy either dot one (subscript "$d1$")

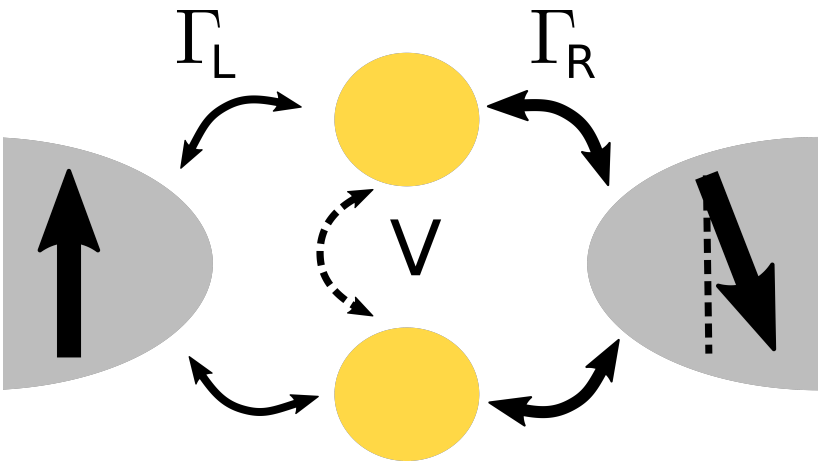


**Figure 5.3 | General setup of a double quantum dot in the spin valve configuration:** The two black arrows indicate the polarization unit vectors $\boldsymbol{n}_{\mathrm{L/R}}$ of the two leads which are again almost antiparallel aligned (compare Figure 5.1). If one wants to fill up one dot with two electrons, one has to pay energy of the on-site Coulomb repulsion $U$. Additionally, there is an inter-site Coulomb repulsion $V$ between the dots. The coupling to the dots can be asymmetric which is denoted by the different thickness of the tunnelling arrows.

or dot two (subscript "$d2$"). The remaining four ground states are divided into a triplet and a singlet. Interestingly, to describe precisely the spin of this triplet state the concept of quadrupole moments is entering (compare Appendix D). The quadrupole moments are able to express an anisotropy of the spin of the triplet. With the help of the equations of motion, we are able to predict the position of the resonance lines (white dashed lines in Figure 5.4). In the plots, we always see from right to left the one-particle, the two-particle and the three-particle Coulomb diamond. We focus now on the one-particle diamond. Here the spins $\boldsymbol{S}_{1d1}$ and $\boldsymbol{S}_{1d2}$ have to be considered which are defined by the expectation values of the respective operators in close analogy to Eq. (5.4). From their equations of motion (see Eq. (D.3c)), we can extract a magnetic field which is exerting a torque on $\boldsymbol{S}_{1\alpha}$ which is defined as

$$\boldsymbol{B}_{1\alpha} = \sum_l 2P_l\Gamma^{\mathrm{orb}}_{l,\alpha}\,\mathrm{Im}\left(Y^+_+(\mu_{10}-\mu_l) - Y^+_+(\mu_{2e1}-\mu_l)\right)\boldsymbol{n}_l,\quad \alpha=\{d1,d2\}\,. \tag{5.11}$$

The difference in respect with the effective magnetic field of the single dot spin resonance (compare Eq. (5.6)) is that here the excited energy difference $\mu_{2e1}$ is entering. It causes that the resonance line will extend to higher bias voltages (see Figure 5.4 b)). According to the resonance condition of maximum precession (see Eq. (5.7)), we are once again able to predict the position of this resonance line. Due to the particle-hole symmetry of this setup, we can apply the same analysis to the three-particle diamond. In the two-particle diamond, however, the effective magnetic field which will precess the spin of the triplet $\boldsymbol{S}_{2gT}$ is determined by Eq. (D.3g):

$$\boldsymbol{B}_{2gT} = \sum_l 2P_l\Gamma^{\mathrm{orb}}_{l,d1}\,\mathrm{Im}\left(Y^+_+(\mu_{2g1}-\mu_l) - Y^+_+(\mu_{32g}-\mu_l)\right)\boldsymbol{n}_l. \tag{5.12}$$

Here the energy difference is with respect to the two-particle ground state.

A deviation of the previous plots is achieved when we are dealing with an additional

asymmetric orbital coupling within the $l$-tunnelling matrix itself. With $\Gamma^{\mathrm{orb}}_{\mathrm{L},d1} = 0.005$, $\Gamma^{\mathrm{orb}}_{\mathrm{L},d2} = \Gamma^{\mathrm{orb}}_{\mathrm{R},d1} = 0.01$ and $\Gamma^{\mathrm{orb}}_{\mathrm{R},d2} = 0.0075$, we observe then a splitting of the resonance lines (see Figure 5.4 c) and d)). The singlet and triplet basis is not ideal to describe the spin resonance effect for such a coupling. Our found equations of motion are not able to capture this observation. If we are just interested in the spin resonance effect in a double quantum dot, it is actually more accurate as well as more straightforward way to think about a double quantum dot as two parallel quantum single dots in parallel. The term which is connecting the two systems is the inter-site Coulomb energy $V$ but it does not distinguish the spin of the involved electrons just its population. Using this ansatz of two independent single dots in respect with their effective magnetic fields allows us - with the help of the resonance condition (compare Eq. (5.7)) - to precisely predict the position of the resonance lines for each orbital separately. The blocking state in the one-particle diamond is now $|\uparrow, 0\rangle$ respective $|0, \uparrow\rangle$ and it can be left through fluctuations to the $|0, 0\rangle$ and the $|2, 0\rangle$ respective $|0, 2\rangle$ state. It is important to note that the coupling to the orbital degree of freedom is diagonal so that there cannot be fluctuations to a different orbital. From this analysis, we get an effective magnetic field $\boldsymbol{B}_{1\alpha}$ which coincides with Eq. (5.11). The blocking state in the two-particle diamond is $|\uparrow, \uparrow\rangle$ and it can be left through fluctuations to the neighbouring particle numbers but this time starting from $|\uparrow, \uparrow\rangle$ which is associated with the ground state energy. The formerly defined $\boldsymbol{B}_{2gT}$ splits then up into $\boldsymbol{B}_{2\alpha}$ using the just described more suitable picture:

$$\boldsymbol{B}_{2\alpha} = \sum_l 2P_l \Gamma^{\mathrm{orb}}_{l,\alpha} \,\mathrm{Im}\left(Y^+_+(\mu_{2g1} - \mu_l) - Y^+_+(\mu_{32g} - \mu_l)\right) \boldsymbol{n}_l, \quad \alpha = \{d1, d2\}\,. \tag{5.13}$$

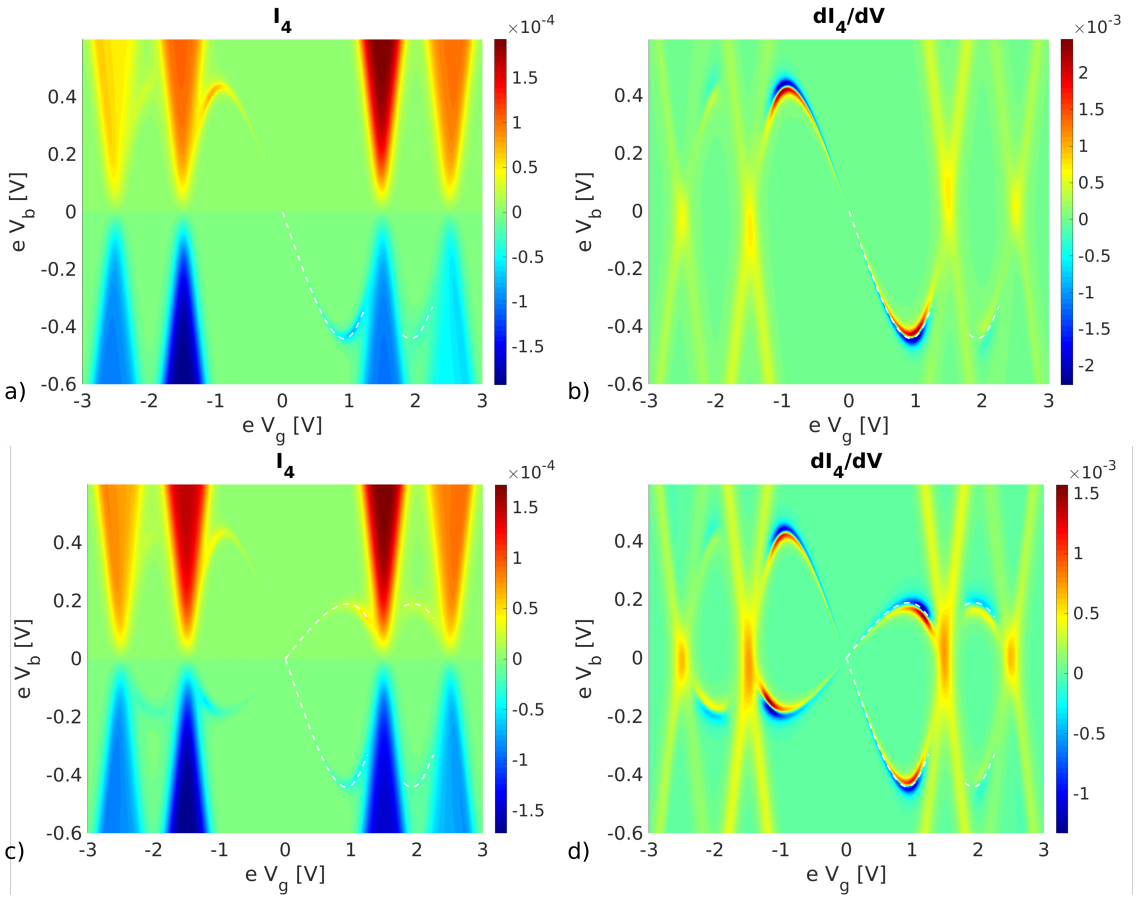


**Figure 5.4 | Transport data of a double dot spin resonance in the spin valve configuration: a)** Current obtained by fourth order calculations for a coupling $\Gamma^{\mathrm{orb}}_{\mathrm{L},d1} = \Gamma^{\mathrm{orb}}_{\mathrm{L},d2} = 0.005$ and $\Gamma^{\mathrm{orb}}_{\mathrm{R},d1} = \Gamma^{\mathrm{orb}}_{\mathrm{R},d2} = 0.01$. **b)** Differential conductance obtained by fourth order calculations: The resonance line in the $N = 2$ Coulomb diamond is very pronounced compared to the outer resonance lines in the $N = 1$ and $N = 3$ Coulomb diamonds. The coupling is the same as in a). **c)** Current obtained by fourth order calculations for a coupling $\Gamma^{\mathrm{orb}}_{\mathrm{L},d1} = 0.005$, $\Gamma^{\mathrm{orb}}_{\mathrm{L},d2} = \Gamma^{\mathrm{orb}}_{\mathrm{R},d1} = 0.01$ and $\Gamma^{\mathrm{orb}}_{\mathrm{R},d2} = 0.0075$. **d)** Differential conductance obtained by fourth order calculations (same coupling as c)): Due to the asymmetric coupling, the three resonance lines in the respective diamonds split up. In all the plots, the predicted resonance positions for positive gate voltages are marked with white dashed lines. The parameters of all plots are measured in terms of the Coulomb interaction $V = 1$: $U = 3$, $T = 0.05$, $E_{\mathrm{z}} = 0$, $W = 10^{50}$, $\phi = 0.99\,\pi$ and $P_l = 0.99$.

# 6

# Canyon of conductance

In the introduction, we asked ourselves if in the cotunnelling transport regime the so-called canyon of conductance will protrude into the Coulomb blockade region. We will explain in this chapter the specifications of both the experimental [22] and the theoretical setup [24] in which such suppression of current and therefore conductance can be observed. Moreover, we will show our transport calculations which will proof that cotunnelling current is extending the canyon of conductance into the Coulomb blockade region.

In an InSb nanowire quantum dot (see Figure 1.5 (i) (a)), there exist multiple energy levels which have a large level dependent $g$-factor. If one applies now a magnetic field to this system, it is possible to shift these energy levels so that two of them get degenerate (compare Figure 1.5 (i) (c)). At low temperatures (here 300mK) exactly at those points, one sees the conductance dropping. This prerequisite of degenerate energies is fulfilled on a line in a gate voltage versus magnetic field plot (compare Figure 1.5 (i) (b) or Figure 6.1 a)). It should be noted that in this setup a constant bias voltage is provided to enable current. The cause of this canyon is an interplay of interference and correlations of the involved electrons due to Coulomb interaction. These plots in a gate voltage-magnetic field-landscape have, similar to stability diagrams, regions where the system is in a state of Coulomb blockade. There one exhibits suppression of current in respect to regions where current can easily flow. In this case, the canyon is stretching from the $N = 6$ Coulomb blockade region with spin $S_z = 0$ to the one of $N = 8$ with spin $S_z = 1$. Nevertheless, tunnelling events like the ones of cotunnelling or higher order ones can provide means to have current in the Coulomb blockade region $N = 7$ with $S_z = \frac{1}{2}$ where the canyon is cutting through. Though due to interference, even those tunnelling processes cannot drive a current in special parameter sets like the ones of precisely the canyon of conductance.

We turn now the attention to the theoretical explanation and especially to the numerical calculations of the canyon of conductance which were done in [22] but to a greater extent in a following up publication [24]. At first, we notice that in the experimental (compare Figure 1.5 (ii) (b)-(f)) as well in the numerical data (compare e.g. Figure 4 of [22]) the canyon of conductance is always accompanied by a correlation-induced resonance near the electron-hole symmetric point which was predicted at first in [40]. This correlation-induced resonance depends exponentially on the Coulomb repulsion $U$ [40]. For numerical calculations of the conductance, they use in both cited theoretical works the second order von Neumann (2vN) approach [23] and apply it on a two-level, spinless, interacting model. As already pointed out in the introduction, this approach is numerically very expensive because it is, among others, non-perturbative. It is therefore not easily applicable to bigger systems. Besides, it should be noted that the 2vN approach is only reliable in a temperature

regime where the temperature is higher than the Kondo temperature [23] so that they had to give a slightly higher temperature as in the experiment. Due to the 2vN approach, it is not clear if this conductance suppression only appears when taking into account higher order processes.

With our self-implemented transport code, we have now the ability to check if also the cotunnelling regime exhibits this canyon of conductance. With our fourth order diagrammatic approach, there are some advantages as well as disadvantages with respect to the 2vN approach. Obviously, our approach is perturbative and therefore definitely more suitable for problems with lower coupling strengths. On the other side, the cotunnelling contribution is - at least in the weak coupling limit - the strongest contribution and higher order processes are just small corrections to it. In contrast to the sequential tunnelling regime, it provides though conceptionally different tunnelling processes which due to quantum fluctuations allow for transport in the Coulomb blockade regime. With one-electron and two-electron processes together, we would capture the leading order of all possible processes. Furthermore, we have a clean construction of our fourth order theory where we do not neglect any contributions so far. In contrast to this, the 2vN approach can exhibit negative conductivities due to an improper treatment of higher order processes [22].

For our calculations, we assume the same tunnelling rate matrices as in [24]:

$$\Gamma_{\mathrm{L}}^{\mathrm{canyon}} = \Gamma^{\mathrm{canyon,0}} \begin{pmatrix} 1 & a \\ a & a^2 \end{pmatrix}, \Gamma_{\mathrm{R}}^{\mathrm{canyon}} = \Gamma^{\mathrm{canyon,0}} \begin{pmatrix} 1 & -a \\ -a & a^2 \end{pmatrix}, a \in \mathbb{R} \tag{6.1}$$

With such a coupling the two dot states couple with opposite parity to the leads. If one thinks about coupling as an overlap of the dot wave function with the lead wave functions, we could think about one dot state with a symmetric wave function and one with an antisymmetric one. In Figure 6.1, our numerical findings are displayed. There is a strong indication that every order will - due to interference - cancel itself within this correlation-induced resonance peak and result in a canyon of conductance. The argument for the existence of such a canyon inside the Coulomb blockade region is therefore not based on a summation of all orders.

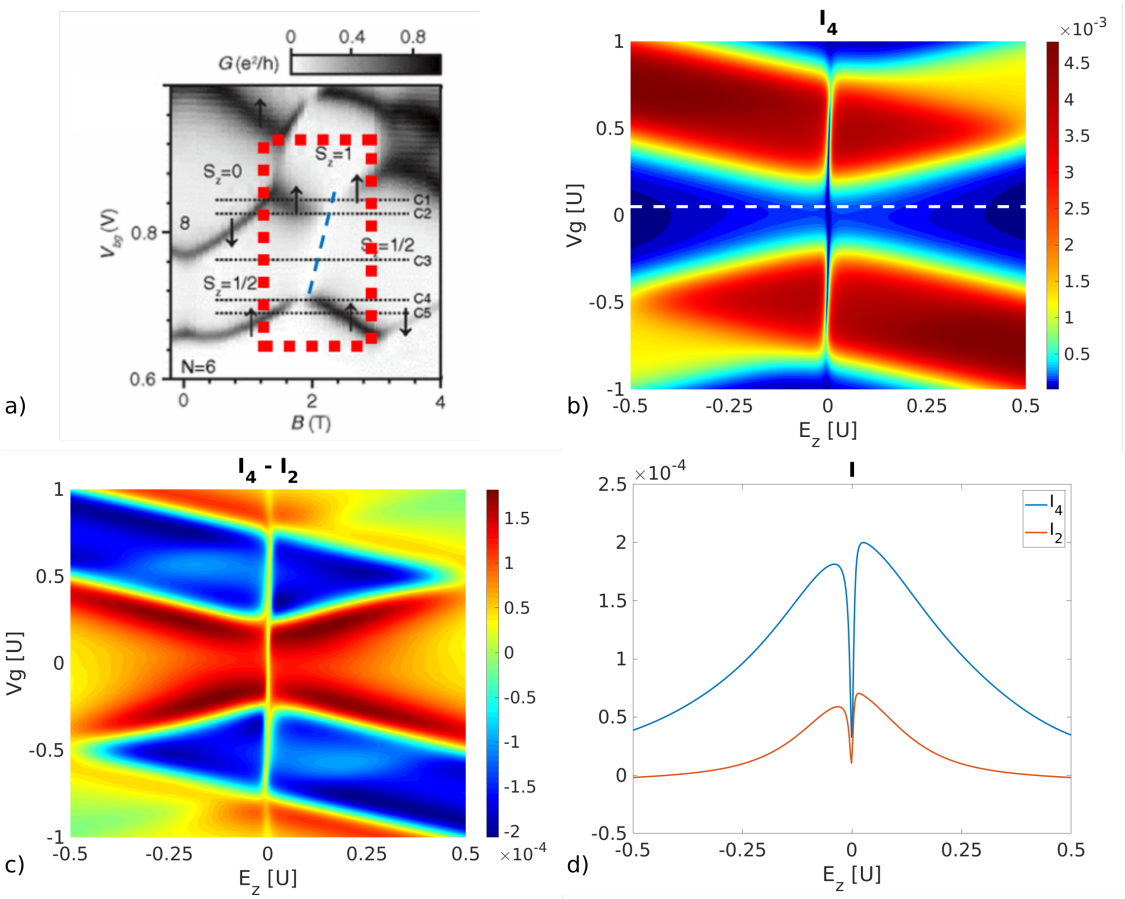


**Figure 6.1 | Canyon of conductance of a single quantum dot in a $E_z$-$V_g$ plot: a)** Experimental data of the conductance of an InSb quantum dot where one observes a canyon of conductance (blue dashed line). The red dashed box should schematically show the area which we model in our calculations. Picture is taken from Figure 2 of [22]. **b)** Increasing a magnetic field $B$ is proportional to increasing the Zeeman splitting $E_z$ of the two dot states. In this plot, the fourth order current is shown in a $E_z$-$V_g$-landscape. Close to $E_z = 0$, a canyon of conductance is cutting through the plot. The asymmetry parameter is chosen to be $a = 0.5$. All other parameters are chosen with respect to $U = 1$: $V_b = 0.5$, $T = 0.05$, $\Gamma^{\text{canyon},0} = 0.01$ and $W = 10^{50}$. **c)** The difference of fourth and second order current is depicted. Due to fourth order processes, more current inside the Coulomb blockade is observed. The parameters are the same as in b). **d)** The two line cuts along the white dashed line of plot b) ($V_g = 0.05$) of fourth (blue) and second (red) current highlight the appearance of a canyon of conductance. The fact that the canyon does not cut through the Coulomb blockade regime as a vertical line can be seen by the asymmetric peaks which accompany the canyon. The reason why the fourth and second order current does not drop exactly to zero inside the canyon is due to a slightly incomplete destructive interference. A complete destructive interference is just obtained for one specific line in a gate voltage versus bias voltage, which would translate here to one specific gate voltage per fixed bias voltage (compare [18]).

# 7

# Unifying picture for interference

In this chapter, we want to give a unifying picture for interference. In chapter 5, we investigated spin resonances where, due to coherent precession of the spin, we could see an increase in the current. In chapter 6, we dealt with the so-called canyon of conductance where the conductance is suppressed by interference. In the introduction, we mentioned interference blockade in a carbon nanotube quantum dot where once again suppression of conductance in certain transitions lines is observed. Now, we will address the connection of all these setups which was one of the questions, we raised in the introduction.

The way how we constructed our transport code allows us now to easily switch between the setups which look at the first glance quite different (e.g. sometimes we have an increase of current and sometimes a decrease). The link to bring these setups nonetheless together are the tunnelling rate matrices. They are the fundamental part to describe interference effects. For a single quantum dot in the spin valve configuration, we define them as

$$\Gamma^{p}_{l,nm} = \left[\Gamma^{0}_{l}\left(\mathbb{1}_2 + P_l \boldsymbol{n}_l \cdot \boldsymbol{\sigma}\right)\right]^{p}_{nm}. \tag{7.1}$$

In Figure 7.1, we show the transition of the interference blockade picture to the spin resonance one. If the polarized leads have an intermediate opening angle of roughly $0.2\,\pi < \phi < 0.8\,\pi$, we observe the disappearance of transition lines along with negative differential conductance which both are fingerprints for interference blockade (compare Figure 7.1 a)). The origin of negative differential conductance is the existence of a blocking state which is characterized by non-coupling to one of the leads [21]. The remaining transition to the other lead is, due to the bias voltage, energetically not favourable so that both transition lines are suppressed. If we increase the opening angle between the polarized leads further ($\phi > 0.9\,\pi$), then we enter into the realm of the spin valve configuration and thus of the spin resonance lines (compare Figure 7.1 b) and c)). Spin resonance is therefore just at the very end of this increase of the opening angle. It is important to note that if we reach an angle of exactly antiparallel alignment ($\phi = \pi$, compare Figure 7.1 d)) spin resonance disappears which seems counterintuitive at first sight. Though as we have pointed out already, we need the coherences of the involved density matrix to play a role which will induce the all-important effective magnetic field. If we can diagonalize the two tunnelling rate matrices at the same time which is the case in antiparallel alignment, the role of the coherences will vanish and hence the effective magnetic field. The maximum of spin resonance is therefore not - as one could suspect - close to $\phi = 0.99\,\pi$ but closer to $\phi = 0.95\,\pi$ (compare Figure 7.1 b) and c)). In the canyon of conductance setup, we deal with a tunnelling rate matrix of the following form

$$\Gamma^{\text{canyon}}_{l} = \Gamma^{\text{canyon},0} \begin{pmatrix} 1 & (-1)^l a \\ (-1)^l a & a^2 \end{pmatrix}, \quad l = \{0, 1\} \tag{7.2}$$

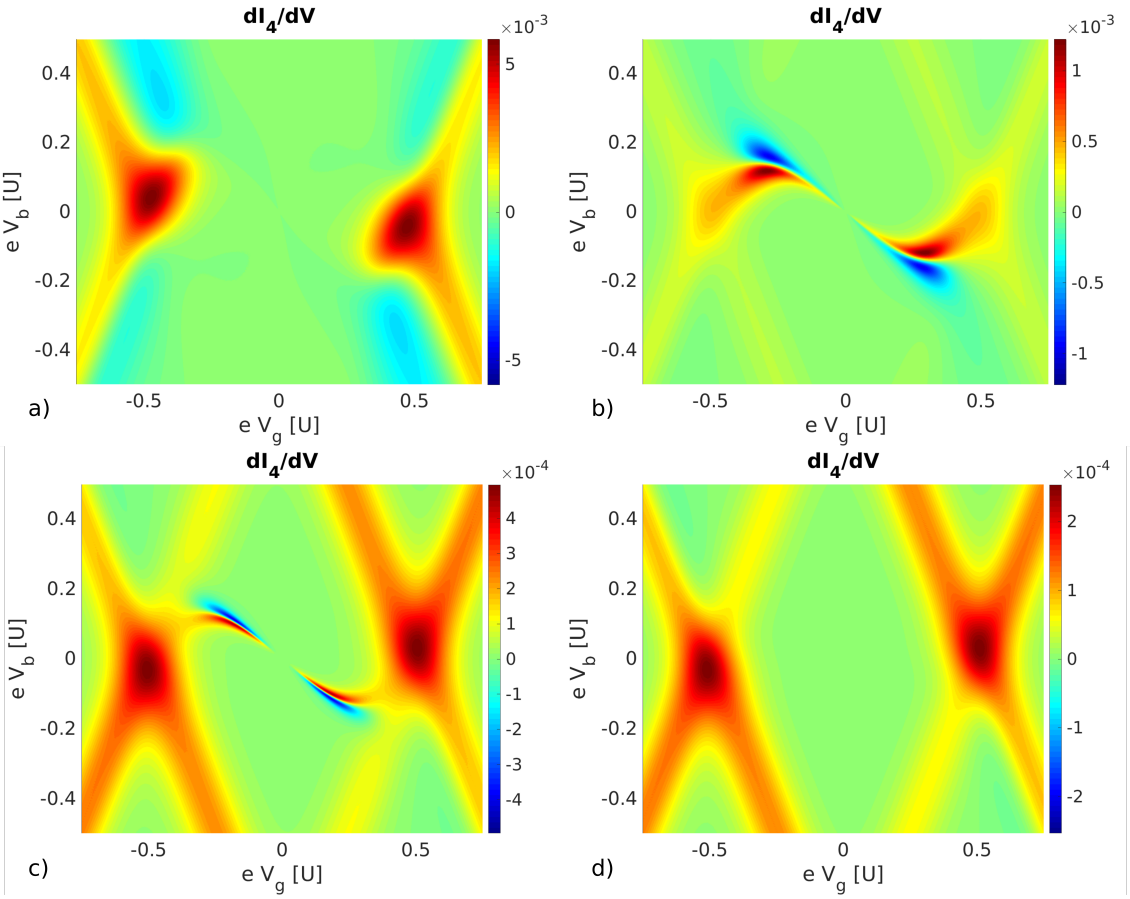


**Figure 7.1 | Transformation of the interference blockade picture to the spin resonance picture:** All parameters of the following differential conductance plots of this figure are measured in terms of the Coulomb interaction $U = 1$: $T = 0.05$, $E_z = 0$, $W = 10^{50}$, $P_l = 0.99$, $2\Gamma^0_L = \Gamma^0_R = 0.01$ and **a)** $\phi = 0.7\,\pi$, **b)** $\phi = 0.95\,\pi$, **c)** $\phi = 0.99\,\pi$, **d)** $\phi = \pi$.

where the $l$-index changes the sign of the asymmetry parameter $a$ so that L$\rightarrow 0$ and R$\rightarrow 1$. We are now able to find the parameters $P_l$ and $\boldsymbol{n}_l$ to reexpress the tunnelling rate matrix of the canyon of conductance setup into the one of spin polarized leads (Eq. (7.1)):

$$\Gamma^0_l = \Gamma^{\text{canyon},0}\left(1+a^2\right), \boldsymbol{n}_l = \begin{pmatrix} (-1)^l \sin\phi \\ 0 \\ \cos\phi \end{pmatrix}, \phi = \sin^{-1}\left(\frac{2a}{1+a^2}\right), P_l = 1. \tag{7.3}$$

In the polarization vector, the factor $(-1)^l$ should be understood as 1 for L and as -1 for R. With $a = 0.5$, we have a polarization opening angle of $\phi \approx 0.59\,\pi$ so that we are exactly in the picture of interference blockade with decoupled states. In Figure 7.2, we highlight graphically the link between interference blockade in the $V_g$-$V_b$-landscape and canyon of conductance in the $E_z$-$V_g$. With the help of this connection, the interpretation of this origin of the canyon of conductance is now more evident. Due to degenerate states, a decoupling of a certain state from one of the leads can arise which is accompanied by negative differential conductance (compare Figure 7.2 e)). In Figure 7.2 d), a drop of current close to the $N = 1 \leftrightarrow N = 2$ transition can be observed. For the interpretation of the origin of the canyon of the conductance, one could go even further and make the

comparison to optical dark states. The latter ones were firstly studied in 1976 [41, 42]. A three-level system irradiated by a laser exhibits an optical interference effect. If the level splitting of the ground states matches the frequency separation between the laser modes, the fluorescent light emitted by depopulation of an excited state is disappearing [42]. The canyon of conductance is nothing else as an all-electronic analogon of this optical dark state. Such an all-electronic dark state was proposed in [21]. The coherent tunnelling takes on the role of the coherent laser pumping. The different modes of the laser are represented by the different couplings to leads. In Figure 7.3, we display a plot of the excited state occupation in the optical dark state case and one of the current through the dot in the canyon of conductance case. In both cases, we vary the resonance parameter of the splitting of the two ground states. The parameters which are chosen are different but the qualitative agreement is striking. In the work of [21], there is, though, no variation of the energy splitting because there is no magnetic field applied but rather a change in the Lamb shift frequencies of the energy levels. The Lamb shift contributions stem once again from fluctuations of the system to the leads and they are strongly depending on the applied bias and gate voltage. To summarize it, they all are based on the same underlying physics even if there are some subtle differences.

If we apply a magnetic field to all of our models, the direction of magnetic field with respect of the polarization plane of the two leads is of crucial importance. We can, for example, apply an additional magnetic field to the spin resonance picture. The direction vector of the applied magnetic field will directly add to the effective magnetic field in the resonance condition (compare Eq. (5.7)) and hence alter the position of the spin resonance. Though, applying the magnetic field perpendicular to the polarization plane of the leads would not influence the effect of interference because it is equally coupled to both spins. It is clear that the effective magnetic field and thus the spin resonance will always disappear if the Zeeman splitting of the states is big enough so that the coupling can distinguish between the formerly quasi-degenerate states.

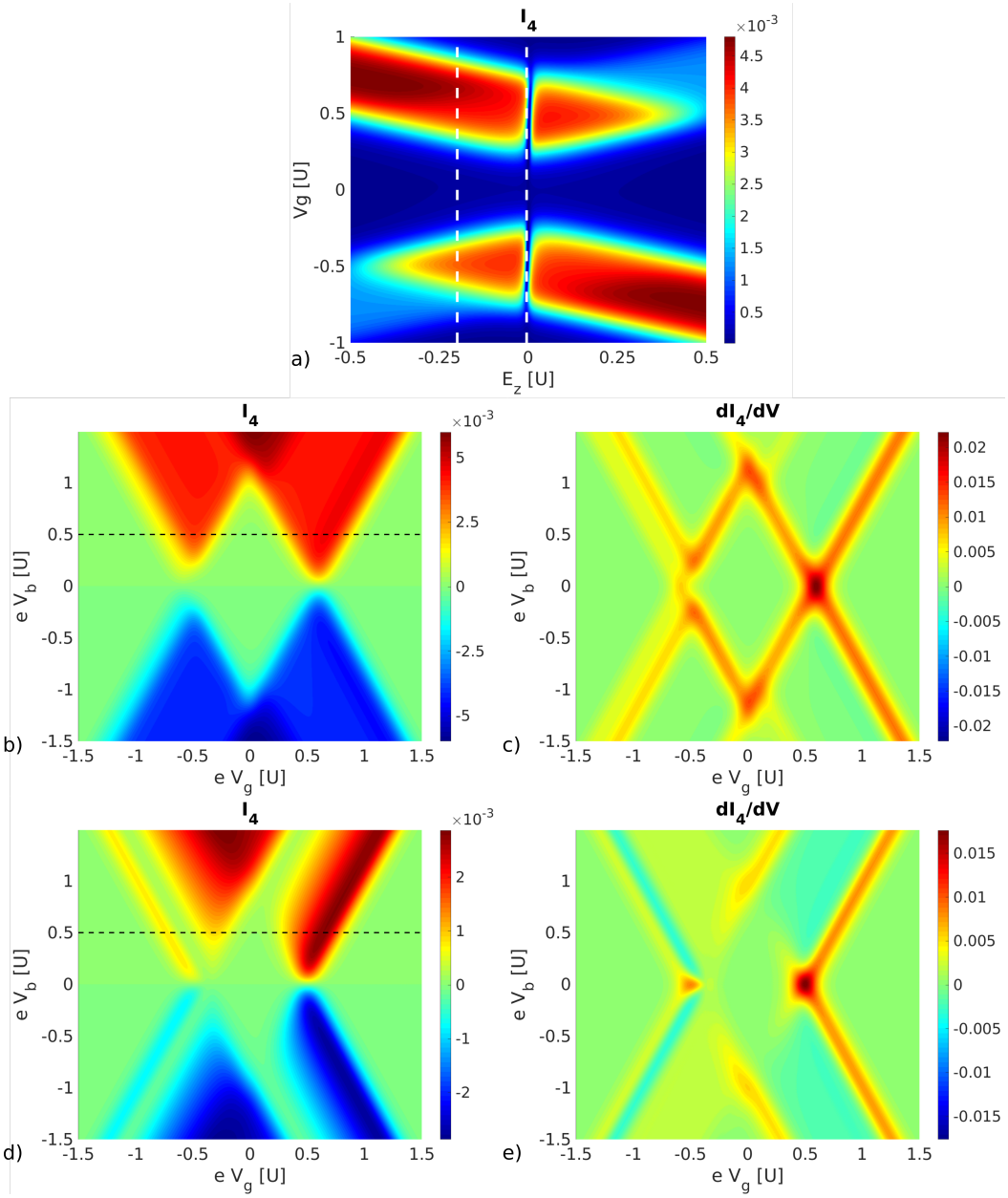


**Figure 7.2 | Transformation of the canyon of conductance picture to the interference blockade picture: a)** Canyon of conductance: The asymmetry parameter is set to $a = 0.5$. All other parameters are chosen with respect to $U = 1$: $V_\mathrm{b} = 0.5$, $T = 0.05$, $\Gamma^{\mathrm{canyon},0} = 0.01$ and $W = 10^{50}$. All other plots which will follow have the same parameters except that the bias voltage is not fixed. The two white dashed lines represent the line cuts ($E_\mathrm{z} = -0.2$ respective $E_\mathrm{z} = -0.005$) which will correspond to the line cuts of b) respective d) (black dashed lines) **b)** Current for $E_\mathrm{z} = -0.2$. **c)** Differential conductance for $E_\mathrm{z} = -0.2$: Far from the canyon of conductance small negative differential conductance appears close to the $N = 0 \leftrightarrow N = 1$ transition. The asymmetric coupling to the leads results in a smaller split-up of the transition lines on the right hand side which will cause then negative differential conductance according to [43]. **d)** Current for $E_\mathrm{z} = -0.005$. **e)** Differential conductance for $E_\mathrm{z} = -0.005$: Inside the canyon of conductance, there is strong suppression of the transition lines $N = 1 \leftrightarrow N = 2$ which indicates that the two-particle state is decoupled from one of the leads.

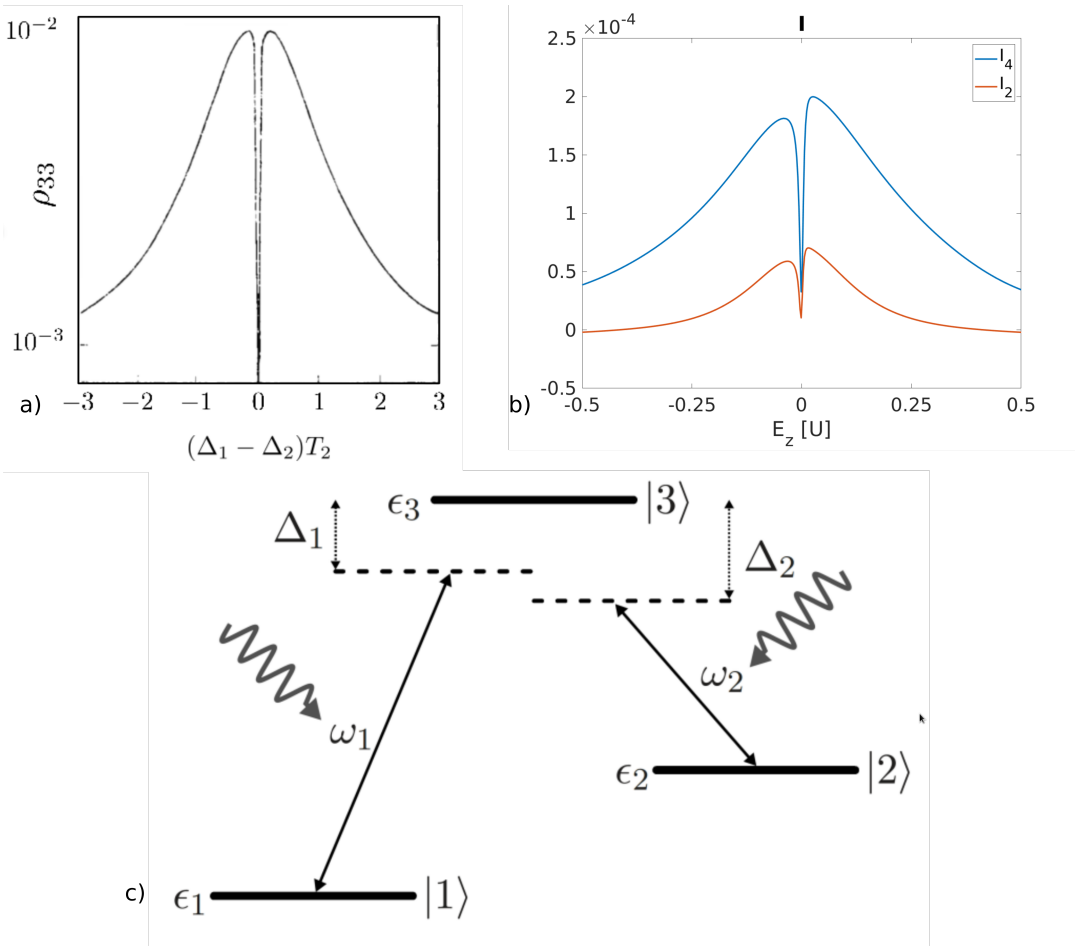


**Figure 7.3 | Comparison of an optical and an all-electric dark state: a)** Excited-state occupation as a function of the resonance parameter. Taken from Figure 1 of [42]. **b)** Same plot as Figure 6.1 d) shows the fourth and second order current with respect to the Zeeman splitting $E_z$. The applied magnetic field is in the plane of the lead polarization which results in an asymmetry of the peaks which accompany the interference canyon. Nevertheless, there is good qualitative agreement with the plot of an optical dark state. **b)** Sketch of a three-level system $(\epsilon_1, \epsilon_2, \epsilon_3)$ on which an optical dark state is based. The curvy lines represent the different laser modes of frequency $\omega_1$ and $\omega_2$. These modes are detuned by $\Delta_1$ respective $\Delta_2$. The dark state forms under the condition $\Delta_1 = \Delta_2$ even if the lasers are slightly tuned away from resonating the excited state.

# 8

# Conclusion and outlook

In this thesis, we addressed the topic of interference effects in tunnelling setups with the focus on the cotunnelling transport regime. There are five main points of this thesis which we want to stress now. One achievement is surely that we managed to find an analytic expression for the cotunnelling energy integrals, namely the $D$- and the $X$-function. We did not restrict ourselves to the real part of the cotunnelling energy integrals which are needed for the dynamics of the populations but rather include also the imaginary part. With this imaginary part, we are now also able to consider the dynamics of the coherences up to fourth order (compare section 4.3). Besides, we embedded these integrals in a concise formalism based on the diagrammatic approach expressed in the Liouville space.

Another important point of this thesis is the implementation of a transport code upon this theory. In section 4.6, we demonstrated the general operating principle of this transport code as well as some numerical objections like e.g. how to treat infinite sums in the cotunnelling energy integrals.

Furthermore, we dedicated section 5.1 to introduce the spin valve configuration and explain the origin of resonance lines which appear in a single quantum dot. Based on this, we could extend this already known mechanism to a double quantum dot which is coupled via inter-site Coulomb interaction. We showed numerical data of the appearing resonance lines and predicted their positions through our analytical findings. For example, we could set up the equations of motion for a double quantum dot with equal orbital coupling (compare Appendix D) out of which we concluded the exact definitions of the involved effective magnetic fields. The latter ones are responsible for lifting the spin valve effect and thus result in a resonance current. In the single and double quantum dot, the cotunnelling processes are necessary to obtain such a resonance line deep inside the Coulomb blockade region.

The next finding of this thesis is the occurrence of a canyon of conductance in the cotunnelling transport regime. In chapter 6, we demonstrated the extension of the canyon of conductance into the Coulomb blockade region. We could conclude that the cotunnelling current exhibits destructive interference within itself similar as in sequential tunnelling. Another available transport code which showed this canyon of conductance at first works with a non-perturbative approach so that they could not make an explicit statement about interference in the cotunnelling transport regime.

Last but not least, we were able to combine three - at first glance - different models, namely interference blockade, spin resonance and canyon of conductance, into a unifying

picture. The link to bring these models together are the tunneling rate matrices. In chapter 7, we could show the transition of the inference blockade picture into the spin resonance picture via a monotonous increase of the opening angle of the spin polarized leads. Even more interesting, the mapping of the canyon of conductance picture into the interference blockade, both analytical and graphical, was displayed. The similarities of these different manifestations of interference effects were, up to now, not greatly emphasized in the literature. Moreover, we could extend the findings of a work about all-electric dark states in a carbon nanotube quantum dot. We could support their claim of encountering an electrical analogon of an optical dark state in their setup. We produced in similar setup a line cut of current which has the characteristic shape of a plot of fluorescence of an optical dark state. With our appropriated knowledge, we can now confidently claim that the canyon of conductance is, in his essence, also an all-electric dark state.

This thesis represents not a closed research work but more an ongoing one. Therefore, one can mention as an outlook of this thesis a couple of things. First of all, the model of a double quantum dot is not yet elaborated to full extent. In section 5.2, we addressed a double quantum dot with spin polarized leads. Though, the orbital coupling of the leads was in both treated cases diagonal. If we allow the orbital part to be off-diagonal, we can assume for the tunnelling rate matrix:

$$\Gamma^p_{l,nm} = \left[\Gamma^0_l \left(\mathbb{1}_2 + P_l^{\text{spin}} \boldsymbol{n}_l^{\text{spin}} \cdot \boldsymbol{\sigma}\right) \otimes \left(\mathbb{1}_2 + P_l^{\text{orb}} \boldsymbol{n}_l^{\text{orb}} \cdot \boldsymbol{\sigma}\right)\right]^p_{nm} \tag{8.1}$$

Preliminary results which are obtained in such a configuration of a spin valve - both in terms of spin and orbit - are displayed in Figure 8.1. Several lines with different slopes inside the outer Coulomb diamonds suggest the existence of an interesting mechanism which is so far not understood. Furthermore, the existing transport code is through its generality ideal to apply it to different transport setups. Another interesting path could be to go to bigger system like e.g. a triple quantum dot which is the smallest system with symmetry protected orbital degeneracies but where we would have to improve the performance of the transport code. Moreover, the transport code is the perfect prelude for a setup with superconducting leads. To work with a particle-conserving approach to superconductivity can be very promising in this respect [44]. Due to the knowledge we gained by calculating the complex cotunnelling energy integrals and especially due to findings of the former group member Jordi Picó Cortés, we find it encouraging to head into this direction.

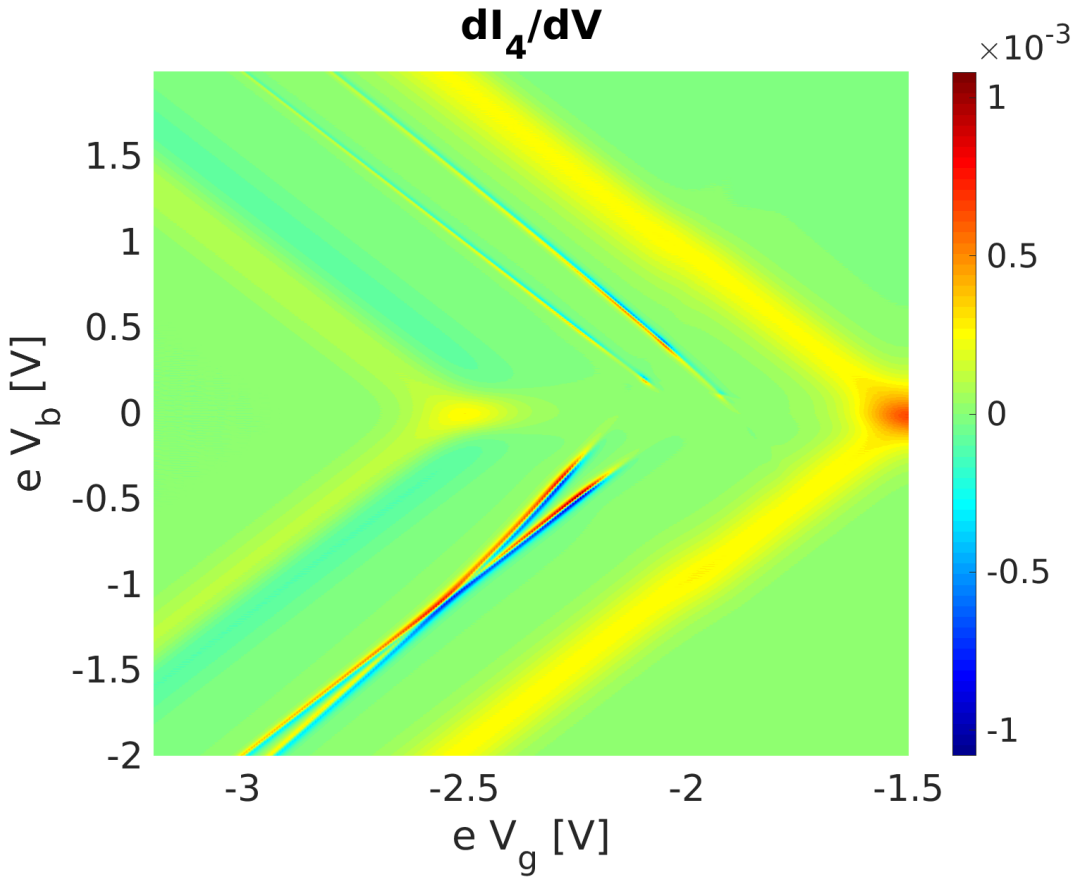


**Figure 8.1 | Differential conductance of a double quantum dot with spin and orbital polarized leads:** Inside the one- and three-particle Coulomb diamond resonance lines appear but the origin of them cannot be explained so far. All parameters are measured in terms of the Coulomb interaction $V = 1$: $T = 0.05$, $U = 3$, $E_z = 0$, $W = 10^{50}$, $P_l^{\mathrm{orb}} = P_l^{\mathrm{spin}} = 0.99$, $\phi^{\mathrm{orb}} = \phi^{\mathrm{spin}} = 0.99\,\pi$ and $2\Gamma_{\mathrm{L}}^0 = \Gamma_{\mathrm{R}}^0 = 0.01$ (according to Eq. (8.1)).

# Part IV.

# Appendix

# A

# Sequential tunnelling energy integral

The following integral defines the $Y$-function up to the prefactor $\left(-\frac{i}{2\pi}\right)$. To perform this integral, we use the residue theorem. It states that an integration on a closed contour in the complex plane is equal to the sum of all residues of the poles which are located inside the contour multiplied by $(2\pi i)$. The contour which is chosen for this integration is depicted in Figure A.1. The contour consists of only the real axis and a big semi-circle which will be zero due to the cut-off function. The integral then yields

$$\begin{aligned}
&\lim_{\eta\to 0}\int \mathrm{d}\omega \frac{f^p(\omega)\,L(W,\omega)}{\omega-\mu+i\eta} = 2\pi i\sum_{k=0}^{\infty}(-p)\,\frac{L(W,i\omega_k)}{i\omega_k-\mu} + 2\pi i\left(-\frac{1}{2}iW\right)\frac{1}{iW-\mu}f^p(+iW)\\
&= 2\pi i\sum_{k=0}^{\infty}(-p)\,iL(W,\mu)\left[\frac{1}{2}\left(\frac{1-\frac{i\mu}{W}}{\omega_k-W}+\frac{1+\frac{i\mu}{W}}{\omega_k+W}\right)-\frac{1}{\omega_k+i\mu}\right]\\
&+ 2\pi i\left(-\frac{1}{2}iW\right)\frac{1}{2}\left(1-ip\tan\left(\frac{W}{2}\right)\right)\frac{1}{iW-\mu}\\
&= \pi pL(W,\mu)\left[\frac{1}{\pi}\left(\Psi^{(0)}\left(\frac{1}{2}+\frac{i\mu}{2\pi}\right)-C'\right)-\frac{1}{2\pi}\left(1-\frac{i\mu}{W}\right)\left(\Psi^{(0)}\left(\frac{1}{2}-\frac{W}{2\pi}\right)-C'\right)\right.\\
&\left.-\frac{1}{2\pi}\left(1+\frac{i\mu}{W}\right)\left(\Psi^{(0)}\left(\frac{1}{2}+\frac{W}{2\pi}\right)-C'\right)\right]+\frac{\pi}{2}\frac{W}{iW-\mu}\left(1-ip\tan\left(\frac{W}{2}\right)\right)\\
&= pL(W,\mu)\left[-\left(\frac{1}{2}-\frac{i\mu}{2W}\right)\Psi^{(0)}\left(\frac{1}{2}-\frac{W}{2\pi}\right)-\left(\frac{1}{2}+\frac{i\mu}{2W}\right)\Psi^{(0)}\left(\frac{1}{2}+\frac{W}{2\pi}\right)\right.\\
&\left.\Psi^{(0)}\left(\frac{1}{2}+\frac{i\mu}{2\pi}\right)\right]+\frac{1}{2}L(W,\mu)\left(\frac{\mu}{W}-i\right)\left[\pi-ip\left(\Psi^{(0)}\left(\frac{1}{2}+\frac{W}{2\pi}\right)-\Psi^{(0)}\left(\frac{1}{2}-\frac{W}{2\pi}\right)\right)\right]\\
&\overset{W\to\infty}{=} -\frac{i\pi}{2}+p\left[\Psi^{(0)}\left(\frac{1}{2}+\frac{i\mu}{2\pi}\right)-\Psi^{(0)}\left(\frac{1}{2}+\frac{W}{2\pi}\right)\right] \qquad \text{(A.1)}
\end{aligned}$$

The constant $C'$ is defined by Eq. (4.29) but will drop anyway. For the second line, we used the following relations

$$\frac{L(W,i\omega_k)}{i\omega_k-\mu} = iL(W,\mu)\left[\frac{1}{2}\left(\frac{1-\frac{i\mu}{W}}{\omega_k-W}+\frac{1+\frac{i\mu}{W}}{\omega_k+W}\right)-\frac{1}{\omega_k+i\mu}\right], \qquad \text{(A.2)}$$

$$f^p(+iW) = 1-ip\tan\left(\frac{W}{2}\right), \qquad \text{(A.3)}$$

and we expressed in the third last line the tangent in terms of two digamma functions:

$$\pi\tan(\pi x) = \Psi^{(0)}\left(\frac{1}{2}+x\right)-\Psi^{(0)}\left(\frac{1}{2}-x\right). \qquad \text{(A.4)}$$

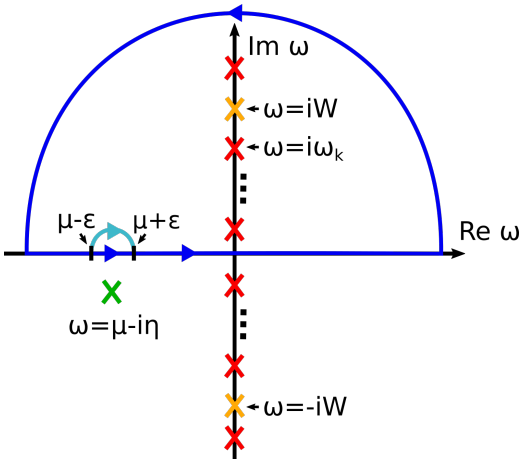


**Figure A.1 | Contour integral of Eq. (A.5) in the complex plane:** The dark blue line depicts the integration path and the crosses are representing the poles of the Fermi-function (red), the pole of the denominator (green) and the poles of the cut-off function $L(W,\omega)$ (orange). With this chosen contour only the poles of the Fermi-function, which lay on the positive imaginary axis, and one pole of the cut-off function, which lays at $\omega = iW$ with residuum $-\frac{1}{2}iW$, have to be taken into account. The Fermi-poles on the upper half plane are located at $\omega_k = 2\pi\left(k+\frac{1}{2}\right)$ for $k \in \mathbb{N}$ with residuum $-p$. The light blue semi-circle is the contour which is taken for the last term of Eq. (A.7) while the second last term of this equation is the same semi-circle which is closed in on the real axis.

Moreover, we defined the constant $C$ by the renormalized wide band constant $W$ as $C = \Psi^{(0)}\left(\frac{1}{2}+\frac{W}{2\pi}\right)$. In the dissertation of S. Koller [5], the same result is obtained by splitting up the contour into a principle value integration which is denoted by $\int' \mathrm{d}\omega$ and an integration of the small area around $\omega = \mu$ which can be solved by the use of the light blue semi-circle which is shown in Figure A.1.

$$\lim_{\eta\to 0}\int_{-\infty}^{\infty}\mathrm{d}\omega\frac{f^p(\omega)\,L(W,\omega)}{\omega-\mu+i\eta} = \tag{A.5}$$

$$= \lim_{\eta\to 0}\lim_{\varepsilon\to 0}\left(\int_{-\infty}^{\mu-\varepsilon}\mathrm{d}\omega\frac{f^p(\omega)\,L(W,\omega)}{\omega-\mu+i\eta} + \int_{\mu+\varepsilon}^{\infty}\mathrm{d}\omega\frac{f^p(\omega)\,L(W,\omega)}{\omega-\mu+i\eta} + \int_{\mu-\varepsilon}^{\mu+\varepsilon}\mathrm{d}\omega\frac{f^p(\omega)\,L(W,\omega)}{\omega-\mu+i\eta}\right) \tag{A.6}$$

$$= \lim_{\eta\to 0}\int'\mathrm{d}\omega\frac{f^p(\omega)\,L(W,\omega)}{\omega-\mu+i\eta}$$

$$- \lim_{\eta\to 0}\lim_{\varepsilon\to 0}\left(\oint_{\frown}\underbrace{\mathrm{d}\omega\frac{f^p(\omega)\,L(W,\omega)}{\omega-\mu+i\eta}}_{=0} - \oint_{\frown}\underbrace{\mathrm{d}\omega\frac{f^p(\omega)\,L(W,\omega)}{\omega-\mu+i\eta}}_{=-i\pi f^p(\mu)}\right) \tag{A.7}$$

$$= \int'\mathrm{d}\omega\frac{f^p(\omega)\,L(W,\omega)}{\omega-\mu} - i\pi f^p(\mu) \tag{A.8}$$

This split-up coincides exactly with the Sokhotski–Plemelj theorem which states for the

real line

$$\lim_{\eta\to 0}\int_{-\infty}^{\infty} \mathrm{d}x \frac{f(x)}{x-y+i\eta} = \int' \mathrm{d}x \frac{f(x)}{x-y} - i\pi f(y) \tag{A.9}$$

with $f(x)$ is an arbitrary complex-valued function which has no poles on the real line. The purpose of showing that the result of this integral can also obtained without splitting the integrand into real and imaginary is that we have a justification using this residuum-only method. It should be mentioned that, in this method, we exchange the order of the limit $\eta \to 0$ and the integration. In general, this is not allowed but if we have a function which is analytic and the integral exists, it is reasonable to exchange them.

# B

# Vanishing of the $C$-constant in sequential tunnelling

In the following, we proof that the part of the $Y$-function which does not depend on the $\mathcal{L}_\mathrm{S}$ is vanishing if we sum over the $\alpha$-indices. For this reason, the constant $C$ is dropped from actual calculations. Starting with the Kernel operator

$$\mathcal{K}^{(2)} = \sum_{\substack{nmp \\ l\alpha\alpha'}} \alpha\alpha' \, \Gamma^p_{l,nm} d_n^{\bar{p},\alpha} d_m^{p,\alpha'} Y_+^\alpha \left(\beta(i\hbar\mathcal{L}_\mathrm{S} - p\mu_l)\right) \tag{B.1}$$

we focus on the part with $C$:

$$\begin{aligned}
&\frac{iC}{2\pi} \sum_{\substack{nmp \\ l\alpha\alpha'}} \alpha\alpha' \, \Gamma^p_{l,nm} d_n^{\bar{p},\alpha} d_m^{p,\alpha'} \alpha \\
&= \frac{iC}{2\pi} \sum_{nm} \Big\{ \Gamma^+_{l,nm} \left( d_n^{-,+} d_m^{+,+} - d_n^{-,+} d_m^{+,-} + d_n^{-,-} d_m^{+,+} - d_n^{-,-} d_m^{+,-} \right) \\
&\quad + \Gamma^-_{l,nm} \left( d_n^{+,+} d_m^{-,+} - d_n^{+,+} d_m^{-,-} + d_n^{+,-} d_m^{-,+} - d_n^{+,-} d_m^{-,-} \right) \Big\} \\
&= \frac{iC}{2\pi} \sum_{nm} \Big\{ \Gamma^+_{l,nm} \left( -d_m^{+,+} d_n^{-,+} + \delta_{nm} - d_m^{+,-} d_n^{-,+} + d_m^{+,+} d_n^{-,-} + d_m^{+,-} d_n^{-,-} - \delta_{nm} \right) \\
&\quad + \Gamma^+_{l,nm} \left( d_m^{+,+} d_n^{-,+} - d_m^{+,+} d_n^{-,-} + d_m^{+,-} d_n^{-,+} - d_m^{+,-} d_n^{-,-} \right) \Big\} \\
&= 0
\end{aligned} \tag{B.2}$$

In the second last step, we used the fermionic anticommutator relation $\{d_i, d_j^\dagger\} = \delta_{ij}$ which reverses the sign of the first and the last contribution. The part with $\Gamma^-_{l,nm}$ can be written as $\Gamma^+_{l,mn}$ and then the variable names can be consistently switched ($n \leftrightarrow m$).

# C

# Cotunnelling energy integrals

In the cotunnelling transport regime, we encounter two different types of integrals, namely the $D$- and the $X$-function. In this section, we will perform these two integrals and they will be displayed in different cases in the same way as they are displayed in the appendix of the dissertation of S. Koller [5]. The decisive distinction will be that we will do the full complex calculation. It should be noted that the functions $D$ and $X$ are smoothly transforming between these cases within itself. The reason why these cases are anyway used is that they speed up the numerical calculation of the $D$- and the $X$-function a lot while enhancing the accuracy. Quite often the diagrams which need to be calculated have e.g. the restriction $\Delta = 0$. Therefore, it is not needed to perform a slowly converging sum of digamma functions with taking the limit of $\Delta \to 0$ but rather use an analytic expression for specific sums of digamma functions.

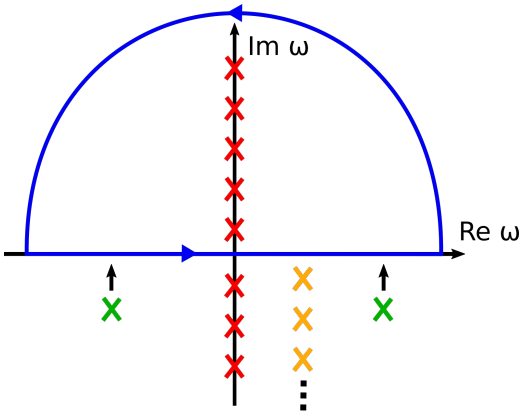


**Figure C.1 | Contour integral of Eq. (C.1) in the complex plane:** The blue line depicts the integration path and the crosses are representing the poles of the Fermi-function (red), the poles of the two denominators (green) and the poles of the digamma function (yellow). The poles are located at $i\omega_k = 2\pi i\left(k+\frac{1}{2}\right)$ for $k \in \mathbb{Z}$ with residuum $-p$ for $f^p(\omega)$, at $\omega = \mu - i\eta$ with residuum $+1$ for $(\omega - \mu - i\eta)^{-1}$ (or $\mu'$ instead of $\mu$) and at $i\omega_k = \Delta - 2\pi i\left(k+\frac{1}{2}\right)$ for $k \in \mathbb{N}$ with residuum $-2\pi i$ for $\Psi^{(0)}\left(\frac{1}{2}+\frac{i(\Delta-\omega)}{2\pi}\right)$.

The following three equations will help us for the integration:

$$
\begin{aligned}
(*1) &= \sum_{k=0}^{\infty} \frac{\Psi^{(0)}(k+1)}{k+p}\frac{1}{k+q} \\
&= \begin{cases} \dfrac{1}{2(q-p)}\left[\Psi^{(1)}(p) - \Psi^{(1)}(q) - \left(\Psi^{(0)}(p)\right)^2 + \left(\Psi^{(0)}(q)\right)^2\right] & p \neq q, \\ \Psi^{(0)}(p)\,\Psi^{(1)}(p) - \dfrac{1}{2}\Psi^{(2)}(p) & p = q;\ p,q \in \mathbb{C} \end{cases} \\
(*2) &= \sum_{k=0}^{\infty} \frac{1}{k+p}\frac{1}{k+q} = \\
&= \begin{cases} \dfrac{1}{p-q}\left[\Psi^{(0)}(p) - \Psi^{(0)}(q)\right] & p \neq q, \\ \Psi^{(1)}(p) & p = q;\ p,q \in \mathbb{C} \end{cases} \\
(*3) &= \lim_{\eta\to 0}\int d\omega \frac{f^n(\omega)}{\omega-\mu+i\eta}\frac{1}{\omega-\mu'+i\eta} \\
&= \Bigg\{ \text{Applying residue theorem: 1. } k^{\text{th}}\text{- residue of } f^n(\omega) \text{ is -n and the poles are at} \\
&\quad i\omega_k = 2\pi i\left(k+\tfrac{1}{2}\right);\ 2.\ \text{The poles of the two denominators do not contribute} \\
&\quad \text{because they are not inside the chosen contour (compare Figure C.1)} \Bigg\} \\
&= 2\pi i \sum_{k=0}^{\infty}(-n)\frac{1}{2\pi i(k+\frac{1}{2})-\mu}\frac{1}{2\pi i(k+\frac{1}{2})-\mu'} = \frac{in}{2\pi}\sum_{k=0}^{\infty}\frac{1}{k+\frac{1}{2}+\frac{i\mu}{2\pi}}\frac{1}{k+\frac{1}{2}+\frac{i\mu'}{2\pi}} \\
&= \frac{in}{2\pi}\frac{1}{\frac{i(\mu-\mu')}{2\pi}}\left[\Psi^{(0)}\left(\frac{1}{2}+\frac{i\mu}{2\pi}\right) - \Psi^{(0)}\left(\frac{1}{2}+\frac{i\mu'}{2\pi}\right)\right]
\end{aligned}
$$

The relations of (∗1) and (∗2) are taken from [45].

**D.i** Given $\mu = \mu'$

$$
\begin{aligned}
&-\frac{4\pi^2}{i\hbar} D^{n\,n'}_{++}(\mu,\mu,\Delta) = \\
&= \lim_{\eta\to 0} \int d\omega \int d\omega' \frac{f^n(\omega)}{\omega-\mu+i\eta} \frac{1}{\omega+\omega'-\Delta+i\eta} \frac{f^{n'}(\omega')}{\omega-\mu+i\eta} \\
&\overset{(A.1)}{=} \lim_{\eta\to 0} \int d\omega \frac{f^n(\omega)}{\omega-\mu+i\eta} \frac{1}{\omega-\mu+i\eta} \\
&\left[-\frac{i\pi}{2} + n'\left(\Psi^{(0)}\left(\frac{1}{2}+\frac{i(\Delta-\omega)}{2\pi}\right) - C\right)\right] \\
&\overset{(*2)}{=} \left(-\frac{i\pi}{2} - Cn'\right) \frac{in}{2\pi} \Psi^{(1)}\left(\frac{1}{2}+\frac{i\mu}{2\pi}\right) \\
&+ \lim_{\eta\to 0} \int d\omega \frac{f^n(\omega)}{\omega-\mu+i\eta} \frac{1}{\omega-\mu+i\eta} n' \Psi^{(0)}\left(\frac{1}{2}+\frac{i(\Delta-\omega)}{2\pi}\right) \qquad \text{(C.1)} \\
&\overset{(\text{Fig.}C.1)}{\overset{+(*1)}{=}} \left(-\frac{i\pi}{2} - Cn'\right) \frac{in}{2\pi} \Psi^{(1)}\left(\frac{1}{2}+\frac{i\mu}{2\pi}\right) \\
&+ \begin{cases} \dfrac{inn'}{2\pi} \displaystyle\sum_{k=0}^{\infty} \frac{\Psi^{(0)}\left(1+k+\frac{i\Delta}{2\pi}\right)}{\left(k+\frac{1}{2}+\frac{i\mu}{2\pi}\right)^2}, & \Delta \neq 0 \\ \dfrac{inn'}{2\pi}\left[\Psi^{(1)}\left(\frac{1}{2}+\frac{i\mu}{2\pi}\right)\Psi^{(0)}\left(\frac{1}{2}+\frac{i\mu}{2\pi}\right) - \frac{1}{2}\Psi^{(2)}\left(\frac{1}{2}+\frac{i\mu}{2\pi}\right)\right], & \Delta = 0 \end{cases} \qquad \text{(C.2)}
\end{aligned}
$$

## D.ii Given $\mu \neq \mu'$

$$
\begin{aligned}
&-\frac{4\pi^2}{i\hbar} D^{n\,n'}_{++}(\mu,\mu',\Delta) = \\
&\lim_{\eta\to 0}\int d\omega \int d\omega' \frac{f^n(\omega)}{\omega-\mu+i\eta}\frac{1}{\omega+\omega'-\Delta+i\eta}\frac{f^{n'}(\omega')}{\omega-\mu'+i\eta} \\
&\overset{(A.1)}{=} \lim_{\eta\to 0}\int d\omega \frac{f^n(\omega)}{\omega-\mu+i\eta}\frac{1}{\omega-\mu'+i\eta} \\
&\left[\frac{-i\pi}{2} + n'\left(\Psi^{(0)}\left(\frac{1}{2}+\frac{i(\Delta-\omega)}{2\pi}\right) - C\right)\right] \\
&\overset{(*3)}{=} \left(-\frac{i\pi}{2} - Cn'\right)\frac{n}{\mu-\mu'}\left[\Psi^{(0)}\left(\frac{1}{2}+\frac{i\mu}{2\pi}\right) - \Psi^{(0)}\left(\frac{1}{2}+\frac{i\mu'}{2\pi}\right)\right] \\
&+ \lim_{\eta\to 0}\int d\omega \frac{f^n(\omega)}{\omega-\mu+i\eta}\frac{1}{\omega-\mu'+i\eta} n'\Psi^{(0)}\left(\frac{1}{2}+\frac{i(\Delta-\omega)}{2\pi}\right) \\
&\overset{(\text{Fig.}C.1)}{\overset{+(*1)}{=}} \left(-\frac{i\pi}{2} - Cn'\right)\frac{n}{\mu-\mu'}\left[\Psi^{(0)}\left(\frac{1}{2}+\frac{i\mu}{2\pi}\right) - \Psi^{(0)}\left(\frac{1}{2}+\frac{i\mu'}{2\pi}\right)\right] \\
&+ \begin{cases} \dfrac{inn'}{2\pi}\displaystyle\sum_{k=0}^{\infty}\dfrac{\Psi^{(0)}\left(1+k+\frac{i\Delta}{2\pi}\right)}{\left(k+\frac{1}{2}+\frac{i\mu}{2\pi}\right)\left(k+\frac{1}{2}+\frac{i\mu'}{2\pi}\right)} & \Delta \neq 0, \\ \dfrac{nn'}{2(\mu-\mu')}\left[\Psi^{(1)}\left(\frac{1}{2}+\frac{i\mu'}{2\pi}\right) - \Psi^{(1)}\left(\frac{1}{2}+\frac{i\mu}{2\pi}\right)\right. & \\ \left. - \left(\Psi^{(0)}\left(\frac{1}{2}+\frac{i\mu'}{2\pi}\right)\right)^2 + \left(\Psi^{(0)}\left(\frac{1}{2}+\frac{i\mu}{2\pi}\right)\right)^2\right] & \Delta = 0 \end{cases}
\end{aligned}
$$

## X.i Given $\mu + \mu' = \Delta$

$$
\begin{aligned}
&-\frac{4\pi^2}{i\hbar} X_{++}^{n\,n'}(\mu,\mu',\Delta) = \\
&= \lim_{\eta\to 0}\int d\omega \int d\omega' \frac{f^n(\omega)}{\omega-\mu+i\eta}\frac{1}{\omega+\omega'-\Delta+i\eta}\frac{f^{n'}(\omega')}{\omega'-\mu'+i\eta} \\
&\overset{(*3)}{=} \lim_{\eta\to 0}\int d\omega' \frac{f^{n'}(\omega')}{\omega'-\mu'+i\eta}\left(\frac{in}{2\pi}\right)\frac{2\pi}{i(\mu+\omega'-\Delta+i\eta)} \\
&\quad\left[\Psi^{(0)}\left(\frac{1}{2}+\frac{i\mu}{2\pi}\right)-\Psi^{(0)}\left(\frac{1}{2}+\frac{i(\Delta-\omega')}{2\pi}\right)\right] \\
&= \lim_{\eta\to 0}\int d\omega' \frac{f^{n'}(\omega')}{\omega'-\mu'+i\eta}\frac{n}{\mu+\omega'-\Delta+i\eta}\Psi^{(0)}\left(\frac{1}{2}+\frac{i\mu}{2\pi}\right) \\
&\quad -\lim_{\eta\to 0}\int d\omega' \frac{f^{n'}(\omega')}{\omega'-\mu'+i\eta}\frac{n}{\mu+\omega'-\Delta+i\eta}\Psi^{(0)}\left(\frac{1}{2}+\frac{i(\Delta-\omega')}{2\pi}\right) \\
&\overset{\substack{(\mathrm{Fig.}C.1)\\ +(*1)}}{=} +\frac{inn'}{2\pi}\Psi^{(0)}\left(\frac{1}{2}+\frac{i\mu}{2\pi}\right)\Psi^{(1)}\left(\frac{1}{2}+\frac{i\mu'}{2\pi}\right) \\
&\quad -\begin{cases}
\dfrac{inn'}{2\pi}\displaystyle\sum_{k=0}^{\infty}\frac{\Psi^{(0)}\left(1+k+\frac{i\Delta}{2\pi}\right)}{\left(k+\frac{1}{2}+\frac{i\mu'}{2\pi}\right)^2} & \Delta\neq 0, \\
\dfrac{inn'}{2\pi}\left[\Psi^{(1)}\left(\frac{1}{2}+\frac{i\mu'}{2\pi}\right)\Psi^{(0)}\left(\frac{1}{2}+\frac{i\mu'}{2\pi}\right)\right. & \\
\left.-\dfrac{1}{2}\Psi^{(2)}\left(\frac{1}{2}+\frac{i\mu'}{2\pi}\right)\right] & \Delta = 0
\end{cases}
\end{aligned}
$$

## X.ii Given $\mu + \mu' \neq \Delta$

$$
\begin{aligned}
&-\frac{4\pi^2}{i\hbar} X_{++}^{n\,n'}(\mu,\mu',\Delta) = \\
&= \lim_{\eta\to 0}\int d\omega \int d\omega' \frac{f^{n}(\omega)}{\omega-\mu+i\eta}\frac{1}{\omega+\omega'-\Delta+i\eta}\frac{f^{n'}(\omega')}{\omega'-\mu'+i\eta} \\
&\overset{(*3)}{=} \lim_{\eta\to 0}\int d\omega' \frac{f^{n'}(\omega')}{\omega'-\mu'+i\eta}\left(\frac{in}{2\pi}\right)\frac{2\pi}{i(\mu+\omega'-\Delta+i\eta)} \\
&\quad \left[\Psi^{(0)}\left(\frac{1}{2}+\frac{i\mu}{2\pi}\right)-\Psi^{(0)}\left(\frac{1}{2}+\frac{i(\Delta-\omega')}{2\pi}\right)\right] \\
&= \lim_{\eta\to 0}\int d\omega' \frac{f^{n'}(\omega')}{\omega'-\mu'+i\eta}\frac{n}{\mu+\omega'-\Delta+i\eta}\Psi^{(0)}\left(\frac{1}{2}+\frac{i\mu}{2\pi}\right) \\
&\quad - \lim_{\eta\to 0}\int d\omega' \frac{f^{n'}(\omega')}{\omega'-\mu'+i\eta}\frac{n}{\mu+\omega'-\Delta+i\eta}\Psi^{(0)}\left(\frac{1}{2}+\frac{i(\Delta-\omega')}{2\pi}\right) \\
&= \begin{cases}
\dfrac{nn'}{\mu+\mu'-\Delta}\Psi^{(0)}\left(\frac{1}{2}+\frac{i\mu}{2\pi}\right)\left[\Psi^{(0)}\left(\frac{1}{2}+\frac{i\mu'}{2\pi}\right)-\Psi^{(0)}\left(\frac{1}{2}+\frac{i(\Delta-\mu)}{2\pi}\right)\right] \\
\quad -\dfrac{inn'}{2\pi}\displaystyle\sum_{k=0}^{\infty}\frac{\Psi^{(0)}\left(1+k+\frac{i\Delta}{2\pi}\right)}{\left(k+\frac{1}{2}+\frac{i\mu'}{2\pi}\right)\left(k+\frac{1}{2}+\frac{i(\Delta-\mu)}{2\pi}\right)} & \Delta\neq 0, \\
\dfrac{nn'}{\mu+\mu'}\Psi^{(0)}\left(\frac{1}{2}+\frac{i\mu}{2\pi}\right)\left[\Psi^{(0)}\left(\frac{1}{2}+\frac{i\mu'}{2\pi}\right)-\Psi^{(0)}\left(\frac{1}{2}-\frac{i\mu}{2\pi}\right)\right] \\
\quad +\dfrac{nn'}{2(\mu+\mu')}\left[\Psi^{(1)}\left(\frac{1}{2}+\frac{i\mu'}{2\pi}\right)-\Psi^{(1)}\left(\frac{1}{2}-\frac{i\mu}{2\pi}\right)\right. \\
\quad \left.-\left(\Psi^{(0)}\left(\frac{1}{2}+\frac{i\mu'}{2\pi}\right)\right)^2+\left(\Psi^{(0)}\left(\frac{1}{2}-\frac{i\mu}{2\pi}\right)\right)^2\right] & \Delta=0
\end{cases}
\end{aligned}
$$

Furthermore, we want to give the explicit reexpressing of the cotunnelling integrals in order to get from Eq. (4.37) to Eq. (4.41). It is done exemplary with the $D$-function but it similarly applies to the $X$-function.

$$
\begin{aligned}
&-\frac{i\hbar}{4\pi^2}\int_{-\infty}^{\infty}\mathrm{d}\varepsilon\int_{-\infty}^{\infty}\mathrm{d}\varepsilon'\frac{f^{(p\alpha_1)}(\varepsilon)}{i0^+ + p\varepsilon-\Delta E_3}\frac{1}{i0^+ + p\varepsilon+p'\varepsilon'-\Delta E_2}\frac{f^{(p'\alpha_2)}(\varepsilon')}{i0^+ + p\varepsilon-\Delta E_1} \\
&\overset{\varepsilon=\omega/\beta}{=} -\beta\frac{i\hbar}{4\pi^2}\int_{-\infty}^{\infty}\mathrm{d}\omega\int_{-\infty}^{\infty}\mathrm{d}\omega'\frac{f^{(\alpha_1)}(p(\omega-\beta\mu_l))}{i0^+ + p\omega-\beta\Delta E_3}\frac{1}{i0^+ + p\omega+p'\omega'-\beta\Delta E_2} \\
&\frac{f^{(\alpha_2)}(p'(\omega'-\beta\mu_{l'}))}{i0^+ + p\omega-\beta\Delta E_1} \\
&\overset{\substack{\tilde\omega=\omega-\beta\mu_l\\ \tilde\omega'=\omega'-\beta\mu_{l'}}}{=} -\beta\frac{i\hbar}{4\pi^2}\int_{-\infty}^{\infty}\mathrm{d}\tilde\omega\int_{-\infty}^{\infty}\mathrm{d}\tilde\omega'\frac{f^{(\alpha_1)}(p\tilde\omega)}{i0^+ + p\tilde\omega+p\beta\mu_l-\beta\Delta E_3} \\
&\frac{1}{i0^+ + p\tilde\omega+p\beta\mu_l+p'\tilde\omega'+p'\beta\mu_{l'}-\beta\Delta E_2}\frac{f^{(\alpha_2)}(p'\tilde\omega')}{i0^+ + p\tilde\omega'+p'\beta\mu_l-\beta\Delta E_1} \\
&= \beta D_{++}^{\alpha_1\alpha_2}(\beta\Delta E_3-\beta p\mu_l,\beta\Delta E_1-\beta p\mu_l,\beta\left(\Delta E_2-p\mu_l-p'\mu_{l'}\right))
\end{aligned}
$$

# D

# Equations of motion for a double quantum dot

In this chapter, the coupled equations of motion for a double quantum dot which is specified in section 5.2 are given. In principle, we need 30 parameters to precisely specify this double quantum dot. There exist 16 eigenstates of the system which are depicted in Table D.1. We see that the six states of particle number two are divided into a ground state triplet ($p_{2gT}$), a ground state singlet ($p_{2gS}$) and two localized excited singlets ($p_{2eS\alpha}$). The one- respective three-particle populations and spins are constructed in analogy to a single quantum dot. In order to correctly account for all degree of freedoms of the triplet state, we have to include quadrupole moments which can describe spin anisotropy and give additional terms of spin relaxation. The notation of the following analysis is based on the work of M. Baumgärtel et al. [46]. To begin with, we choose the orbital part of the tunnelling rate matrix to be proportional to the identity which describes equal coupling to both orbitals:

$$\Gamma^p_{l,nm} = \left[\Gamma_l^{\text{spin}} \otimes \Gamma_l^{\text{orb}}\right]^p_{nm} = \left[\left(\mathbb{1}_2 + P_l^{\text{spin}} \boldsymbol{n}_l^{\text{spin}} \cdot \boldsymbol{\sigma}\right) \otimes \left(\Gamma_l^{\text{orb}} \mathbb{1}_2\right)\right]^p_{nm} \tag{D.1}$$

Moreover, we define the quadrupole moment tensor operator $\hat{Q}$ as

$$\hat{Q}_{ij} = \frac{1}{2}\left(\hat{S}_i\hat{S}_j - \hat{S}_j\hat{S}_i\right) - \frac{1}{3}\hat{\boldsymbol{S}}\delta_{ij} \tag{D.2}$$

where $\hat{S}_i$ is the $i = x, y, z$ component of the spin operator $\hat{\boldsymbol{S}} = \frac{1}{2}\sum_{\zeta,\zeta',k} \hat{d}^\dagger_{\zeta',k} (\boldsymbol{\sigma})_{\zeta\zeta'} \hat{d}_{\zeta',k}$ with $\boldsymbol{\sigma}$ as the vector containing the Pauli-matrices (compare Eq. (5.3)). The trace of the quadrupole moment tensor operator $\hat{Q}$ with a density matrix will lead to the nine observable quadrupole moments of the quadrupole moment matrix $\boldsymbol{Q}$. Not all the moments are independent so that in principle only five are needed to completely describe the anisotropy of the spin (e.g. $Q_{z^2}$, $Q_{x^2-y^2}$, $Q_{xx}$, $Q_{xy}$, $Q_{xz}$, $Q_{yz}$). Though, we opted to take into account all the nine entries in order to simplify the coupled equations. We will use e.g. $(\boldsymbol{Q}\times\boldsymbol{B})_{ij} = \epsilon_{jkl}Q_{ik}B_l$ and $(\boldsymbol{B}\times\boldsymbol{Q})_{ij} = \epsilon_{ikl}B_kQ_{lj}$ where $\epsilon$ is the Levi-Civita symbol. Moreover, we define a dyadic product as $(\boldsymbol{ab})_{ij} = a_ib_j$ which will give us a matrix. The product $\boldsymbol{Q}\cdot\boldsymbol{\gamma}^\pm_{nm}$ is defined as a conventional matrix-vector product. Similarly to the single dot equations of motion (compare Eqs. (5.5)), we define $\gamma^\pm_{\text{nm}} = \sum_l \gamma^\pm_{l,\text{nm}}$ and $\gamma^\pm_{l,\text{nm}} = \Gamma_l^{\text{orb}} f_l^\pm(\varepsilon - \mu_{\text{nm}})$ where $\mu_{\text{nm}}$ is the energy difference between the state n and the state m. The vectorial form is defined by $\boldsymbol{\gamma}^\pm_{\text{nm}} = \sum_l \boldsymbol{n}_l P_l \gamma^\pm_{l,\text{nm}}$. This time though, we encounter two different effective magnetic fields which we denote by $\boldsymbol{B}_{mn-op} = \sum_l 2P_l\Gamma_l^{\text{orb}}\text{Im}\left(Y_+^+(\mu_{mn} - \mu_l) - Y_+^+(\mu_{op} - \mu_l)\right)\boldsymbol{n}_l$. Out of an analysis of the quations of motion, we can predict the position of the resonance lines in this double quantum dot (compare section 5.2). Another interesting point is the appearance of the quadrupole moments which enrich the physics of this particular problem. We can extract that they couple to the spin of one-/three-particle occupation but as well to the

spin of the triplet. Interestingly, this coupling $\boldsymbol{Q}\cdot\boldsymbol{\gamma}^-_{2g1}$ to both spins differs in terms of the sign so that this contribution tends to make these spins non-collinear [46]. The effective magnetic field exerts a torque on the quadrupole moments via the terms $(\boldsymbol{B}\times\boldsymbol{Q})$ and $(\boldsymbol{Q}\times\boldsymbol{B})$. The index $\alpha$ can take the value $d1$ respective $d2$ and $\bar{\alpha}$ takes the opposite value of $\alpha$. In order to simplify the equations, we define here $p_1 = p_{1d1} + p_{1d2}$, $\boldsymbol{S}_1 = \boldsymbol{S}_{1d1} + \boldsymbol{S}_{1d2}$, $p_3 = p_{3d1} + p_{3d2}$ and $\boldsymbol{S}_3 = \boldsymbol{S}_{3d1} + \boldsymbol{S}_{3d2}$. The equations are then:

$$\dot{p}_0 = -4\gamma^+_{10}\,p_0 + \gamma^-_{10}p_1 + 2\boldsymbol{\gamma}^-_{10}\cdot\boldsymbol{S}_1, \tag{D.3a}$$

$$\dot{p}_{1\alpha} = 2\gamma^+_{10}\,p_0 - \left(\gamma^-_{10} + \gamma^+_{2e1} + 2\gamma^+_{2g1}\right)p_{1\alpha} + 2\gamma^-_{2e1}\,p_{2eS\alpha} + \gamma^-_{2g1}\left(p_{2gS} + p_{2gT}\right) - 2\left(\boldsymbol{\gamma}^-_{10} - \boldsymbol{\gamma}^+_{2e1}\right)\cdot\boldsymbol{S}_{1\alpha} + \boldsymbol{\gamma}^-_{2g1}\cdot\boldsymbol{S}_{2gT}, \tag{D.3b}$$

$$\dot{\boldsymbol{S}}_{1\alpha} = \boldsymbol{\gamma}^+_{10}\,p_0 + \tfrac{1}{2}\left(-\boldsymbol{\gamma}^-_{10} + \boldsymbol{\gamma}^+_{2e1}\right)p_{1\alpha} - \boldsymbol{\gamma}^-_{2e1}\,p_{2eS\alpha} + \boldsymbol{\gamma}^-_{2g1}\left(\tfrac{1}{6}p_{2gT} - \tfrac{1}{2}p_{2gS}\right) - \left(\gamma^-_{10} + \gamma^+_{2e1} + 2\gamma^+_{2g1}\right)\boldsymbol{S}_{1\alpha} + \tfrac{1}{2}\gamma^-_{2g1}\boldsymbol{S}_{2gT} - \boldsymbol{S}_{1\alpha}\times\boldsymbol{B}_{10-2e1} + \boldsymbol{Q}\cdot\boldsymbol{\gamma}^-_{2g1}, \tag{D.3c}$$

$$\dot{p}_{2gT} = \tfrac{3}{2}\gamma^+_{2g1}p_1 - 2\left(\gamma^-_{2g1} + \gamma^+_{32g}\right)p_{2gT} + \tfrac{3}{2}\gamma^-_{32g}p_3 + \boldsymbol{\gamma}^+_{2g1}\cdot\boldsymbol{S}_1 + 2\left(\boldsymbol{\gamma}^+_{32g} - \boldsymbol{\gamma}^-_{2g1}\right)\cdot\boldsymbol{S}_{2gT} - \boldsymbol{\gamma}^-_{32g}\cdot\boldsymbol{S}_3, \tag{D.3d}$$

$$\dot{p}_{2gS} = \tfrac{1}{2}\gamma^+_{2g1}p_1 - 2\left(\gamma^-_{2g1} + \gamma^+_{32g}\right)p_{2gS} + \tfrac{1}{2}\gamma^-_{32g}p_3 - \boldsymbol{\gamma}^+_{2g1}\cdot\boldsymbol{S}_1 + \boldsymbol{\gamma}^-_{32g}\cdot\boldsymbol{S}_3, \tag{D.3e}$$

$$\dot{p}_{2eS\alpha} = \gamma^+_{2e1}\,p_{1\alpha} - 2\left(\gamma^-_{2e1} + \gamma^+_{32e}\right)p_{2eS\alpha} + \gamma^-_{32e}\,p_{3\alpha} + 2\boldsymbol{\gamma}^-_{32e}\cdot\boldsymbol{S}_{3\bar{\alpha}} - 2\boldsymbol{\gamma}^+_{2e1}\cdot\boldsymbol{S}_{1\alpha}, \tag{D.3f}$$

$$\dot{\boldsymbol{S}}_{2gT} = \tfrac{4}{3}\left(\boldsymbol{\gamma}^+_{32g} - \boldsymbol{\gamma}^-_{2g1}\right)p_{2gT} + \boldsymbol{\gamma}^+_{2g1}p_1 - \boldsymbol{\gamma}^-_{32g}p_3 + 2\gamma^+_{2g1}\boldsymbol{S}_1 + 2\gamma^-_{32g}\boldsymbol{S}_3 - 2\left(\gamma^+_{32g} + \gamma^-_{2g1}\right)\boldsymbol{S}_{2gT} - \boldsymbol{S}_{2gT}\times\boldsymbol{B}_{2g1-32g} + 2\boldsymbol{Q}\cdot\left(\boldsymbol{\gamma}^+_{32g} - \boldsymbol{\gamma}^-_{2g1}\right), \tag{D.3g}$$

$$\begin{aligned}\dot{\boldsymbol{Q}} = {} & -2\left(\gamma^-_{2g1} + \gamma^+_{32g}\right)\boldsymbol{Q} - \boldsymbol{Q}\times\boldsymbol{B}_{2g1-32g} + \boldsymbol{B}_{2g1-32g}\times\boldsymbol{Q} \\ & + 2\left(\boldsymbol{S}_1\boldsymbol{\gamma}^+_{2g1} + \boldsymbol{\gamma}^+_{2g1}\boldsymbol{S}_1\right) - 2\left(\boldsymbol{S}_3\boldsymbol{\gamma}^-_{32g} + \boldsymbol{\gamma}^-_{32g}\boldsymbol{S}_3\right) \\ & - \tfrac{1}{2}\left(\boldsymbol{S}_{2gT}\left(\boldsymbol{\gamma}^-_{2g1} - \boldsymbol{\gamma}^+_{32g}\right) + \left(\boldsymbol{\gamma}^-_{2g1} - \boldsymbol{\gamma}^+_{32g}\right)\boldsymbol{S}_{2gT}\right) - \tfrac{2}{3}\left(\boldsymbol{\gamma}^+_{2g1}\cdot\boldsymbol{S}_1\right)\mathbb{1}_3 \\ & + \tfrac{1}{3}\left(\left(\boldsymbol{\gamma}^-_{2g1} - \boldsymbol{\gamma}^+_{32g}\right)\cdot\boldsymbol{S}_{2gT}\right)\mathbb{1}_3 + \tfrac{2}{3}\left(\boldsymbol{\gamma}^-_{32g}\cdot\boldsymbol{S}_3\right)\mathbb{1}_3,\end{aligned} \tag{D.3h}$$

$$\dot{p}_{3\alpha} = 2\gamma^-_{43}\,p_4 - \left(\gamma^+_{43} + \gamma^-_{32e} + 2\gamma^-_{32g}\right)p_{3\alpha} + 2\gamma^+_{32e}\,p_{2eS\alpha} + \gamma^+_{32g}\left(p_{2gS} + p_{2gT}\right) + 2\left(\boldsymbol{\gamma}^-_{32e} - \boldsymbol{\gamma}^+_{43}\right)\cdot\boldsymbol{S}_{3\alpha} - \boldsymbol{\gamma}^+_{32g}\cdot\boldsymbol{S}_{2gT}, \tag{D.3i}$$

$$\dot{\boldsymbol{S}}_{3\alpha} = -\boldsymbol{\gamma}^-_{43}\,p_4 + \tfrac{1}{2}\left(-\boldsymbol{\gamma}^-_{32e} + \boldsymbol{\gamma}^+_{43}\right)p_{3\alpha} + \boldsymbol{\gamma}^+_{32e}\,p_{2eS\alpha} + \boldsymbol{\gamma}^+_{32g}\left(-\tfrac{1}{6}p_{2gT} + \tfrac{1}{2}p_{2gS}\right) - \left(\gamma^+_{43} + \gamma^-_{32e} + 2\gamma^-_{32g}\right)\boldsymbol{S}_{3\alpha} + \tfrac{1}{2}\gamma^+_{32}\boldsymbol{S}_{2gT} - \boldsymbol{S}_{3\alpha}\times\boldsymbol{B}_{32e-43} - \boldsymbol{Q}\cdot\boldsymbol{\gamma}^+_{32g}, \tag{D.3j}$$

$$\dot{p}_4 = -4\gamma^-_{43}\,p_4 + \gamma^+_{43}p_3 - 2\boldsymbol{\gamma}^+_{43}\cdot\boldsymbol{S}_3. \tag{D.3k}$$

| Particle number N | State | Energy | Parameters |
|---|---|---|---|
| 0 | $\|0,0\rangle$ | $\varepsilon$ | $p_0$ |
| 1 | $\|\sigma,0\rangle$ | $\varepsilon$ | $p_{1L}, \boldsymbol{S}_{1d1}$ |
| 1 | $\|0,\sigma\rangle$ | $\varepsilon$ | $p_{1d2}, \boldsymbol{S}_{1d2}$ |
| 2 | $\|2,0\rangle$ | $2\varepsilon + U$ | $p_{2eSd1}$ |
| 2 | $\|0,2\rangle$ | $2\varepsilon + U$ | $p_{2eSd2}$ |
| 2 | $\|\uparrow,\downarrow\rangle - \|\downarrow,\uparrow\rangle$ | $2\varepsilon + V$ | $p_{2gS}$ |
| 2 | $\|\uparrow,\downarrow\rangle + \|\downarrow,\uparrow\rangle$ | $2\varepsilon + V$ | $p_{2gT}, \boldsymbol{S}_{2gT}, \boldsymbol{Q}$ |
| 2 | $\|\uparrow,\uparrow\rangle$ | $2\varepsilon + V$ | $p_{2gT}, \boldsymbol{S}_{2gT}, \boldsymbol{Q}$ |
| 2 | $\|\downarrow,\downarrow\rangle$ | $2\varepsilon + V$ | $p_{2gT}, \boldsymbol{S}_{2gT}, \boldsymbol{Q}$ |
| 3 | $\|2,\sigma\rangle$ | $3\varepsilon + U + 2V$ | $p_{3d1}, \boldsymbol{S}_{3d1}$ |
| 3 | $\|\sigma,2\rangle$ | $3\varepsilon + U + 2V$ | $p_{3d2}, \boldsymbol{S}_{3d2}$ |
| 4 | $\|2,2\rangle$ | $4\varepsilon + 2U + 4V$ | $p_4$ |

**Table D.1 | Double quantum dot states according to the setup of Figure 5.3:** In total, there are 16 states in this double quantum dot. The on-site Coulomb energy $U$ is chosen to be higher than the inter-site Coulomb energy $V$ so that two localized singlets (subscript "$2eSd1$" and "$2eSd2$") with particle number two exist. They are excited with respect to the ground state singlet (subscript "$2gS$") and ground state triplet states (subscript "$2gT$"). With $\varepsilon$ the on-site energy is denoted. The subscript "$d1/d2$" labels the two dots which are connected in our chosen setup parallel - not in series - to the leads.

# References


[1] R. P. Feynman, Engineering and Science **23**, 22 (1960).

[2] W. Lu, Y. Lee, J. Murdzek, J. Gertsch, A. Vardi, L. Kong, S. M. George, and J. A. del Alamo, IEEE International Electron Devices Meeting (2018) 10.1109/IEDM.2018.8614536.

[3] D. DiVincenzo, *Mesoscopic Electron Transport* (Springer, 1997).

[4] M.-A. Russon, *The race to make the world's most powerful computer ever (https://www.bbc.com/news/business-45273584)* (BBC, 2018).

[5] S. Koller, *Spin phenomena and higher order effects in transport across interacting quantum-dots* (2010).

[6] T. Young, Phil. Trans. Royal Society of London **94**, 1 (1804).

[7] C. Jönsson, Z. Physik **161**, 454 (1961).

[8] P. G. Merli, G. F. Missiroli, and G. Pozzi, Am. J. Phys. **44**, 306 (1976).

[9] M. Arndt, O. Nairz, J. Vos-Andreae, C. Keller, G. v. der Zouw, and A. Zeilinger, Nature **74**, 4047 (1999).

[10] D. M. Cardamone, C. A. Stafford, and S. Mazumdar, Nano Letters **6**, 2422 (2006).

[11] S.-H. Ke, W. Yang, and H. U. Baranger, Nano Letters **8**, 3257 (2008).

[12] Z. Qian, R. Li, X. Zhao, S. Hou, and S. Sanvito, Phys. Rev. B **78**, 113301 (2008).

[13] G. C. Solomon, D. Q. Andrews, T. Hansen, R. H. Goldsmith, M. R. Wasielewski, R. P. Van Duyne, and M. A. Ratner, The Journal of Chemical Physics **129**, 054701 (2008).

[14] T. Markussen, R. Stadler, and K. S. Thygesen, Nano Letters **10**, 4260 (2010).

[15] T. Markussen, R. Stadler, and K. S. Thygesen, Phys. Chem. Chem. Phys. **13**, 14311 (2011).

[16] Guédon Constant M., Valkenier Hennie, Markussen Troels, Thygesen Kristian S., Hummelen Jan C., and van der Molen Sense Jan, Nature Nanotechnology **7**, 305 (2012).

[17] G. Begemann, D. Darau, A. Donarini, and M. Grifoni, Phys. Rev. B **77**, 201406 (2008).

[18] D. Darau, G. Begemann, A. Donarini, and M. Grifoni, Phys. Rev. B **79**, 235404 (2009).

[19] A. Donarini, G. Begemann, and M. Grifoni, Nano Letters **9**, 2897 (2009).

[20] A. Donarini, G. Begemann, and M. Grifoni, Phys. Rev. B **82**, 125451 (2010).

[21] A. Donarini, M. Niklas, M. Schafberger, N. Paradiso, C. Strunk, and M. Grifoni, Nature Communications **10**, 381 (2019).

[22] H. A. Nilsson, O. Karlström, M. Larsson, P. Caroff, J. N. Pedersen, L. Samuelson, A. Wacker, L.-E. Wernersson, and H. Q. Xu, Phys. Rev. Lett. **104**, 186804 (2010).

[23] J. N. Pedersen and A. Wacker, Phys. Rev. B **72**, 195330 (2005).

[24] O. Karlström, J. N. Pedersen, P. Samuelsson, and A. Wacker, Phys. Rev. B **83**, 205412 (2011).

[25] K. Blum, *Density matrix theory and applications* (Springer, 2012).

[26] A. Donarini, *Lecture notes: density matrix and its application to quantum transport* (2018).

[27] D. Mantelli, *Analytical and numerical study of quantum impurity systems in the intermediate and strong coupling regimes* (2016).

[28] U. Fano, Rev. Mod. Phys. **29**, 74 (1957).

[29] M. Niklas, *Current and noise properties of interacting nanojunctions* (2018).

[30] S. Nakajima, Progress of Theoretical Physics - Kyoto **20**, 948 (1958).

[31] R. Zwanzig, The Journal of Chemical Physics **33**, 1338 (1960).

[32] H. Schoeller and G. Schön, Phys. Rev. B **50**, 18436 (1994).

[33] J. König, H. Schoeller, and G. Schön, Europhysics Letters (EPL) **31**, 31 (1995).

[34] M. Niklas, A. Trottmann, A. Donarini, and M. Grifoni, Phys. Rev. B **95**, 115133 (2017).

[35] M. Hell, B. Sothmann, M. Leijnse, M. R. Wegewijs, and J. König, Phys. Rev. B **91**, 195404 (2015).

[36] S. Koller, M. Grifoni, M. Leijnse, and M. R. Wegewijs, Phys. Rev. B **82**, 235307 (2010).

[37] G. W. Stewart, Mathematics of Computation **69**, 1309 (2000).

[38] A. Donarini, *Dynamics of shuttle devices* (2004).

[39] M. Braun, J. König, and J. Martinek, Phys. Rev. B **70**, 195345 (2004).

[40] V. Meden and F. Marquardt, Phys. Rev. Lett. **96**, 146801 (2006).

[41] G. Alzetta, A. Gozzini, L. Moi, and G. Orriols, Il Nuovo Cimento B (1971-1996) **36**, 5 (1976).

[42] E. Arimondo and G. Orriols, Lettere al Nuovo Cimento (1971-1985) **17**, 333 (1976).

[43] A. Yar, A. Donarini, S. Koller, and M. Grifoni, Phys. Rev. B **84**, 115432 (2011).

[44] A. J. Leggett, *Quantum Liquids: Bose condensation and Cooper pairing in condensed-matter systems* (Oxford Graduate Texts, 2008).

[45] M. Milgram, arXiv Mathematics e-prints, math/0406338 (2004).

[46] M. Baumgärtel, M. Hell, S. Das, and M. R. Wegewijs, Phys. Rev. Lett. **107**, 087202 (2011).

# Acknowledgement

First of all, I want to thank Andrea Donarini for the incredible supervision of my master's thesis. I am utmost grateful that I could work with you. You were always patient to answer one of my many questions. Moreover, I appreciated your endurance to find an appropriate explanation of problems we did not understand at the first place. One point which I especially liked about working with you, is your fascination of physics which is so much contagious. I am really looking forward to work with you during my PhD.

Furthermore, I want to thank Milena Grifoni for creating the very nice atmosphere in your group. I very much enjoyed the Monday group meetings in which you consistently urged people to summarize their work in an easy way so that also the master and bachelor students could grasp the main idea of what they did.

Another big thank you is reserved to my office colleagues Jakob Schlör, Moritz Frankerl, Thomas Naimer, Michael Dafinger and Mario Ebner. I am so happy that I spent the last year in this particular office. The discussions about politics, economy, physics and daily live - I enjoyed them all. If I look back to the memories of the last year, you are definitely the reason which made my master's such an enjoyable time.

Special thanks also to Luca Magazzù and Jordi Picó Cortés for having always a nice lunch time together with fruitful discussions.

I owe the last thank you to my girlfriend Kathleen. You had to listen countless times to the problems which I encountered during my thesis. You gave me a lot of power in the last year which I am very grateful for.

# Eidesstattliche Erklärung

Ich habe die Arbeit selbstständig verfasst und keine anderen als die angegebenen Quellen und Hilfsmittel verwendet und nicht an einer anderen Hochschule zur Erlangung eines akademischen Grades eingereicht. Die vorgelegten Druckexemplare sind identisch mit der vorgelegten elektronischen Version der Arbeit. Ich wurde über wissenschaftlich korrektes Arbeiten und Zitieren aufgeklärt und kenne die Rechtsfolgen nach § 24 Abs. 5.

Regensburg, July 29, 2019

_____

Christoph Rohrmeier